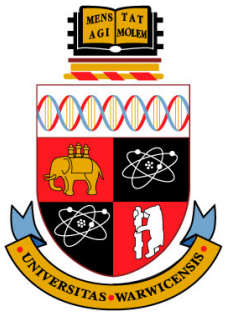

Vlasov Code Development with Inertial Confinement Fusion Applications

by

Nathan John Sircombe

Thesis

Submitted to the University of Warwick

for the degree of

Doctor of Philosophy

Centre for Fusion, Space and Astrophysics, Department of Physics

April 2006

THE UNIVERSITY OF WARWICK

Contents

List of Figures

Acknowledgments

I would like to thank Dr Tony Arber, my supervisor, for his support and guidance throughout my Ph.D. I am grateful to my external supervisor Prof. Richard Dendy, whose interest and support were invaluable and from whom I learnt some of the art of scientific writing.

I want to thank my girlfriend Iona, my parents and friends for their support throughout.

I would also like to thank Dr. Mark Dieckmann, Prof. Padma Shukla and the rest of the Institut für Theoretische Physik IV at the Ruhr-Universität Bochum for their kind hospitality during the month I spent there and their continuing scientific collaboration.

For funding I am grateful to the EPSRC and UKAEA for a CASE studentship.

This thesis was typeset with LaTeX 2_ε[1] by the author.

[1] LaTeX 2_ε is an extension of LaTeX. LaTeX is a collection of macros for TeX. TeX is a trademark of the American Mathematical Society. The style package *wnewthesis* was used.

Declarations

I hereby declare that this thesis is my own work, except where explicitly stated, and that it has not previously been submitted for a degree at the University of Warwick, or any other university.

N. J. Sircombe
January, 2006.

Abstract

Experiments probing fundamental laser-plasma interaction physics have demonstrated some interesting and unexpected effects. Scattering from electron plasma waves with frequencies below the electron plasma frequency (called electron acoustic waves) has been observed in addition to conventional parametric scattering. Reflectivities observed in NIF early light experiments on long scale-length plasmas differed considerably from those predicted by existing fluid models. These effects are essentially kinetic in nature. The low frequency modes are supported by the trapping of electrons at low phase velocities and the saturation of instabilities at the intensities provided by the next generation of laser systems, such as NIF, is associated with the trapping of electrons. Numerical simulation of laser plasma interaction, therefore, benefits from an accurate treatment of the particle kinetics, in particular the evolution of the particle distribution functions.

The direct solution of the Vlasov equation allows a high resolution, noise-free, representation particle distribution functions. Recent advancements in Vlasov codes, which draw a considerable expertise in the numerical solution of hydrodynamic codes, make such an approach to the simulation of laser plasma interaction viable. Here the development of a one dimensional electromagnetic Vlasov code is outlined. The code is applied to realistic laser and plasma parameters characteristic of single hot-spot experiments. Results are in qualitative agreement with experiments displaying both stimulated Raman and stimulated electron acoustic scattering [N. J. Sircombe, T. D. Arber and R. O. Dendy *Kinetic effects in Laser-Plasma coupling: Vlasov theory and computations*, Submitted to Plasma Physics and Controlled Fusion]. The amplitude of simulated electron acoustic waves is greater than that observed experimentally, and is

accompanied by a higher phase velocity. These minor differences may be attributed to the limitations of a one-dimensional collisionless model.

Furthermore, the interaction of a Langmuir wave with a density hole is investigated and shown to result in the acceleration of a small population of electrons [N. J. Sircombe, T. D. Arber and R. O. Dendy, *Accelerated electron populations formed by Langmuir wave-caviton interactions*, Phys. Plasmas, **12**, 012303 (2005)]. This acceleration results from wave breaking and is dependent on the parameters of the background density profiles. In addition, pre-acceleration of electrons in supernova remnant shocks is considered as a kinetic problem [N. J. Sircombe, M. E. Dieckmann, P. K. Shukla and T. D. Arber, *Stabilisation of BGK modes by relativistic effects*, Astronomy and Astrophysics, In Press], [M. E. Dieckmann, N. J. Sircombe, M. Parviainen, P. K. Shukla and R. O. Dendy, *Phase speed of electrostatic waves: The critical parameter for efficient electron surfing acceleration*, Plasma Phys. Control. Fusion **48** (2006) 489-508].

Abbreviations

BGK = Bernstein Green Kruskal

DT = Deuterium Tritium

EM = Electromagnetic

EMW = Electromagnetic Wave

ESW = Electrostatic Wave

HS = Hot Spot

IAW = Ion Acoustic Wave

ICF = Inertial Confinement Fusion

ISM = Interstellar Medium

ITER = International Tokamak Experimental Reactor

KDP = Potassium Dihydrogen Phosphate

LDI = Langmuir Decay Instability

LEH = Laser Entrance Hole

LPI = Laser Plasma Interaction

LWFA = Laser Wakefield Acceleration

MCF = Magnetic Confinement Fusion

MHD = Magnetohydrodynamic

MPI = Message Passing Interface

NIF = National Ignition Facility

PI = Parametric Instability

PIC = Particle In Cell

PPM = Piecewise Parabolic Method

RF = Radio Frequency

RT = Raleigh Taylor

SBS = Stimulated Brillouin Scattering

SEAS = Stimulated Electron Acoustic Scattering

SNR = Supernova Remnant

SRS = Stimulated Raman Scattering

TEM = Transverse Electromagnetic

TIWD = Two Ion Wave Decay

Chapter 1

Introduction

1.1 Preface

With the construction of the latest generation of laser systems, the goal of achieving thermonuclear fusion in the laboratory via inertial confinement is closer than ever. The National Ignition Facility in the US and the Laser Megajoule in France are the largest and most powerful of these and are expected to achieve ignition in the near future. Smaller facilities being constructed (such as the Orion laser in the UK) or upgraded (such as Omega EP in the US and Gecko in Japan) will provide vital insights into the physics of laser plasma interaction and, in some cases, may achieve ignition themselves through innovative lower-energy schemes such as Fast Ignition. Also, the potential of plasmas as a medium for particle acceleration may soon be realised by the development of laser-driven particle accelerators.

The physics of laser plasma interaction, at the energies demanded by a fusion reactor, is a complex and essentially non-linear subject. Electromagnetic waves can excite numerous instabilities in the plasma, scattering incident light, producing super-thermal electrons, creating density holes and driving turbulent structures. Understanding these instabilities, and the complex interplay between them, is an important task for experimental, theoretical and numerical study.

This thesis begins by introducing the concept of thermonuclear fusion and concentrates on fusion with lasers. Key theoretical models are explained along with physical

principals fundamental to laser plasma interaction.

1.2 An Introduction to Fusion

Nuclear fusion is the process of combining two light elements together to create a heavier element with a net yield in energy. This is possible when the combined binding energy of the products is less than the binding energy of the original elements. Nuclear fusion is the process which powers the stars and the mechanism by which the elements were synthesised. Elements up to iron (which has the highest binding energy per nucleon) were created by exothermic fusion reactions in a process known as Stellar Nucleosynthesis. Heavier elements are believed to have formed in endothermic fusion reactions during Supernovae, in a process known as Supernova Nucleosynthesis.

In the context of laboratory physics, nuclear fusion usually refers to one specific type of fusion reaction: the deuterium-tritium (DT) reaction. Here, the nuclei of heavy Hydrogen Isotopes (Deuterium $^{2}\mathrm{H}$ and Tritium $^{3}\mathrm{H}$) fuse to produce a $^{4}\mathrm{He}$ nuclei and a high energy neutron (14.1MeV), as shown in Fig.1.1. In order to overcome the Coulomb barrier, so that nuclear fusion can take place, the kinetic energy of the nuclei must be greater than the activation energy of the reaction, approximately 0.1MeV. This is far greater than the ionisation energy for a hydrogen atom (13.7eV); thus, heating the nuclear fuel produces a plasma. This fusion of nuclei in a plasma is referred to as Thermonuclear Fusion.

Containing and controlling this plasma whilst maintaining conditions favourable to nuclear fusion is an important problem at the heart of all attempts to produce nuclear fusion in the laboratory.

1.2.1 The Fusion Triple Product

The fusion triple product gives an estimate of the conditions necessary for heating by the products of the fusion reaction to maintain the plasma temperature without an external source of energy. To achieve ignition, the conditions within a thermonuclear reactor must satisfy the conditions given by the fusion triple product, while being hot enough

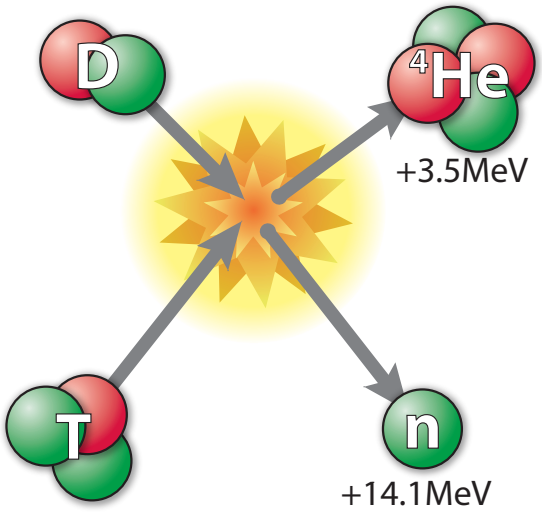

Figure 1.1: Deuterium Tritium (DT) fusion reaction. The two heavy isotopes of Hydrogen fuse, producing a helium nucleus and a high energy neutron. The activation energy for the reaction, 0.1MeV, is significantly higher than the ionisation energy of hydrogen, 13.7eV, so the fuel is in the form of a plasma. This fusion reaction is generally referred to as thermonuclear fusion. Thermonuclear fusion in the laboratory usually takes one of two approaches; magnetic confinement, where diffuse plasma is confined by magnetic fields over long time-scales; or inertial confinement fusion, where a plasma is compressed to high densities over very short time-scales.

for the fusion reaction to take place.

The Fusion Triple Product is the product of plasma density n, temperature T and confinement time τ. For the case of DT fuel, assuming all species have the same temperature, each fuel is in equal abundance and there are no impurities, $nT\tau$ can be calculated as follows.

The confinement time, τ is the energy content W divided by the power loss P_{loss}, where $W = P/(\gamma - 1)$. Taking $P = 2n\kappa T$ and $\gamma = 5/3$ where κ is Boltzmann's constant. The electron and ion densities and temperatures are assumed to be equal, hence the total energy density is given by $W = 3n\kappa T$. The energy produced per unit volume by the fusion reactions is given by $(1/4)n^2 \langle \sigma v \rangle E$ where E is the energy of the fusion reaction and $\langle \sigma v \rangle$ is the product of the reaction cross-section and relative velocity averaged over a Maxwellian veloctity distribution. Since only the charged particles contribute to the plasma heating, $E = E_{ch}$: the energy of the charged fusion products. For the DT fusion reaction, $E_{ch} = 3.5\mathrm{MeV}$. Heating must exceed the losses: $(1/4)n^2 \langle \sigma v \rangle E_{ch} \geq P_{loss}$. It follows that

$$nT\tau \geq \frac{12\kappa}{E_{ch}} \frac{T^2}{\langle \sigma v \rangle} \approx 10^{21} \mathrm{keV\ s\ m^{-3}}. \tag{1.1}$$

This offers two significantly different regimes for achieving fusion; low density, large confinement time and high density, small confinement time. In practice these regimes correspond to magnetic confinement and inertial confinement.

1.2.2 Magnetic Confinement

Equation (1.1) can be satisfied for low density plasmas if the temperature and confinement time are sufficiently high, of the order of 10^8K for several seconds in the case of the planned ITER (International Tokamak Experimental Reactor) facility. Such extreme temperatures present a serious containment problem. However, since charged particles in a magnetic field follow a helical path about the field lines, a strong magnetic field can be used to isolate the hot plasma from the walls of the reactor vessel. This concept is at the heart of Magnetic Confinement Fusion (MCF). Mirror devices were the first to confine a plasma in this manner but are generally unsuitable as fusion reactors due to instabilities. Most modern MCF devices are based around a Tokamak design. Here, the

magnetic field forms a closed toroidal helix, as shown in Fig.1.2. The confined plasma is heated via RF radiation and neutral beam injection to temperatures sufficient for thermonuclear fusion.

1.2.3 Inertial Confinement

The second fusion regime suggested by Eq.(1.1) aims to achieve fusion by compressing the fuel to extremely high densities (twenty times the density of lead) over short time-scales (a few billionths of a second) rather than by heating a low density fuel over long time-scales. In this regime the fuel is confined, and compressed to ignition densities and temperatures, by the action of intense electromagnetic (EM) radiation. This is known as Inertial Confinement Fusion (ICF).

In general, a small ($r \sim 1$mm) pellet of fusion (DT) fuel is compressed and heated by the action of EM radiation. In this case, the timescale of the fusion reaction is proportional to the transit time for a sound wave across the fuel pellet

$$\tau = \frac{R}{\sqrt{\kappa T/m_i}}. \tag{1.2}$$

From Eq.(1.1) it follows that ignition requires $\rho R \geq \frac{12 m_i^{1/2}}{E_{ch}} \frac{\kappa^{3/2} T^{3/2}}{<\sigma v>}$. For DT fuel this is approximately $1\mathrm{gcm}^{-2}$. Some, or all, of the plasma at this density must also be hot enough to achieve the activation energy for the DT fusion reaction and initiate thermonuclear burn. The potential for achieving laboratory scale fusion experiments via inertial confinement was first realised in the early seventies. Since that time the field has advanced considerably, both theoretically and experimentally. The development of ICF, in its various forms, is outlined below.

1.3 Development of ICF

The use of lasers to drive thermonuclear fusion was first outlined by Nuckolls *et al.* [1]. Compressing a complete droplet of DT until the ignition conditions are met, known as volume compression, requires a considerable energy input. Rather than attempt to

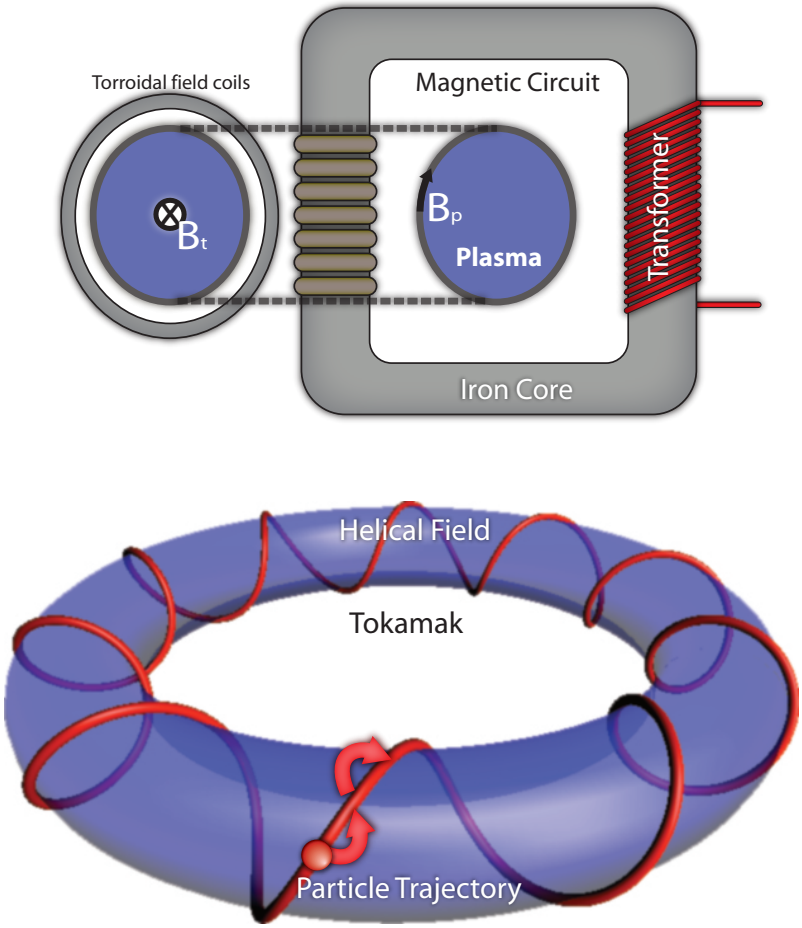

Figure 1.2: The Tokamak is a machine used for Magnetic Confinement Fusion (MCF). It confines the hot (in excess of 100 million Kelvin) plasma in a toroidal magnetic field. The term tokamak comes from the Russian for 'toroidal chamber in magnetic coils'. It is characterised by azimuthal symmetry and the use of the plasma current to generate poloidal field ($\mathbf{B}_p$) which, together with the toroidal field ($\mathbf{B}_t$) produces the helical magnetic field necessary for a stable equilibrium. Particles follow a helical path about the field line shown in red above.

ignite all the available fuel, in central hot-spot (or isobaric hot-spot) ignition, only the very centre of the fuel pellet achieves the conditions necessary for ignition, see Fig.1.3. Compression at the centre is driven by the rocket effect as the outer layers of fuel are ablated. The pressures generated by the rocket effect driven by the deposition of EM energy into the plasma are several orders of magnitude higher than those generated by radiation pressure alone. Once ignition has been achieved at the centre, a thermonuclear burn wave spreads out radially igniting the corona of ablated fuel.

In order for the central hot-spot to form and ignite the fuel, the compression phase needs to be symmetric, and fast. Radiation asymmetries must be avoided and the growth of hydrodynamic instabilities, such as the Raleigh-Taylor instability, minimised. The basic requirements of the central hot-spot (HS) for ignition are: $\rho r_{HS} \sim 0.3\mathrm{gcm}^{-2}$, $T_{HS} = 10\mathrm{keV}$, which can be achieved with an implosion velocity $v_{imp} \sim 4 \times 10^7 \mathrm{cms}^{-1}$. Higher implosion velocities would in principal be desirable but the effects of hydrodynamic instabilities and the driver energy requirements mean that $4 \times 10^7 \mathrm{cm}^{-1}$ is an upper limit when using the rocket effect [2]. The use of a hollow target increases the efficiency by reducing the mass of material which must be accelerated to this velocity.

Two ratios embody what is required of the fuel pellet. These are the convergence ratio, which is the ratio of the initial radius of the ablator to the final radius of the hot-spot, $\frac{R_A}{r_{HS}}$ and the in-flight aspect ratio, the ratio of the shell radius to the shell thickness $\frac{R}{\Delta R}$.

Ignition requires the generation and delivery of a considerable energy flux and pressure. This can be achieved in a variety of ways, using a variety of drivers including lasers, Z-pinches and ion beams. All these methods are variations on two principal approaches; indirect and direct drive. Much of the ICF work conducted to date, and planned for the future, centres on the former. Both are outlined below.

1.3.1 Indirect Drive

In indirect (or radiative) drive, the target is contained within a small high-Z (usually gold) cylinder, known as a Hohlrahm (see Fig.1.4). Incident lasers are directed through the laser entrance holes (LEHs) and onto the inner walls of the Hohlraum, rather than

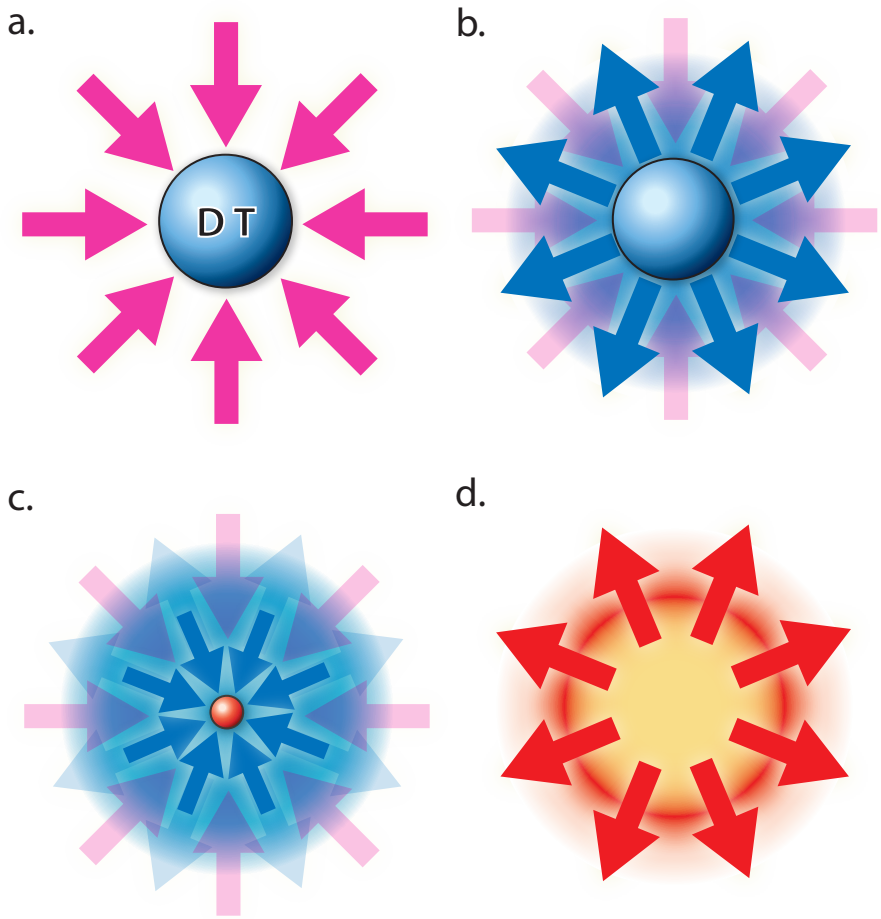

Figure 1.3: Isobaric hot-spot ignition; **a.** outer layers of the fuel pellet are heated and ablated, forming a corona; **b.** rocket-like blow-off of the target's outer layer compresses the fuel at the centre; **c.** hotspot forms in the centre of the compressed fuel and ignites; **d.** thermonuclear burn wave spreads out radially igniting the remaining fuel.

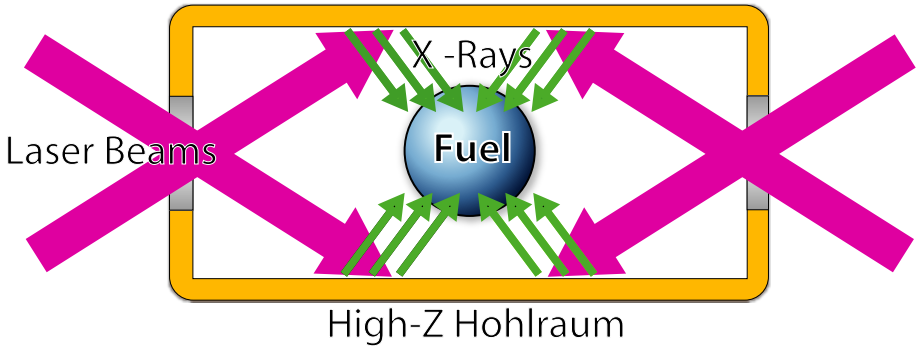

Figure 1.4: Indirect Drive Inertial Confinement. A fuel pellet is suspended within a small gold cylinder (Hohlraum, German for 'hollow room'). The driving laser beams are aimed at the inside wall of the chamber to produce x-rays which then compress the fuel to ignition.

onto the fuel pellet itself. The incident energy heats the Hohlraum walls which emit x-rays that irradiate the target. This process greatly improves the radiation uniformity and avoids, to some extent, problems associated with beam pointing, but sacrifices some efficiency.

The inertial confinement programme in the US, like France, aims to achieve ignition in a central hot-spot by radiative drive, using a Hohlraum. Early laser-plasma experiments in the 1970s and 1980s, combined with the proof that small scale thermonuclear fusion was viable (provided by the Centurion-Halite test programme), validated the target and laser properties which would be required to achieve laboratory scale ignition. This resulted in the National Ignition Programme and the construction of the National Ignition Facility, NIF. Like its predecessors, Shiva and Nova, NIF is based on a Neodymium-Glass laser. The infrared (referred to as 'red' or 1ω light) output of the laser is frequency tripled by KDP crystals (Potassium Dihydrogen Phosphate) which, in essence, combine three infrared photons into one ultraviolet ('blue' or 3ω) photon. Unlike its predecessors, NIF will have 192 beamlines, arranged into groups (or quads) of four beams and be capable of delivering 1.8MJ of 3ω light to the target. The figure of

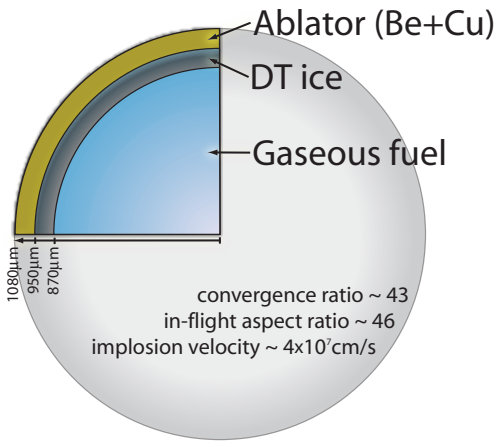

Figure 1.5: Inertial confinement fuel pellet design. The structure is common to most ICF designs; a solid spherical ablator lined with a layer of DT ice together with a gaseous DT core. The capsule size, ablating material, convergence and in-flight aspect ratios and implosion velocity are given for a 300eV NIF target design [3] intended for ignition with 1.3MJ of laser energy with a yield of 17.1MJ. The ablator material and doping varies considerably between target designs.

1.8MJ is intended to be more than sufficient to ignite the NIF point design. This calls for a layered hollow fuel pellet, as shown in Fig.1.5. This basic design is common to all radiation driven ICF schemes and broadly similar to a direct drive target - differing in the in-flight aspect ratio and the ablator doping. This pellet is mounted inside a gold Hohlraum designed for an x-ray radiation temperature of 300-350eV, or approximately 4×10^6K. Too low a temperature and the target may fail to ignite, too high and the efficiency begins to suffer as the effects of scattering and hot electron production become more significant.

Higher Gains

The baseline specification for NIF has been improved upon to increase gain and reduce the ignition energy. Using a laminated Hohlraum constructed of uranium and gold [4] is found to improve the Hohlraum efficiency by increasing the opacity and reducing the pollution of the cavity with heavy ions. Shine shields (see Fig.1.6), originally tried on

Nova [5], shield the fuel from the 'cold' LEHs, improving the Hohlraum efficiency. Other improvements include the addition of radiators (to help to keep the cryogenic fuel cool) and internal baffles, to reduce convection within the Hohlraum.

Other Approaches

Other methods of indirect drive, not detailed here, include; heavy ion driven, where ion beams incident on the Hohlraum produce an x-ray flux to drive compression; Z-pinch driven, where two Z-pinch Hohlraums, one at each end of the fusion Hohlraum, provide the x-ray flux.

1.3.2 Direct Drive

In direct drive, the ablation of the outer layers of the fuel capsule is driven by direct laser irradiation. This approach necessitates the uniform irradiation of the target sphere. The beams must be pointed accurately and the sensitivity to the target quality necessitates a target surface roughness $< 2\%$. Compression with blue, rather than x-ray, light requires a lower in-flight aspect ratio which exacerbates the growth of hydrodynamic instabilities. Beam uniformity can be improved by the introduction of an element of temporal and spatial incoherence to the beam. By dispensing with the Hohlraum, the efficiency is improved considerably. For the same driver energy and fuel mass, direct drive would be expected to produce gains double those of indirect drive.

Polar Direct Drive

Facilities such as NIF are designed to concentrate on the radiation driven path to ignition but are designed to be re-configured for direct drive if required. Polar direct drive is a proposed method for conducting direct drive fusion experiments, possibly even ignition, without the necessity of reconfiguring the beam-lines [6]. To reduce the drive asymmetry some beams would be run at a lesser intensity, reducing the energy available for compression. The addition of a plastic 'saturn' ring around the equator of the target has also been suggested to improve radiation uniformity. During firing, the ring produces

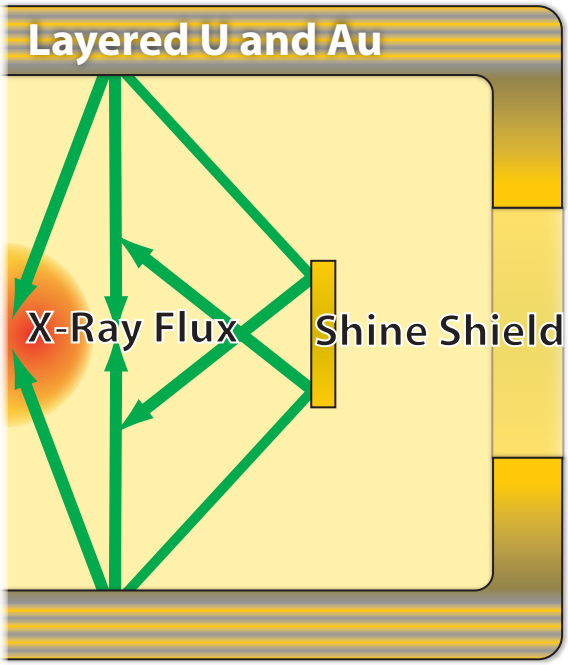

Figure 1.6: Improvements to Hohlraum design can increase efficiency and yield. Shine shields (or LEH shields) obstruct the target's view of the cold LEHs. The use of uranium or uranium gold laminates in the Hohlraum has been shown to improve the Hohlraum's efficiency.

a band of plasma which helps to refract some of the polar beams inwards towards the target centre. Polar direct drive and the Saturn concept are summerised in Fig.1.7.

Fast Ignition

In isobaric ignition a central region of highly compressed fuel is ignited to initiate a thermonuclear burn wave. The compression and ignition are both driven by the rocket effect as the outer layers of fuel are ablated. This necessitates a high degree of implosion symmetry, as well as a considerable driver energy. Fast Ignition attempts to avoid these requirements by separating the tasks of compression and ignition [7, 8]. A central volume of fuel is compressed as before, using multiple long-pulse laser beams. This compressed fuel is then ignited by a second, short-pulse, laser. The second laser produces relativistic electrons [9] which deposit their energy in the ultra dense core, igniting it as shown in Fig.1.8a. Delivering the ignition energy to the core requires the short-pulse beam to traverse the lower density corona of plasma created by the compression beams. This problem can be alleviated by shielding the beam path from the plasma using a hollow gold cone [10], as shown in Fig.1.8b, at the expense of some compression symmetry and heavy ion pollution.

1.4 Modelling a Plasma

Inertial confinement fusion by direct or indirect drive requires a detailed knowledge of a range of physical processes. This thesis focuses on the physics of the interaction between the laser beam and a pre-formed plasma. Laser Plasma Interaction (LPI) is of critical importance to ICF. During the compression phase of indirect drive, the laser passes through the plasma filling the Hohlraum. In direct drive, the beam must traverse the rapidly expanding target corona. In these circumstances the behaviour of the incident light and its coupling to the plasma has serious implications for the efficiency and practicality of ICF.

The EMW can excite a number of instabilities in the plasma. Incident light may be scattered from longitudinal plasma waves, resulting in back propagating EMWs

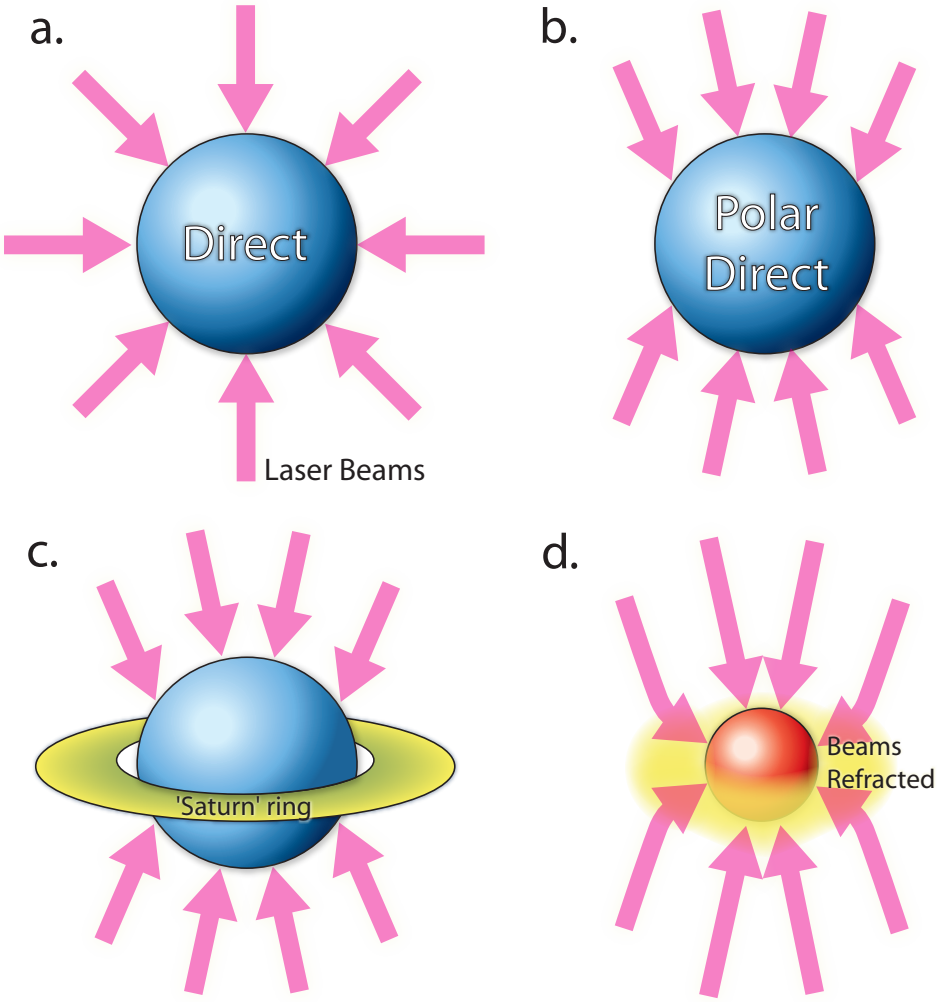

Figure 1.7: **a.** Direct drive ICF by symmetric irradiation with long-pulse beams. **b.** Facilities configured for radiative implosion, using a Hohlraum, may be able to ignite a fuel pellet directly without significant reconfiguration. The Polar Direct Drive scheme aims to achieve a sufficient degree of symmetry by pointing some beams off target centre and reducing their power. The outermost beams will be refracted by the expanding corona once the implosion phase has begun, leading to an improvement in drive symmetry. **c, d.**This effect may be enhanced by the addition of a plastic 'Saturn' ring around the target's equator.

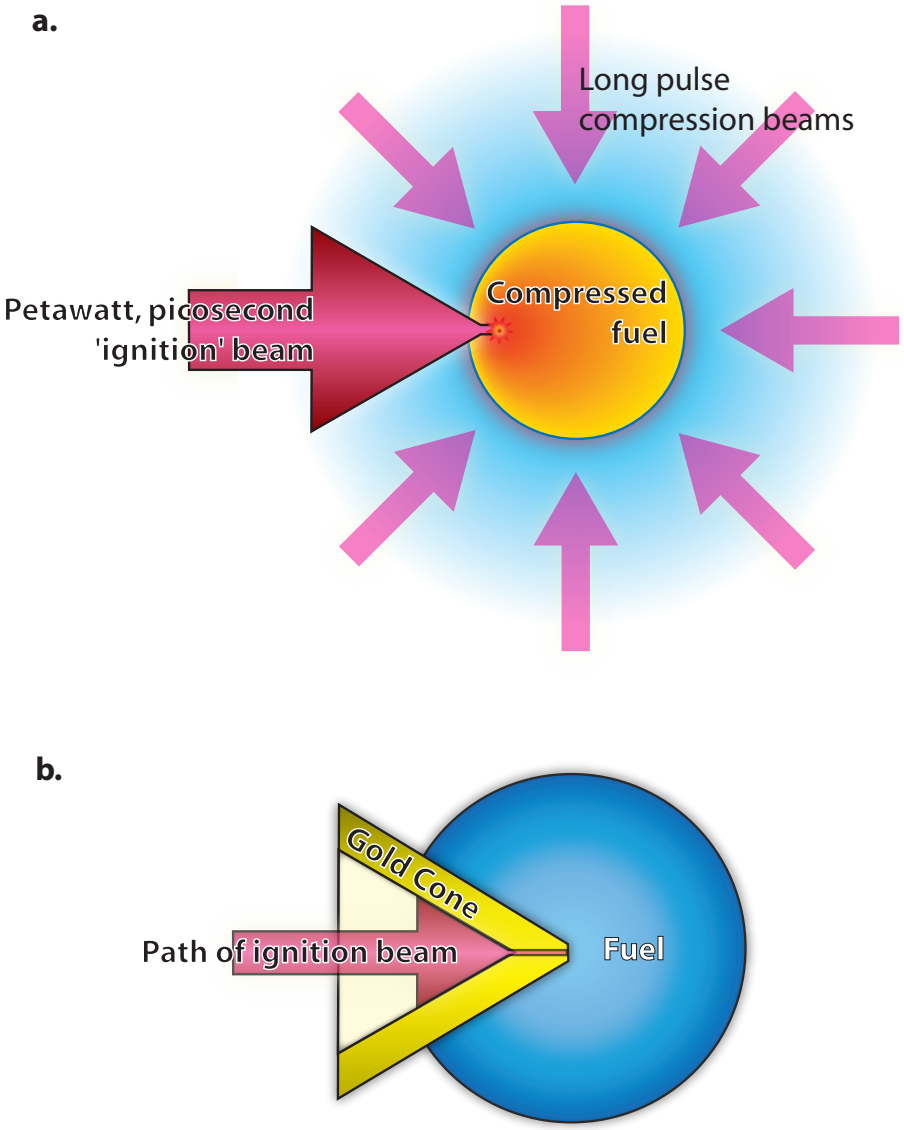

Figure 1.8: In Fast Ignition, the tasks of compression and ignition are performed by two separate systems. **a.** Long-pulse laser beams compress the fuel, much like direct drive. A small region of the compressed core is then heated by the deposition of relativistic electrons produced by a picosecond, petawatt beam. **b.** A hollow gold cone has been used in experiments to allow the ignition beam to traverse the corona.

and fast-moving particle populations. Scattering can destroy the radiation symmetry, impact efficiency by reducing the energy delivered on target and potentially damage optics and diagnostics. Accelerated electrons can pre-heat the fuel core, increasing the energy required for compression.

These processes are inherently non-linear and the coupling of the plasma with EMWs is often studied numerically. There are a number of models which can be used to simulate the interaction of lasers with plasma; each has its strengths and weaknesses. They must strike a balance between the complexity of the physics included and the spatial/temporal extent over which they may be applied.

Fluid models are capable of modeling spatially extensive systems, in two and three dimensions but their relative simplicity is a weakness when considering such highly non-linear systems. Fluid models can be augmented by results from experiment or more complex models, but this does not entirely overcome their inherent limitations.

Kinetic models adopt a statistical treatment of the plasma retaining information about the distribution of particle momenta. In addition to the conventional spatial dimensions, a kinetic model may have up to three velocity dimensions. Together, these describe a phase space of up to six dimensions. The complexity of such models allows a more accurate treatment of LPI, but renders problems analytically and computationally challenging. The Vlasov equation is crucial to kinetic numerical simulations of LPI. It can be solved, together with the appropriate equations of electrodynamics, either directly or via particle in cell (PIC) methods. While the PIC approach is widely adopted, it is inherently noisy in phase space, particularly in regions where the number of macroparticles is low. As a result, PIC methods cannot achieve the high resolutions possible by direct solution of the Vlasov equation.

Here, the principal equations of the fluid and kinetic models are detailed, and some implications discussed. The direct solution of the Vlasov equation will later be considered in detail as a method for modeling LPI and related phenomena.

1.4.1 Fluid Models: The Zakharov Approach

The plasma is treated as two interpenetrating fluids: the ion fluid and the electron fluid. The basis for modeling these fluids is hydrodynamic theory.

Hydrodynamics

For a fluid with mass density $\rho(\mathbf{x}, t)$ and velocity $\mathbf{u}(\mathbf{x}, t)$, the conservation of mass is embodied by the continuity equation

$$\frac{\partial \rho}{\partial t} + \nabla \cdot (\rho \mathbf{u}) = 0. \tag{1.3}$$

Conservation of momentum is expressed as

$$\rho \frac{D\mathbf{u}}{Dt} = -\nabla P + \mathbf{F} \tag{1.4}$$

where $\frac{D\mathbf{u}}{Dt} = \frac{\partial \mathbf{u}}{\partial t} + (\nabla \cdot \mathbf{u})\mathbf{u}$ is the convective derivative, P is the pressure and $\mathbf{F}$ represents the volume forces acting on the fluid.

Plasma as a fluid

The two fluid model is based on the hydrodynamic equations for an ion fluid (density ρ_i, velocity $\mathbf{v}_i$) and an electron fluid (density ρ_e, velocity $\mathbf{v}_e$) together with Maxwell's equations. The force term $\mathbf{F}$ is given by the Lorentz force $q(\mathbf{E} + \mathbf{v} \wedge \mathbf{B})$. Treating each fluid as an ideal gas

$$P_{e,i} = n_{e,i} \kappa T_{e,i} \tag{1.5}$$

where κ is Boltzmann's constant and $n_{e,i}$ represents the particle number density. Together with the isentropic equation $P_{e,i} = C n_{e,i}^{\gamma_{e,i}}$, where C is a function of the entropy and $\gamma_{e,i}$ is the adiabatic exponent, the pressure gradient in the hydrodynamic equations becomes

$$\nabla P_{e,i} = P_{e,i} \gamma_{e,i} \left(\frac{\nabla n_{e,i}}{n_{e,i}} \right) = \gamma_{e,i} \kappa T_e \nabla n_{e,i} \tag{1.6}$$

An additional term of the form $\nu_{e,i} \mathbf{v_{e,i}}$ is added to the momentum equations to represent the effect of collisional and/or Landau damping (see section 1.4.4). Terms of the form

$\nu_{ei}(\mathbf{v_e} - \mathbf{v_i})$ may be used to represent electron-ion collisions.

The two-fluid model thus consists of: two continuity equations

$$\frac{\partial n_{e,i}}{\partial t} + \nabla \cdot (n_{e,i}\mathbf{v_{e,i}}) = 0 \tag{1.7}$$

and two momentum equations

$$\frac{\partial \mathbf{v_{e,i}}}{\partial t} + (\mathbf{v_{e,i}} \cdot \nabla)\,\mathbf{v_{e,i}} + \frac{\gamma_{e,i}\kappa T_{e,i}}{n_{e,i}m_{e,i}}\nabla n_{e,i} + \nu_{e,i}\mathbf{v_{e,i}} = \frac{q_{e,i}}{m_{e,i}}\left(\mathbf{E} + \mathbf{v_{e,i}} \wedge \mathbf{B}\right) \tag{1.8}$$

closed by Maxwell's equations

$$\nabla \wedge \mathbf{B} = \mu_0\mathbf{J} + \frac{1}{c^2}\frac{\partial \mathbf{E}}{\partial t} \tag{1.9}$$

$$\nabla \wedge \mathbf{E} = \frac{\partial \mathbf{B}}{\partial t}. \tag{1.10}$$

The current density is given by $\mathbf{J} = -e\,(n_e\mathbf{v_e} - n_i\mathbf{v_i})$.

These basic equations are the starting point for a model of the evolution of wave amplitudes in laser-plasma instabilities. Two separate time-scales naturally arise in the system as a result of the difference between the ion and electron mass. This allows all the key variables to be split into fast and slow time-scale components. For example, the electron and ion densities can be written

$$n_i = n_0 + \delta n_i \tag{1.11}$$

$$n_e = n_0 + \delta n_e + \tilde{n}_e. \tag{1.12}$$

Here, $\tilde{n}_e$ represents the fast-timescale perturbations to the electron density while δn_e and δn_i represent the slow timescale perturbations to the electron and ion densities. At this timescale, the electrons are able to respond to electrical fields so fast that they can keep the plasma almost exactly electrically neutral. This is expressed through the quasineutrality condition $\delta n_e \simeq \delta n_i = \delta n$. In similar notation, the electric field and the fluid velocities are

$$\mathbf{E} = \mathbf{E_{slow}} + \tilde{\mathbf{E}} \tag{1.13}$$

$$\mathbf{v_e} = \delta\mathbf{v_e} + \tilde{\mathbf{v}}_\mathbf{e} \tag{1.14}$$

$$\mathbf{v_i} = \delta\mathbf{v_i}. \tag{1.15}$$

Using this two-timescale, two-fluid model gives, for the fast time-scale variables

$$\frac{\partial^2 \tilde{\mathbf{E}}}{\partial t^2} + \omega_{pe}^2 \left(1 + \frac{\delta n}{n_0}\right) \tilde{\mathbf{E}} - 3v_{Te}^2 \nabla \left(\nabla \cdot \tilde{\mathbf{E}}\right) + c^2 \nabla \wedge \left(\nabla \wedge \tilde{\mathbf{E}}\right) = 0 \tag{1.16}$$

Linearising this expression, in particular neglecting terms in $\delta n \tilde{E}$, yields the dispersion relation for electron plasma waves, or Langmuir waves.

$$\omega^2 = \omega_{pe}^2 + 3v_{Te}^2 k^2 \tag{1.17}$$

Equation (1.16) can be written in terms of the slowly varying amplitude of the fast-timescale electric field, $\bar{\mathbf{E}}$. This is defined by $\tilde{\mathbf{E}}(\mathbf{x}, t) = 0.5(\bar{\mathbf{E}}(\mathbf{x}, t) \exp(-i\omega_{pe} t) + \bar{\mathbf{E}}^*(\mathbf{x}, t) \exp(i\omega_{pe} t))$. Since $\bar{\mathbf{E}}$ is slowly varying, the second derivative in Eq.(1.16) can be neglected, giving the first Zakharov Equation

$$-2i\omega_{pe} \frac{\partial \bar{\mathbf{E}}}{\partial t} - 3v_{Te}^2 \nabla \left(\nabla \cdot \bar{\mathbf{E}}\right) + c^2 \nabla \wedge \left(\nabla \wedge \bar{\mathbf{E}}\right) + \omega_{pe}^2 \frac{\delta n}{n_0} \bar{\mathbf{E}} = 0. \tag{1.18}$$

This shows the coupling of the slowly varying amplitude of the rapidly oscillating electric field ($\bar{\mathbf{E}}$) to the slowly varying local number density (δn). A similar consideration of the slow-timescale components gives the second Zakharov equation:

$$\left(\frac{\partial^2}{\partial t^2} - c_S^2 \nabla^2\right) \delta n = \frac{\epsilon_0}{4m_i} \nabla^2 |\bar{\mathbf{E}}^2|. \tag{1.19}$$

This also involves only $\bar{\mathbf{E}}$ and δn, giving a closed system which must be solved self-consistently. The non-linear right-hand-side of the second Zakharov equation, proportional to $\nabla^2 |\bar{\mathbf{E}}|^2$, is referred to as the ponderomotive force. Although it has the same form, it is not actually a radiation pressure and can be written in the same way for longitudinal and transverse fields (where it is due to the $\mathbf{v} \wedge \mathbf{B}$ force). In laser plasma interactions, the ponderomotive force generated by the laser is responsible for cavitation and filamentation and also forms a vital part of many particle acceleration schemes [11]. In many fluid based models for LPI, the laser-plasma coupling is resolved via the ponderomotive force, rather than the direct interaction of the transverse fields.

The Zakharov treatment has some advantages for simulations of laser-plasma interaction since it is relatively undemanding in terms of computational resources. The literature contains many examples [12, 13, 14] of solving the Zakharov equations for laser

plasma instabilities. There are some considerable approximations made in the Zakharov model, mainly the assertion of a two-timescale plasma and the assumption that the plasma fits a perfect Maxwellian distribution. Models based on a Zakharov, or similar, two-fluid treatment have some significant problems. Most importantly, the damping rates, $\nu_{e,i}$, in Eq.(1.16) are not self-consistently determined within the Zakharov model unless both ion and electron distribution functions remain Maxwellian.

1.4.2 Kinetic Theory: The Vlasov Approach

Kinetic theory avoids many of the assumptions required for a fluid model, describing the plasma via a statistical treatment which retains information about particle velocities rather than averaging over them. In addition to physical dimensions, kinetic theory also considers three velocity dimensions, with particles evolving with time through a six dimensional 'phase space'. The following section describes the derivation of the Plasma Kinetic Equation. This equation is an exact kinetic description of the plasma in which the collisional and non-collisional aspects are treated separately.

Individual Particle Dynamics

The derivation begins by considering the motion of a single particle, charge q, mass m in external electric, $\mathbf{E}$, and magnetic, $\mathbf{B}$, fields. The equations of motion for this particle are

$$\frac{d\mathbf{X}(t)}{dt} = \mathbf{V}(t) \tag{1.20}$$

$$\frac{d\mathbf{V}(t)}{dt} = \frac{q}{m}\left(\mathbf{E}(\mathbf{X}(t),t) + \mathbf{V}(t) \wedge \mathbf{B}(\mathbf{X}(t),t)\right) \tag{1.21}$$

where the particle's position and velocity, as functions of time, t, are given by $\mathbf{X}(t)$ and $\mathbf{V}(t)$ respectively. As t varies, $\mathbf{X}$ and $\mathbf{V}$ describe the particle's trajectory in the six-dimensional phase-space $(\mathbf{x}, \mathbf{v})$, where $\mathbf{x}$ and $\mathbf{v}$ represent spatial and velocity space coordinates, independent of time. Figure 1.9 shows a hypothetical particle trajectory through a simplified phase space with only one spatial and one velocity dimension. The particle is assumed to be described by Dirac delta functions with the number density of

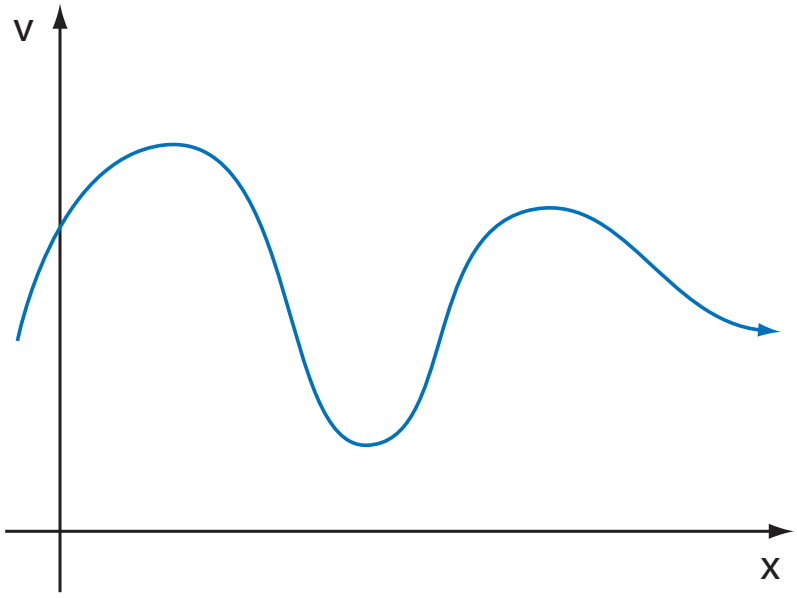

Figure 1.9: Hypothetical single particle trajectory through (x,v) phase space in the presence of external electric and magnetic fields.

particles, N, given by:

$$N(\mathbf{x},\mathbf{v},t) = \delta(\mathbf{x}-\mathbf{X}(t))\delta(\mathbf{v}-\mathbf{V}(t)), \tag{1.22}$$

where the total number density over the complete phase space, in this single particle system, is unity:

$$\int N(\mathbf{x},\mathbf{v},t)d\mathbf{x}d\mathbf{v} = 1. \tag{1.23}$$

In a system of n particles, each particle (denoted by $i = 1, 2, \cdots, n$) obeys equations of motion like those given in Eqs.(1.20) and (1.21):

$$\frac{d\mathbf{X}^i(t)}{dt} = \mathbf{V}^i(t) \tag{1.24}$$

$$\frac{d\mathbf{V}^i(t)}{dt} = \frac{q}{m}\left(\mathbf{E}^i(\mathbf{X}^i(t),t) + \mathbf{V}^i(t)\wedge\mathbf{B}^i(\mathbf{X}^i(t),t)\right) \tag{1.25}$$

where the particle number density is given by

$$N(\mathbf{x},\mathbf{v},t) = \sum_{i=1}^{n}\left[\delta(\mathbf{x}-\mathbf{X}^i(t))\delta(\mathbf{v}-\mathbf{V}^i(t))\right]. \tag{1.26}$$

The electric and magnetic fields are now given by self-consistent solutions of Maxwell's equations, rather than being externally prescribed:

$$\nabla\cdot\mathbf{E} = \frac{\rho(\mathbf{x},t)}{\epsilon_0} \tag{1.27}$$

$$\nabla\cdot\mathbf{B} = 0 \tag{1.28}$$

$$\nabla\wedge\mathbf{E} = -\frac{\partial\mathbf{B}}{\partial t} \tag{1.29}$$

$$\nabla\wedge\mathbf{B} = \mu_0\mathbf{J} + \epsilon_0\mu_0\frac{\partial\mathbf{E}}{\partial t}. \tag{1.30}$$

The charge density, ρ and current density $\mathbf{J}$ are given by

$$\rho(\mathbf{x},t) = q\int N(\mathbf{x},\mathbf{v},t)d\mathbf{v} \tag{1.31}$$

$$\mathbf{J}(\mathbf{x},t) = q\int \mathbf{v}N(\mathbf{x},\mathbf{v},t)d\mathbf{v}. \tag{1.32}$$

This completes the 'N-body' problem for charged particles. It is an exact kinetic model for the dynamics of a single charged particle species and is easily extended to multiple species. While the single particle dynamics have tractable analytic solutions, the N-body problem does not. In addition, as particle numbers are increased the problem rapidly becomes computationally unfeasible.

The Klimontovich Equation

The next step towards a usable kinetic model for the plasma is the Klimontovich equation, which is derived directly from the N-body model without simplification. Considering the time derivative of the particle density, Eq.(1.26) and using the chain rule to write $\frac{d}{dt}\delta(\mathbf{x}-\mathbf{X}^i) = \frac{d\mathbf{X}^i}{dt}\cdot\nabla_{X^i}\delta(\mathbf{x}-\mathbf{X}^i)$, gives

$$\begin{aligned}\frac{\partial N(\mathbf{x},\mathbf{v},t)}{\partial t} &= \sum_{i=1}^{n}\left[\frac{d\mathbf{X}^i}{dt}\cdot\nabla_{X^i}\delta(\mathbf{x}-\mathbf{X}^i)\delta(\mathbf{v}-\mathbf{V}^i)\right.\\ &+ \left.\frac{d\mathbf{V}^i}{dt}\cdot\nabla_{V^i}\delta(\mathbf{x}-\mathbf{X}^i)\delta(\mathbf{v}-\mathbf{V}^i)\right]. \qquad (1.33)\end{aligned}$$

Now, since $\partial_a f(a-b) = -\partial_b f(a-b)$, the derivatives in $\mathbf{X}^i$ and $\mathbf{V}^i$ can be replaced with derivatives in terms of the coordinates, $\mathbf{x}$ and $\mathbf{v}$, hence

$$\begin{aligned}\frac{\partial N(\mathbf{x},\mathbf{v},t)}{\partial t} &= -\sum_{i=1}^{n}\left[\frac{d\mathbf{X}^i}{dt}\cdot\nabla_{x}\delta(\mathbf{x}-\mathbf{X}^i)\delta(\mathbf{v}-\mathbf{V}^i)\right.\\ &+ \left.\frac{d\mathbf{V}^i}{dt}\cdot\nabla_{v}\delta(\mathbf{x}-\mathbf{X}^i)\delta(\mathbf{v}-\mathbf{V}^i)\right]. \qquad (1.34)\end{aligned}$$

The equations of motion for the N-body problem, Eqs.(1.24) and (1.25), are now substituted into Eq.(1.34):

$$\begin{aligned}&\frac{\partial N(\mathbf{x},\mathbf{v},t)}{\partial t} =\\ -\;&\sum_{i=1}^{n}\left[\mathbf{V}^i\cdot\nabla_x\delta(\mathbf{x}-\mathbf{X}^i)\delta(\mathbf{v}-\mathbf{V}^i)\right]\\ -\;&\sum_{i=1}^{n}\left[\frac{q}{m}\left(\mathbf{E}^i(\mathbf{X}^i,t)+\mathbf{V}^i\wedge\mathbf{B}^i(\mathbf{X}^i,t)\right)\cdot\nabla_v\delta(\mathbf{x}-\mathbf{X}^i)\delta(\mathbf{v}-\mathbf{V}^i)\right]. \qquad (1.35)\end{aligned}$$

The relation $a\delta(a-b) = b\delta(a-b)$ allows all references to the exact particle positions and velocities, $\mathbf{X}^i$ and $\mathbf{V}^i$, outside of the delta functions to be replaced with $\mathbf{x}$ and $\mathbf{v}$:

$$\begin{aligned}&\frac{\partial N(\mathbf{x},\mathbf{v},t)}{\partial t} =\\ -\;&\mathbf{v}\cdot\nabla_x\sum_{i=1}^{n}\left[\delta(\mathbf{x}-\mathbf{X}^i)\delta(\mathbf{v}-\mathbf{V}^i)\right]\\ -\;&\frac{q}{m}\left(\mathbf{E}(\mathbf{x},t)+\mathbf{v}\wedge\mathbf{B}^i(\mathbf{x},t)\right)\cdot\nabla_v\sum_{i=1}^{n}\left[\delta(\mathbf{x}-\mathbf{X}^i)\delta(\mathbf{v}-\mathbf{V}^i)\right]. \qquad (1.36)\end{aligned}$$

Using Eq.(1.26) to complete the remaining sums yields the Klimontovich equation

$$\frac{\partial N}{\partial t} + \mathbf{v} \cdot \nabla_x N + \frac{q}{m} (\mathbf{E} + \mathbf{v} \wedge \mathbf{B}) \cdot \nabla_v N = 0 \tag{1.37}$$

where the electric and magnetic fields are again solved via Maxwells equations. The Klimontovich equation follows directly from the N-body model without assumption or approximation. The complete dynamics of each particle in the system are still considered; for this reason it is no easier to use than the N-body problem.

The Particle Distribution Function

In order to make further progress, a more flexible description of the particle phase space is required. The Klimontovich equation describes the location of particles in phase space as a collection of delta functions at n exact locations $(\mathbf{X}^i, \mathbf{V}^i)$, given by the function N. A more useful approach is to treat the location of particles in phase space as a continuous function, the distribution function. This is shown schematically in Fig.1.10. It follows from the definition of N that $N d\mathbf{x} d\mathbf{v}$ is the number of particles in the range $(\mathbf{x}, \mathbf{x} + d\mathbf{x}), (\mathbf{v}, \mathbf{v} + d\mathbf{v})$ where $\int N d\mathbf{x} d\mathbf{v} = n$. The distribution function, f, is a smoothed, continuous representation of N such that $f d\mathbf{x} d\mathbf{v}$ the expected number of particles in the volume element, rather than the exact number. Thus

$$f(\mathbf{x}, \mathbf{v}, t) \equiv \langle N(\mathbf{x}, \mathbf{v}, t) \rangle \tag{1.38}$$

where $\langle \cdots \rangle$ represents the ensemble average. The electric and magnetic fields are replaced by similarly smoothed functions. As explained below, these smoothed functions can be substituted into the Klimontovich equation and the difference between the exact and the smooth descriptions attributed to effects such as discrete particle collisions.

The Plasma Kinetic Equation

The distribution function does not contain information about the discrete nature of the particles. Writing the difference between N and f as δN gives

$$N(\mathbf{x}, \mathbf{v}, t) = f(\mathbf{x}, \mathbf{v}, t) + \delta N(\mathbf{x}, \mathbf{v}, t) \tag{1.39}$$

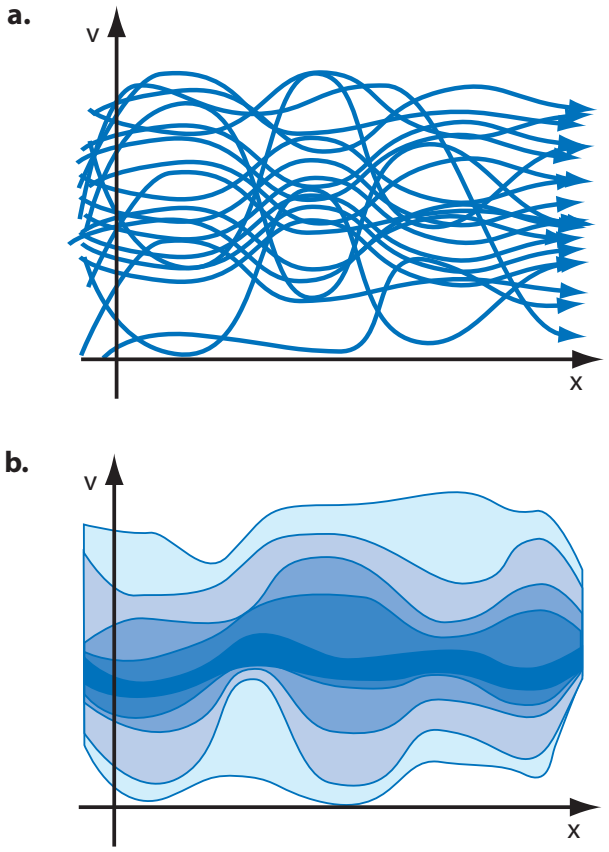

Figure 1.10: **a.** Hypothetical particle phase space for a many-particle system. **b.** The exact particle locations are replaced with smoothed continuous distribution function. Isocontours enclose regions of constant phase space volume.

where δN represents the contribution from discrete particle interactions. Similarly, $\mathbf{E}$ and $\mathbf{B}$ are written in terms of a smoothed component, corresponding to f, and a correction, $\delta\mathbf{E}$ and $\delta\mathbf{B}$

$$\mathbf{E}(\mathbf{x},t) = \mathbf{E_0}(\mathbf{x},t) + \delta\mathbf{E}(\mathbf{x},t) \quad (1.40)$$

$$\mathbf{B}(\mathbf{x},t) = \mathbf{B_0}(\mathbf{x},t) + \delta\mathbf{B}(\mathbf{x},t). \quad (1.41)$$

Where $f = \langle N\rangle$, $\mathbf{E_0} = \langle\mathbf{E}\rangle$, $\mathbf{B_0} = \langle\mathbf{B}\rangle$, $\langle\delta N\rangle = \langle\delta\mathbf{E}\rangle = \langle\delta\mathbf{B}\rangle = 0$, this gives the plasma kinetic equation

$$\frac{\partial f}{\partial t} + \mathbf{v}\cdot\nabla_x f + \frac{q}{m}\left(\mathbf{E_0} + \mathbf{v}\wedge\mathbf{B_0}\right)\cdot\nabla_v f = -\frac{q}{m}\left\langle\left(\delta\mathbf{E} + \mathbf{v}\wedge\delta\mathbf{B}\right)\cdot\nabla_v\delta N\right\rangle \quad (1.42)$$

Terms concerned with the discrete nature of the particles are grouped on the right hand side. The Vlasov equation can now be derived directly from the kinetic equation by neglecting the effects of collisions.

1.4.3 The Vlasov Equation

The plasma kinetic equation, Eq.(1.42), can be written as

$$\frac{\partial f}{\partial t} + \mathbf{v}\cdot\nabla_x f + \frac{q}{m}\left(\mathbf{E}_0 + \mathbf{v}\wedge\mathbf{B}_0\right)\cdot\nabla_v f = \left(\frac{\partial f}{\partial t}\right)_c \quad (1.43)$$

where $\left(\frac{\partial f}{\partial t}\right)_c$ represents any residual contribution from collisions to the rate of change of the distribution function f. The left hand side of Eq.(1.43) is the rate of change in f due to the smooth self-consistent fields $\mathbf{E}_0$ and $\mathbf{B}_0$, and has a characteristic timescale τ_0. If collisions have a characteristic timescale of τ_c, the right hand side of Eq.(1.43) can be neglected for

$$\frac{f}{\tau_0} \gg \frac{f}{\tau_c} \Rightarrow \tau_c \gg \tau_0. \quad (1.44)$$

That is, collisions can be ignored for processes on timescales shorter than the average time between collisions.

The derivation for the plasma kinetic equation (Eq.(1.42)) given here, demonstrates the natural progression from single particle dynamics to many particles, onto the Klimontovich equation, the concept of the particle distribution function, separation of

collisional and non-collisional effects, and finally the plasma kinetic equation. In moving from the N-body problem to the kinetic equation, it is not necessary to make any approximations or introduce any assumptions; the kinetic equation represents an exact kinetic model. Vlasov's equation dispenses with the collisional terms to give

$$\frac{\partial f}{\partial t} + \mathbf{v} \cdot \nabla_x f + \frac{q}{m} (\mathbf{E} + \mathbf{v} \wedge \mathbf{B}) \cdot \nabla_v f = 0. \tag{1.45}$$

Vlasov's Equation in LPI

The Vlasov equation for a two, or more, component plasma in the presence of a laser field can be solved numerically. This allows the accurate representation and evolution of the particle phase space for laser-plasma systems where the collision terms can be neglected. In practice, the Vlasov model can be used to study LPI as the laser traverses the low-Z gas fill of the Hohlraum or the corona of expanding fuel [34]. In these cases, the relevant timescale is the electron-ion collision time, derived by considering a Coulomb deflection of a test electron by a background ion [29]:

$$\tau_c = \tau^{ei} = \left(\frac{3\sqrt{6}}{8} \right) \frac{\sqrt{m_e} \left(\kappa T_e \right)^{3/2}}{\pi Z^4 e^4 n_i \ln \Lambda}. \tag{1.46}$$

Where τ_c is given in seconds, T_e in degrees Kelvin and n_i in cm^{-3}. Taking $Z = 1$ with a temperature $\approx 4 \times 10^6 \mathrm{K}$ (or $350 \mathrm{eV}$) and number density $\approx 10^{20} \mathrm{cm}^{-3}$, this corresponds to a collision time of slightly less than one nanosecond. Shorter than the timescale for ignition of an ICF target but considerably longer than the timescale over which the salient kinetic features in a single hotspot in the Hohlraum gas fill or target corona would be expected to evolve [49].

The Vlasov model allows a detailed study of the laser plasma interaction physics, in particular the appearance, growth and non-linear saturation of instabilities. Generally, the temporal and spatial extent of such studies is limited - both by the assumption of a collision-less plasma and the computational demands. However, the insight gained by retaining such detailed kinetic information can be used together with hydrodynamic, radiation-hydrodynamic and collisional codes to better describe the processes involved in ICF.

Moments of Vlasov's Equation

The zeroth, first and second order moments of the particle distribution function give the particle density

$$n(\mathbf{x},t) = \int f(\mathbf{x},\mathbf{v},t)d\mathbf{v} \tag{1.47}$$

the fluid velocity

$$\mathbf{u}(\mathbf{x},t) = \frac{1}{n(\mathbf{x},t)} \int \mathbf{v} f(\mathbf{x},\mathbf{v},t)d\mathbf{v} \tag{1.48}$$

and the stress tensor

$$P_{ij}(\mathbf{x},t) = \int m v_i v_j f(\mathbf{x},\mathbf{v},t)d\mathbf{v}. \tag{1.49}$$

Just as taking moment of the distribution function yields macroscopic physical quantities, moments of the Vlasov equation provide physical equations relating these quantities. For a system of mobile electrons and ions, the zeroth order moments give the continuity equation, first order the momentum equation and second order the energy equation. The system is closed by setting the third order moment, describing the thermal conductivity, to zero.

In essence, fluid plasma models, such as the two fluid model (see section 1.4.1) in un-magnetised plasmas and the equations of MHD [15] in magnetically dominated plasmas can be derived from kinetic theory by taking moments of the kinetic equations. Some simplifications are required, and the resulting models are devoid of the richness of information provided by the kinetic description.

1.4.4 Electrostatic Waves and Landau Damping

Considering only one dimensional electrostatic interaction for a system of mobile electrons (with charge $q = e$ and mass $m = m_e$) against a fixed ion background simplifies the Vlasov equation (Eq.(1.45)) to

$$\frac{\partial f}{\partial t} + v\frac{\partial f}{\partial x} - \frac{e}{m_e}E_x\frac{\partial f}{\partial v} = 0 \tag{1.50}$$

where v is the velocity component along x and $f = f(x,v,t)$ is the electron distribution function. Consider perturbations f_1, E_{x1} about a spatially uniform equilibrium, f_0, E_{x0}, such that $f(x,v,t) = f_0(v,t) + f_1(x,v,t)$ and $E_x = E_{x0} + E_{x1}$. In equilibrium $\int f_0 dv =$

$n_0 = n_i$, where n_i is the background ion density, and the electrostatic field is zero. Therefore $E_x \to 0$ as $f_1 \to 0$, and $E_x = E_{x1}$. Substituting into Eq.(1.50) gives a zeroth order equation:

$$\frac{\partial f_0}{\partial t} + v\frac{\partial f_0}{\partial x} = 0 \tag{1.51}$$

which is satisfied where f_0 is a Maxwellian distribution, and a first order equation:

$$\frac{\partial f_1}{\partial t} + v\frac{\partial f_1}{\partial x} - \frac{e}{m_e}E_{x1}\frac{\partial f_0}{\partial v} = 0. \tag{1.52}$$

Solving Poisson's equation gives the electrostatic field E_x:

$$\frac{\partial E_x}{\partial x} = \frac{e}{\epsilon_0}(n_i - n_e) \Rightarrow \frac{\partial E_{x1}}{\partial x} = -\frac{e}{\epsilon_0}\int f_1 dv \tag{1.53}$$

Searching for linear solutions of the form $\propto \exp(ikx - i\omega t)$, substitute $f_1(x,v,t) = f_1(v)\exp(ikx - i\omega t)$ and $E_{x1}(x,t) = E_{x1}\exp(ikx - i\omega t)$.

$$f_1 = \frac{ie}{m_e}\frac{1}{\omega - kv}E_{x1}\frac{\partial f_0}{\partial v} \tag{1.54}$$

$$ikE_{x1} = -\frac{e}{\epsilon_0}\int f_1 dv \tag{1.55}$$

Hence,

$$ikE_{x1} = -\frac{e^2}{\epsilon_0 m_e}\int \frac{1}{\omega/k - v}\frac{\partial f_0}{\partial v}dv \tag{1.56}$$

or

$$1 + \frac{e^2}{\epsilon_0 m_e k^2}\int \frac{\partial_v f_0}{\omega/k - v}dv = 0. \tag{1.57}$$

Normalising the distribution function to the background density, n_0, such that $g(v) = f_0(v)/n_0$ gives

$$1 + \frac{\omega_{pe}^2}{k^2}\int \frac{\partial_v g}{\omega/k - v}dv = 0 \tag{1.58}$$

where $\omega_{pe} = (n_0 e^2/\epsilon_0 m_e)^{1/2}$ is the electron plasma frequency, the natural mode of oscillation for a cold plasma [16].

However, the integral has a singularity in velocity space, at $v = \omega/k$ and therefore appears not to be well defined. A thorough consideration of the integral, treated first by Landau [17] as an initial value problem and solved via Laplace transformed along a prescribed inversion contour, shows the existence of a form of non-collisional kinetic damping known as Landau damping. The derivation given below follows the analytic continuation of the integrand along the contours described by the Landau prescription, rather than Landau's original approach.

Analytic Continuation and the Landau Contour

For complex frequencies, Eq.(1.58) is written as

$$\epsilon(k,\omega) = 1 + \frac{\omega_{pe}^2}{k^2}\int_C \frac{\partial_v g}{\omega/k - v}dv = 0 \tag{1.59}$$

where C represents a contour in the complex plane and $\epsilon(k,\omega)$ is the kinetic dispersion relation for electrostatic plasma waves; providing a relation between wavenumber and frequency. Without loss of generality fix $k > 0$ and continue to solve for ω. This requires the analytic continuation of the integrand. Provided $\frac{dg}{dv}$ can be treated as a complex function of complex v, as is certainly the case for a Maxwellian equilibrium particle distribution, the analytic continuation allows the domain of the integrand to be extended into the complex plane along the contour C. This contour is chosen according to the 'Landau Prescription', as shown in Fig.1.11 for the cases of $Im(\omega) < 0$, $Im(\omega) = 0$, and $Im(\omega) > 0$. These correspond to unstable exponential growth, undamped waves and damped waves respectively.

When ω is real or the singularity lies in the upper half of the complex plane, the Landau contour follows the path shown in Fig.1.11b or 1.11c respectively. In the limit as ω approaches the real axis, the integral in the dispersion relation is given by

$$\int_C \frac{\partial_v g}{\omega/k - v}dv = P\int_{-\infty}^{\infty} \frac{\partial_v g}{\omega/k - v}dv + \frac{\pi i}{k}\left(\frac{\partial g}{\partial v}\right)_{v=\omega/k} \tag{1.60}$$

where $-\frac{1}{k}\left(\frac{dg}{dv}\right)_{v=\omega/k}$ is the residue about $v = \omega/k$. If g decreases rapidly and monotonically with increasing v, reaching zero as $v \to \pm\infty$, then so will $\frac{dg}{dv}$. Writing ω as a sum of separate real and imaginary components, define ω_r, γ, such that $\omega = \omega_r + i\gamma$. Assuming γ is small in comparison to ω_r, the principal part of the integral can now be solved by replacing $(\omega/k - v)^{-1}$ with its Taylor expansion about $\omega = \omega_r$ and integrating by parts to give

$$\begin{aligned} P\int_{-\infty}^{\infty} \frac{\partial_v g}{\omega_r/k - v}dv &= \frac{k}{\omega_r}\int_{-\infty}^{\infty}\left(1 + \frac{kv}{\omega_r} + \left(\frac{kv}{\omega_r}\right)^2 + \cdots\right)\frac{dg}{dv}dv \\ &= -\frac{k^2}{\omega_r^2}\int_{-\infty}^{\infty} g\left(1 + 2\frac{kv}{\omega_r} + 3\left(\frac{kv}{\omega_r}\right)^2 + \cdots\right)dv. \end{aligned} \tag{1.61}$$

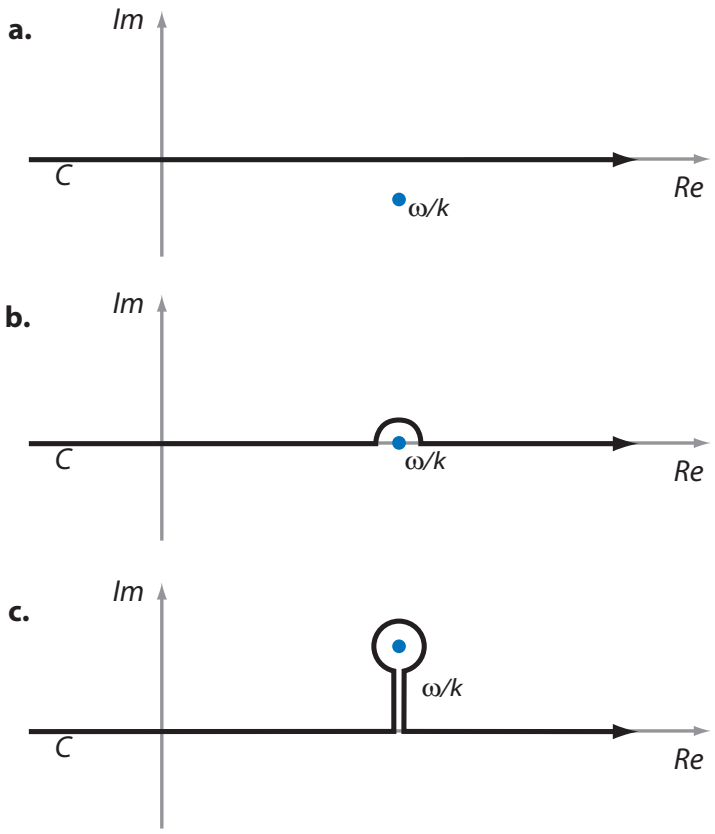

Figure 1.11: The Landau contour, C, in the complex plane for the cases; **a.** $Im(\omega) < 0$; **b.** $Im(\omega) = 0$; **c.** $Im(\omega) > 0$, representing a decaying field.

By definition, $\int g dv = 1$ and $\int m_e v^2 g dv = \kappa T$, where κ is the Boltzmann constant and T the temperature. Thus, to second order, Eq.(1.59) becomes

$$\epsilon(k,\omega) = 1 - \frac{\omega_{pe}^2}{\omega_r^2} - 3\left(\frac{k^2 \kappa T \omega_{pe}^2}{m_e \omega_r^4}\right) - \frac{e^2}{\epsilon_0 m_e}\frac{\pi i}{k^2}\left(\frac{dg}{dv}\right)_{v=\omega_r/k} \tag{1.62}$$

Equating the real parts of Eq.(1.62) yields the conventional dispersion relation $\omega_r^2 \approx \omega_{pe}^2(1 + 3k^2\lambda_D^2)$, where $\lambda_D = (\kappa T/m_e\omega_{pe}^2)^{1/2}$ is the Debye length [16]. Then the imaginary component of ω is given by

$$\gamma = -\frac{\pi e^2}{2\omega_{pe} k^2 \epsilon_0 m_e}\left(\frac{dg}{dv}\right)_{v=\omega_r/k} \tag{1.63}$$

For a Maxwellian velocity distribution, this becomes

$$\gamma = \frac{1}{2}\sqrt{\frac{\pi}{2}}\omega_{pe}\frac{1}{k^3\lambda_d^3}\exp\left(-1/(2k^2\lambda_d^2) - 3/2\right) \tag{1.64}$$

Since γ is the imaginary component of the frequency, this represents the damping of electrostatic waves. Landau damping, as it is called, is absent from fluid models of the plasma and describes a purely kinetic, non-collisional form of damping. As shown in Fig.1.12 Landau damping can be interpreted as a transfer of energy from the wave to the particles. Particles with velocity $v < v_p$ bunch in the accelerating region, and are accelerated, while particles with $v > v_p$ bunch in the decelerating region and are retarded. Provided $\frac{df}{dv} < 0$ initially, more electrons will gain energy from the wave than lose energy. As a result energy is transferred from the wave to the particles - effectively damping the wave.

1.4.5 BGK Modes

Landau damping is an example of a plasma phenomena which can only be understood with kinetic theory. A plasma can support complex and stable phase space structures which represent modes distinctly different from those in the fluid limit. A whole class of fully non-linear solutions to the Vlasov equation in a two component plasma can be found. These are often referred to as BGK modes after Bernstein, Greene and Kruskal, who were the first to develop an analytic treatment. This treatment explicitly relates the wave potential to the trapped and un-trapped particle distribution functions[18].

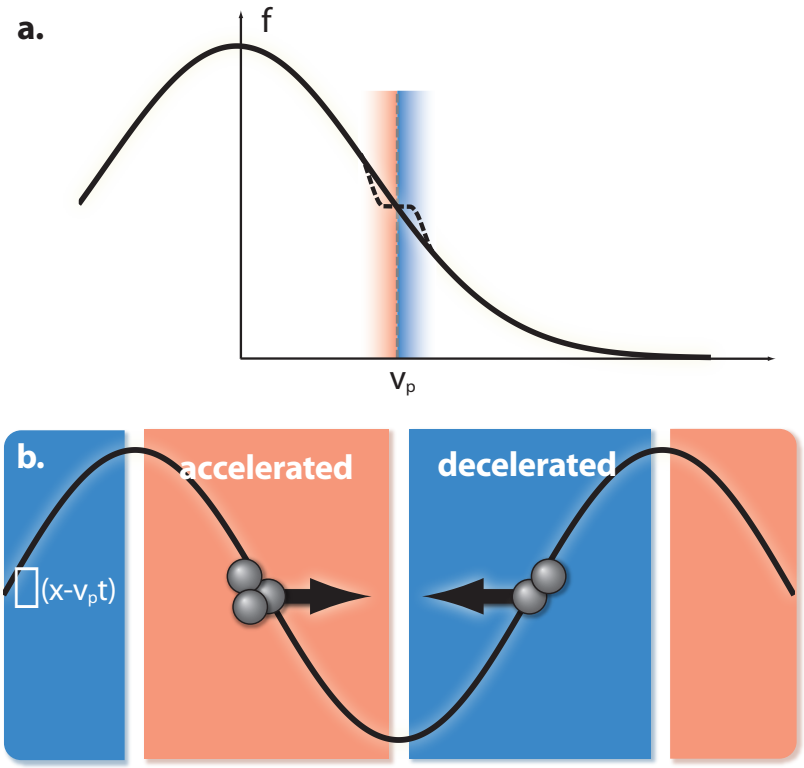

Figure 1.12: The physical origin of Landau damping, for an electrostatic wave with phase velocity v_p. **a**. shows the particle distribution function. **b.** The potential in the frame moving with the wave. Particles with velocity $v < v_p$ bunch in the accelerating region, and are accelerated, while particles with $v > v_p$ bunch in the decelerating region and are retarded. Provided $\frac{df}{dv} < 0$ initially, more electrons will gain energy from the wave than lose energy. As a result the wave energy falls; it is damped via a non-collisional interaction with the electron population. The process of acceleration and deceleration results in a flattening of the distribution function at v_p, shown by a dotted line in **a**.

The presence of 'buckets' in the particle phase space is a common characteristic of BGK modes. As shown in Fig.1.13, these structures, often referred to as 'phase space holes', represent trapped particles (within the hole) and un-trapped particles (outside the hole). BGK modes provide a mechanism for the existence of large amplitude plasma waves which are only weakly damped [19, 20, 21, 22]. They have been observed experimentally [23] and are believed to participate in LPI [24, 25]. Some systems [26] are entirely dominated by the appearance and evolution of BGK modes.

In themselves, BGK modes present a complex analytical and numerical problem [27], but in a dynamic kinetic system an accurate treatment of such phase space structures is vital.

1.5 Instabilities in Laser-Plasma Interaction

The interaction of a large amplitude electromagnetic field with a plasma leads to a variety of highly non-linear phenomena. The laser field can drive a number of distinct plasma instabilities in which the electromagnetic wave (EMW) couples to other plasma modes. Parametric Instabilities are characterised by a frequency matching condition between the driving and daughter waves and the existence of a threshold driving amplitude - below which no instability occurs. The most general example of a parametric instability is the coupled mode parametric excitation.

Coupled Mode Parametric Excitation

As a general model for parametric instabilities in plasmas, consider a large amplitude driving field coupled with two low amplitude daughter waves. It is assumed that the parent, or pump, wave is not depleted by the growth of the daughter waves. This assumption is inadequate for modeling parametric instabilities through their growth and saturation. However, as shown below, this model demonstrates the salient features of parametric instabilities - the feed-back loop and the existence of a driving threshold.
The fixed amplitude, homogenous pump field is given by

$$Z(t) = Z_0 \cos(\omega_Z t) \tag{1.65}$$

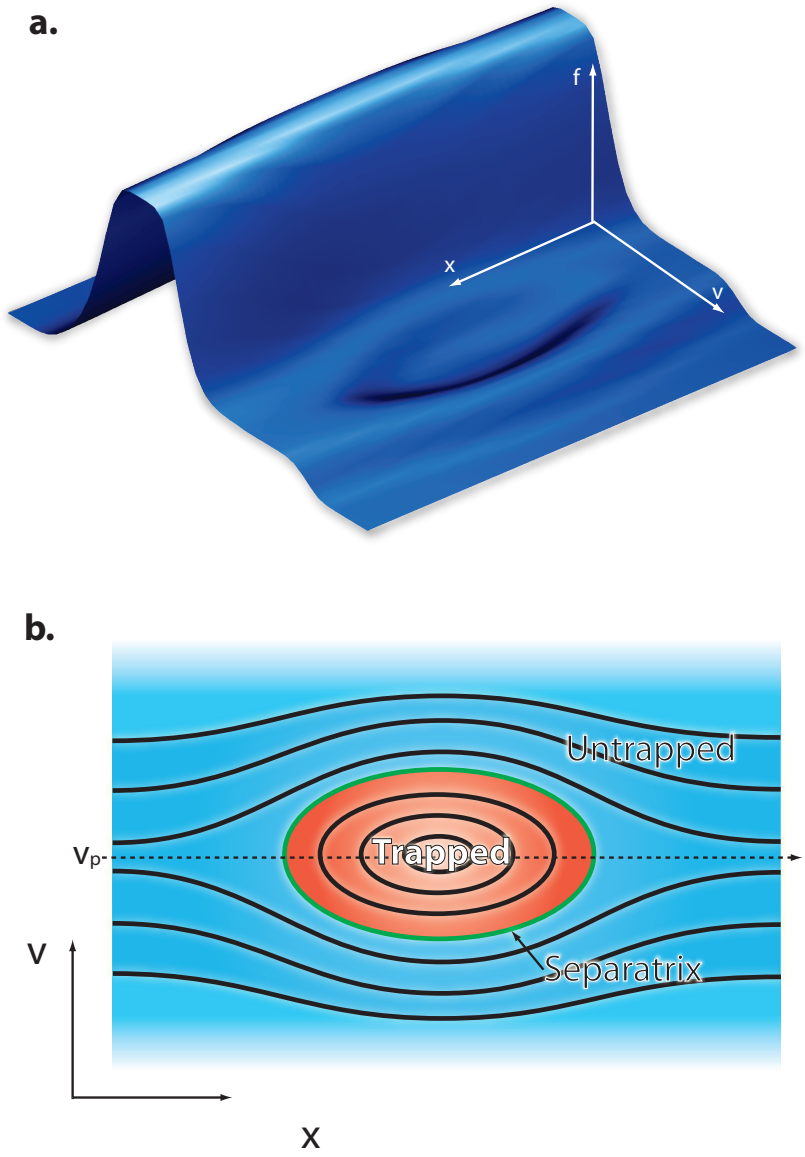

Figure 1.13: BGK modes are a class of non-linear solutions to the Vlasov equation in a two component plasma. **a.** The phase space hole, commonly observed in simulations is a form of BGK mode. **b.** The particle phase space is partitioned into regions where the particles are trapped by the wave potential, and regions where they are not. They are a phenomena absent from fluid treatments of the plasma.

The daughter waves are two natural oscillations, $X(t)$ and $Y(t)$. Adding non-linear coupling terms to the wave equations for $X(t)$ and $Y(t)$, with coupling coefficients c_X and c_Y gives

$$l_X X(t) = c_X Z(t) Y(t) \tag{1.66}$$

$$l_Y Y(t) = c_Y Z(t) X(t) \tag{1.67}$$

where the linear operators are given by

$$l_{X,Y} \equiv \frac{d^2}{dt^2} + \Gamma_{X,Y} \frac{d}{dt} + \omega_{X,Y}^2. \tag{1.68}$$

Here, $\Gamma_{X,Y}$ represents the damping rate for each mode. This forms a simple model for three wave coupling. The equations describe how the non-linear modulation of X (or Y) due to Z acts to produce forced oscillations in the daughter waves. When the pump wave is in resonance with the daughter waves

$$\omega_Z \approx \omega_X + \omega_Y. \tag{1.69}$$

Energy is transferred between the three waves. Consider the Fourier transforms of the coupled wave equations:

$$D_X(\omega) X(\omega) = c_X \frac{Z_0}{2} \{ Y(\omega + \omega_Z) + Y(\omega - \omega_Z) \} \tag{1.70}$$

$$D_Y(\omega \pm \omega_Z) Y(\omega \pm \omega_Z) = c_Y \frac{Z_0}{2} \{ X(\omega) + X(\omega \pm 2\omega_Z) \} \tag{1.71}$$

$$D_{X,Y}(\omega) = -\omega^2 - 2i\Gamma_{X,Y}\omega + \omega_{X,Y}^2 \tag{1.72}$$

If follows from Eq.(1.69) that the terms $X(\omega \pm 2\omega_Z)$ are not in resonance and can be neglected. The remaining terms show the coupling of $X(\omega)$ to $Y(\omega \pm \omega_Z)$, which in turn couples with $X(\omega)$ - creating a feed-back loop. Solving this system of equations, assuming a small frequency missmatch $\delta = \omega_Z - \omega_X - \omega_Y$ yields the characteristic parametric threshold for the pumping amplitude

$$Z_{0,th}^2 = \frac{\omega_X \omega_Y \Gamma_X \Gamma_Y}{c_X c_Y} \left(1 + \frac{4\delta^2}{(\Gamma_X + \Gamma_Y)^2} \right). \tag{1.73}$$

With a minimum value in the case of perfect frequency matching

$$Z_{0,min}^2 = \frac{\omega_X \omega_Y \Gamma_X \Gamma_Y}{c_X c_Y} \tag{1.74}$$

The threshold values only exist where the daughter waves are damped (i.e. Γ_x and Γ_Y are non-zero). The maximum growth rate Γ_{max} occurs for $\Gamma_{X,Y} = 0$ and $\delta = 0$ where

$$\Gamma_{max} = \left(\frac{c_X c_Y}{4\omega_X \omega_Y} \right)^{1/2} Z_0 \tag{1.75}$$

Instabilities in laser plasma systems behave in essentially the same manner, with a driving field coupled to daughter waves. It is possible to derive similar systems of wave equations linked by non-linear coupling terms that describe the evolution of various instabilities in plasmas, from the two fluid model [28, 29].

1.5.1 Parametric Instabilities in Plasmas

The unmagnetised plasma of a laser-plasma system can support a variety of wave modes, these are described below.

Electromagnetic Waves

The propagation of EMWs in a plasma is governed by the dispersion relation

$$\omega_E^2 = \omega_{pe}^2 + c^2 k^2. \tag{1.76}$$

However, unlike the vacuum, EMWs in a plasma are not free to take any frequency. They are restricted to $\omega_E > \omega_{pe}$ and cannot propagate at or below the plasma frequency. For the scenario where an EMW is incident on a plasma with $\omega_{pe} = \omega_E$, a wave travelling perpendicular to the plasma interface will be reflected. Where the incoming EMW is not perpendicular, there will be a mixture of reflection and resonant absorption [29, 30].

Langmuir Waves

These are sometimes referred to simply as electron plasma waves. Langmuir waves are collisionless, high frequency, longitudinal electrostatic waves which propagate in the form of a perturbation to the electron density only - the ions being too heavy to respond

to the rapidly oscillating field. The dispersion relation from the fluid treatment

$$\omega_L^2 = \omega_{pe}^2 + 3k^2 v_{Te}^2 \tag{1.77}$$

shows they are also unable to propagate below ω_{pe} and form standing waves at ω_{pe}. Furthermore, Langmuir waves can only propagate in warm plasmas, with finite temperatures. In the case of a cold plasma (where $T_e = T_i = 0$, and hence $v_{Te} = 0$) it must be the case that $\omega = \omega_{pe} \Rightarrow \frac{\omega}{k}, \frac{\partial \omega}{\partial k} = 0$ resulting in a stationary wave.

Ion Acoustic Waves

Like Langmuir waves, ion acoustic waves are collisionless longitudinal electrostatic waves. However, they are low frequency which means that, unlike Langmuir waves, the ions move - dragging the electron population with them. There are no resonances or cut-offs to restrict the propagation of ion-acoustic waves like those of electromagnetic and Langmuir waves. Consequently they follow a much simpler dispersion relation

$$\omega_S^2 = k^2 c_s^2 \tag{1.78}$$

where $c_s = \sqrt{\frac{\kappa(\gamma_e T_e + \gamma_i T_i)}{m_i}}$ is the ion acoustic velocity. On the time-scale of ion acoustic waves, it can be assumed that the electron population is able to respond immediately to any temperature variations - this will clearly not be the case for the ions. For example, in a one dimensional system, one would usually choose $\gamma_e = 1$, $\gamma_i = 3$, corresponding isothermal perturbations of the electrons and adiabatic perturbations of the ions.

A kinetic derivation follows a similar methodology to the derivation of the dispersion relation for electron plasma waves given in section 1.4.4. A kinetic consideration of the ion acoustic wave shows them to be critically Landau damped for the case of $T_e \approx T_i$ [28]. Assuming a phase velocity much greater than the ion thermal velocity, but much smaller than the electron thermal velocity, a kinetic treatment gives the following dispersion relation

$$\omega_S^2 = \kappa \frac{T_e}{m_i} \frac{k^2}{1 + k^2 \lambda_D^2} \tag{1.79}$$

for Maxwellian electron and ion velocity distributions. For $k\lambda_D \ll 1$ this simplifies to

$$\omega_S^2 = \kappa \frac{T_e}{m_i} k^2 \tag{1.80}$$

a dispersion relation much like that of an ordinary sound wave, with pressure provided by the electrons and inertia by the ions.

Matching conditions

As with the coupled mode parametric instability, consider a driving wave pumping energy into two daughter waves. For resonance, temporal and spatial phase matching demands that

$$\omega_1 \approx \omega_2 + \omega_3 \tag{1.81}$$

and

$$\mathbf{k_1} = \mathbf{k_2} + \mathbf{k_3}. \tag{1.82}$$

where the subscript '1' is used to denote the driver, while '2' and '3' denote the daughter waves.

With a driving EMW provided by the laser, this allows several different combinations of driver and daughter waves. The $(\omega, \mathbf{k})$ space can be treated as a two-dimensional plane (ω, k). While this is an over simplification (some instabilities are not feasible in only one spatial dimension) it allows the matching conditions to be described schematically as a simple vector diagram. These diagrams, shown in Fig.1.14, use the notation 'E' to represent EMWs, 'L' for Langmuir waves and 'S' for ion acoustic waves. The instabilities are described in full below.

1.5.2 The Critical Density

In ICF experiments the incident light typically encounters a ramped density profile (see Fig.1.15) created by the expansion of the outer layers of ablated material. The various instabilities described below typically occur at different points on the ramp, and some are prohibited at certain densities. The critical density n_c is the density at which the plasma frequency matches the frequency of the incident light $n_c = \frac{\omega^2 m_e \epsilon_0}{e^2}$. It is at this density that the laser energy is absorbed by the plasma.

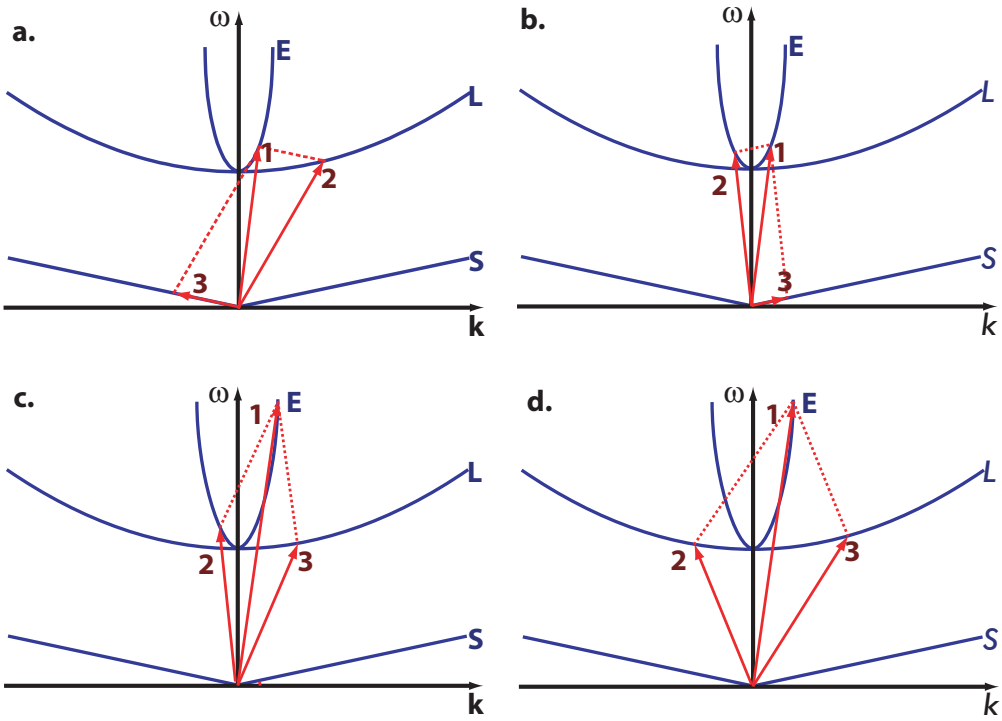

Figure 1.14: Three wave coupling for common parametric instabilities. '1' represents the driving wave while '2' and '3' represent the two daughter waves. **a.** The Parametric Instability. **b.** SBS. **c.** SRS. **d.** Two Plasmon Decay

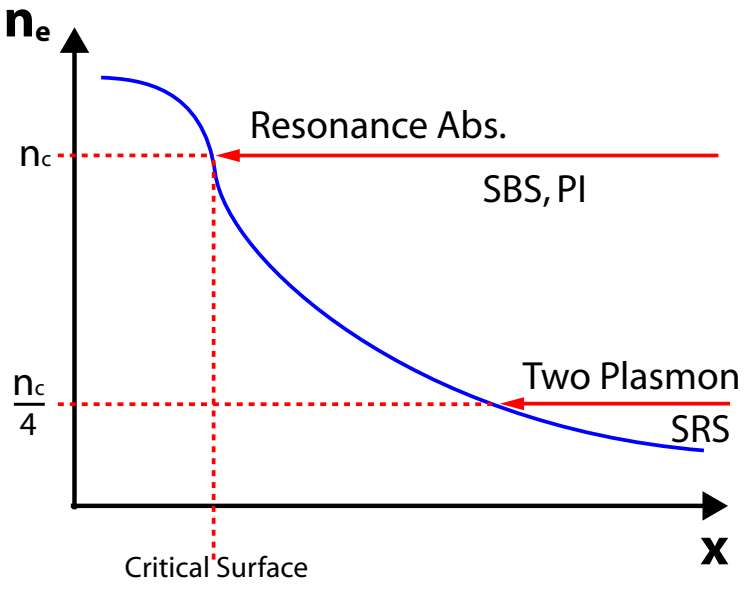

Figure 1.15: Typical density ramp from an ICF experiment. Absorption occurs at the critical density surface at $n = n_c$. SBS occurs for densities up to n_c and SRS for densities up to quarter critical. The parametric instability occurs near to the critical surface and two plasmon decay occurs near to $n = n_c$.

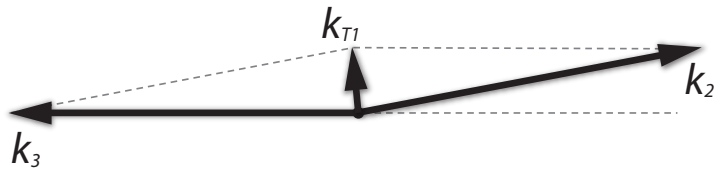

Figure 1.16: Diagrammatic representation of the k-matching between transverse electric field $\mathbf{k}_{T1}$ of the EM parent wave and the wavevectors of the two daughter waves $\mathbf{k}_2$ and $\mathbf{k}_3$. For the parametric instability, '2' and '3' represent Langmuir and ion acoustic waves respectively. For two plasmon decay, they represent two Langmuir waves and for two ion wave decay, two ion acoustic waves. This demonstrates the two-dimensional nature of these instabilities.

1.5.3 The Parametric Instability

E → L + S: The incident wave excites counter propagating Langmuir and ion acoustic waves. The transverse electric field of the pump wave must be able to couple to the longitudinal electric fields of the Langmuir and ion acoustic waves. This is only possible if the daughter waves are not exactly anti-parallel, as shown in Fig.1.16; as a result the process is two-dimensional. The parametric decay instability results in the conversion of EM energy into electrostatic modes of the plasma, and so enhances absorption. Since $\omega_S \ll \omega_{pe}$ and $\omega_L \approx \omega_{pe}$, the instability occurs where $\omega_E \approx \omega_{pe}$, that is at densities $n_e \approx n_c$.

1.5.4 Stimulated Brillouin Scattering

E → E + S: Often referred to simply as SBS. Here, the incident wave excites an ion acoustic wave which remains within the plasma and an EMW which propagates in the opposite direction to the driving wave. Since EMWs are able to propagate in free-space, the electromagnetic daughter wave is able to leave the plasma. Unlike the parametric instability, SBS can be modeled in one dimension, with the EM waves coupled to the ion wave via the ponderomotive force. Combining the various dispersion relations with

the frequency-matching condition gives the minimum frequency for SBS as $\omega_1 = \omega_{pe}$, corresponding to a maximum allowed density of $n_e = n_c$.

SBS can backscatter incident light before it reaches the critical surface, reducing efficiency and symmetry. The growth rate of SBS (in s^{-1}), for an incident intensity much greater than the threshold intensity is:

$$\Gamma_{sbs} = \frac{\omega_{pe}^2}{2\omega_0}\left(\frac{I_0}{2n_0 m_e c^2 v_s}\right)^{1/2} \tag{1.83}$$

where I_0 is the incident intensity (in $\mathrm{watt\ cm}^{-2}$), ω_0 is the frequency of incident light, n_0 is the background number density (in cm^{-3}) and v_s is the phase velocity (in $\mathrm{cm\ s}^{-1}$) of the ion acoustic wave [29].

1.5.5 Stimulated Raman Scattering

E → E + L: Like SBS, a backwards-travelling EMW is produced, but this time accompanied by a forward moving Langmuir wave, rather than an ion-acoustic wave. SRS can also be treated as a one-dimentional instability although, like SBS, it can take place in two and three dimentions. The Langmuir daughter wave may trap and accelerate electrons. These supra-thermal electrons are the most important facet of SRS, since they may preheat the fusion fuel prior to compression. The minimum drive frequency for SRS is given by $\omega_1 = 2\omega_{pe}$ corresponding to a maximum density of $n_e = \frac{1}{4}n_c$. Thus, in a typical ramped density profile, SRS occurs away from the critical surface. The growth rate of SRS (in s^{-1}), for an incident intensity much greater than the threshold intensity is:

$$\Gamma_{srs} = \frac{\omega_{pe}^2}{2\omega_0}\left(\frac{I_0}{2n_0 m_e c^2 v_l}\right)^{1/2} \tag{1.84}$$

where I_0 is the incident intensity (in $\mathrm{watt\ cm}^{-2}$), ω_0 is the frequency of incident light, n_0 is the background number density (in cm^{-3}) and v_l is the phase velocity (in $\mathrm{cm\ s}^{-1}$) of the Langmuir wave [29].

1.5.6 Two Plasmon and Two Ion Wave Decay

E → L + L: Two Plasmon Decay: the driving laser excites two Langmuir waves moving in opposite directions.

E → S + S: Two ion wave decay (TIWD): the driving field excites two ion acoustic waves which move in opposite directions.

Like the parametric instability, wave vectors of the daughter waves cannot be anti-parrallel. In order for the transverse electric field of the parent to couple to the longditudinal electric field of the daughters, wave vectors must be aligned as shown in Fig.1.16 This necessitates at least a two-dimensional treatment.

1.5.7 The Langmuir Decay Instability and the Langmuir Cascade

Unlike the parametric instabilities described above, Langmuir decay is driven, not by an EMW pump, but by a Langmuir wave which decays into another Langmuir wave and an ion-acoustic wave. The resulting longer wavelength Langmuir wave can then itself undergo Langmuir decay, producing a third Langmuir wave and a second ion-acoustic wave. This process gives rise to the Langmuir cascade in which energy is transferred to longer and longer wavelengths (see Fig.1.17). However, this decay process cannot continue indefinitely. The Langmuir cascade [31] proceeds for all k above a critical value k_c, determined by the point where the group velocities of the parent Langmuir wave (L) is equal to that of the IAW:

$$\frac{\partial \omega_L}{\partial k} = \frac{\partial \omega_{IAW}}{\partial k} \Rightarrow k_c = \frac{1}{3\lambda_D}\sqrt{\frac{m_e}{m_i}}. \tag{1.85}$$

In hydrodynamic turbulence energy is transferred to progressively smaller and smaller scales before being dissipated via viscosity [32]. The Langmuir cascade transfers energy to progressively longer wavelengths, from which the energy must then be dissipated. The generally accepted mechanism for dissipation from the Langmuir condensate is via the Modulational Instability. This instability forms density holes, cavitons, by the action of the ponderomotive force. These trap energy in the form of long wavelength Langmuir waves, until eventually the cavitons burn-out, releasing energy in the form of hot electrons.

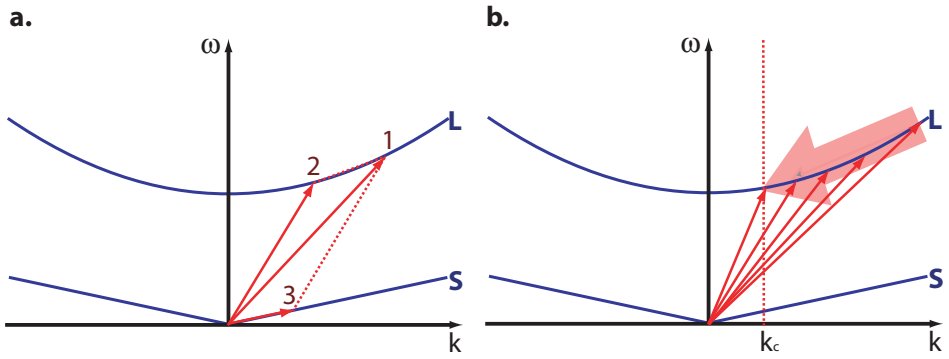

Figure 1.17: Langmuir Decay Instability. **a.** Driving Langmuir wave, '1', decays into a longer wavelength Langmuir wave, '2', and an ion-acoustic wave, '3'. **b.** This process can occur repeatedly to form a *Langmuir Cascade*, transferring energy to longer wavelengths until reaching $k = k_c = \frac{1}{3\lambda_D}\sqrt{\frac{m_e}{m_i}}$.

1.5.8 The Modulational Instability

The simplest model for cavition formation is given in Ref.[16]. Starting with Eq.(1.19) define the turbulence parameter $\bar{W} = \frac{\epsilon_0|\bar{\mathbf{E}}^2|}{4n_0 k_B T_e}$ and note that $m_i c_S^2 \simeq k_b T_e$ to give

$$\frac{\partial^2}{\partial t^2}\frac{\delta n}{n_0} = c_S^2 \nabla^2 \left(\frac{\delta n}{n_0} + \bar{W}\right). \tag{1.86}$$

Note that $\frac{\partial^2}{\partial t^2}\frac{\delta n}{n_0} = 0$ when $\frac{\delta n}{n_0} = -\bar{W}$. This is the quasistatic solution of the second Zakharov equation, Eq.(1.19). It represents a state in which regions of increased electric field amplitude correspond to a depletion in ion density. Seeking solutions to Eq.(1.16), where $\tilde{\mathbf{E}}$ varies as $\exp(iv\mathbf{k}\cdot\mathbf{x} - i\omega t)$, and retaining the nonlinear coupling between slow ion-density variations and the fast-timescale electric field gives

$$\omega^2 = \omega_{pe}^2 \left(1 + 3k^2\lambda_D^2 + \frac{\delta n}{n_0}\right). \tag{1.87}$$

Since $\frac{\delta n}{n_0} = -\bar{W}$, it follows that $\frac{\delta n}{n_0} < 0$. So in the case where $|\frac{\delta n}{n_0}| > 3k^2\lambda_D^2$, from Eq.(1.87) it follows that $\omega < \omega_{pe}$. Now waves whose wavenumbers satisfy $|\frac{\delta n}{n_0}| > 3k^2\lambda_D^2$ will be unable to move through the bulk plasma, and will become trapped within the density depletion. This process of trapping electrostatic waves is inherently

unstable. Once it has begun it will continue to grow. If the condition is satisfied in some region and the magnitude of the density depletion is increased slightly then it follows that some wavelengths, previously free, will become trapped. These trapped waves increase the local value of $\bar{W}$ resulting in the expulsion of more ions, by the action of the ponderomotive force. This, in turn results in the trapping of more electrostatic waves, leading to an instability charaterised by ion-density depletion and a growth in the amplitude of the slowly evolving envelope of the electric field.

1.5.9 LPI in the context of ICF

In radiation driven ICF, the laser encounters two significant LPI regimes. Firstly as the beam traverses the low-Z plasma, filling the Hohlraum, and secondly, as the beam is absorbed by the high-Z plasma formed at the Hohlraum wall. Much of the physics is common to direct drive, where the beams must pass through the expanding corona of fuel and deliver their energy to the core.

In the interaction with the low-Z (typically a H or He H) plasma, the incident light can decay into a back scattered beam and a transverse plasma wave (ion acoustic for SBS or Langmuir for SRS). Beating between incident and back scattered beams drives the plasma wave to higher and higher amplitude, making it increasingly effective at scattering the laser and creating the feedback loop at the heart of instabilities such as SBS and SRS.

SBS can scatter a significant proportion of incident light, observed levels range from 12%, in early NIF experiments [33], to upwards of 25% in Nova experiments [34]. Losses of this magnitude impact the efficiency of the system. Furthermore, the scattered light can directly irradiate the fuel pellet of an indirect drive target, destroying the drive symmetry. Fast moving plasma blown out of the LEHs is susceptible to SBS with different frequency matching conditions to the bulk Hohlraum plasma, due to the Doppler shift. The interplay of instabilities in this region where the beams cross can even lead to energy transfer between laser beams [35], also affecting the drive symmetry. Some experimental results suggest that SBS may be controlled, or at least capped, by a judicious choice of dopants [36] although the exact mechanisms for these effects are

not well understood.

The levels of reflectivity observed from SRS are considerably lower than SBS, typically only a few percent. It may thus appear that SRS cannot represent a significant cause for concern. However, aside from the generation of a scattered beam, it is the second product of SRS which is of most interest. In driving a high amplitude Langmuir wave, SRS can produce suprathermal electrons which can preheat the core, making its compression towards ignition much harder.

Historically, plasma inhomogeneity has helped to limit the potential of such parametric instabilities and their effects. However, ignition scale plasmas are expected to have long density and velocity scale lengths [34, 33], 2mm and 6mm respectively. Under such conditions, the limiting factors will be the damping of daughter waves, pump depletion and, particularly at high intensity, non-linear effects such as wave-breaking and particle trapping.

The non-linear saturation of SRS can proceed via electron trapping in the Langmuir daughter wave (and subsequent de-tuning) or via the Langmuir decay of the daughter wave, initiating a Langmuir cascade [13, 37].

Understanding the physics of LPI, along the beam path, in the LEHs, at the Hohlraum wall or in the target corona, is vital for efficient target design and the operation of a successful inertial fusion reactor. The growth, evolution and in particular, the saturation of instabilities such as SRS, SBS, LDI, and filamentation, require thorough theoretical and numerical, as well as experimental, investigation.

Vlasov codes offer high velocity space resolution in high energy regions of particle phase space, and do not require analytical pre-processing of the fundamental equations. In particular, this treatment can resolve kinetic phenomena in LPI such as particle trapping, for example in BGK modes.

1.6 Outline

The electrostatic Vlasov code, introduced in Ref.[38] is described in chapter 2 and used to investigate kinetic effects of relevance to ICF - the breaking of large amplitude

Langmuir waves and creation of high energy electron phase space jets. An analytical model, describing the necessary conditions for the development of these jets, is developed and tested.

Chapter 3 considers the kinetic modeling of particle acceleration in astrophysical, rather than ICF, plasmas. Electrons may be trapped and accelerated by electrostatic waves driven by the Buneman instability, in a system dominated by two counter-propagating ion beams. These mechanisms are shown to be sufficient for promoting some of the electron population to energies comparable to the Fermi injection energy.

The electrostatic Vlasov model is extended to a fully relativistic model with transverse EM fields. This allows the full kinetic simulation of LPI. Chapter 4 describes in full the development and testing of this Electromagnetic (EM) Vlasov Maxwell code.

In chapter 5 the EM Vlasov Maxwell code is used to consider scattering of incident laser light from non thermal particle distributions where the standard fluid-like descriptions, based on idealised dispersion relations, prove to be inadequate.

Chapter 2

Electrostatic Wave-Caviton Interaction

This work is an expansion of published work [N. J. Sircombe, T. D. Arber and R. O. Dendy, *Accelerated electron populations formed by Langmuir wave-caviton interactions*, Phys. Plasmas, **12**, 012303 (2005)].

2.1 Outline

The potential of a plasma as a medium for accelerating particles has been known for some time [11]. Plasmas can sustain high electric field gradients, in theory capable of accelerating electrons to GeV's over a distance of only a metre - making tabletop particle accelerators a realistic possibility. Plasma accelerators come in four basic types, laser wakefield acceleration (LWFA), self-modulated LWFA, plasma beat wave accelerators and plasma wakefield accelerators. These basic concepts are detailed in Ref.[39]. Recent laser-plasma experiments have been successful in producing high-energy mono-energetic electron beams [40, 41, 42].

This chapter describes a novel mechanism for the non-resonant acceleration of electrons within a plasma. Coupling of strong Langmuir turbulence to finite amplitude, coherent Langmuir waves allows the potential energy of the Langmuir waves to be imparted to electrons as the wave breaks. This results in the acceleration of

a small population of electrons from the background population at the point where wave-breaking occurs. Acceleration occurs spontaneously without requiring an intense laser pulse or particle injection, which are key features of electron acceleration schemes [11, 43, 39, 44, 45] that rely on wave-particle resonance, such as LWFA, self-modulated LWFA, plasma beat wave accelerators and plasma wakefield accelerators. The electrons accelerated form a collimated phase space jet in the electron distribution function f_e. Such populations of energetic electrons are of some concern in inertial confinement fusion (ICF) experiments, because they may contribute directly to capsule pre-heat or form the seed populations for further acceleration. For example, the hot electrons generated by this mechanism could undergo wakefield acceleration [46, 47, 48] in the presence of a laser field, creating even more energetic particles capable of pre-heating the ICF capsule [2, 49].

By considering the relativistic one dimensional Vlasov-Poisson system and exposing this system to a large amplitude electrostatic standing wave (in a similar manner to Ref.[50]), it is possible to drive the formation of cavitons. As described in section 1.5.8, these cavitons are, in essence, local regions of ion density depletion accompanied by a local concentration of electric field amplitude. Their formation is driven by the ponderomotive force and they are seeded by small fluctuations in the electron density. In simulations these initial fluctuations are provided by the electrostatic driving field. However, once the process of cavitation has begun, the external field can be removed without significantly affecting further caviton development. At a particular point in the caviton development, fine jet-like structures form in the electron phase space. Necessary conditions for jet formation, depending on the characteristics of the caviton, can be derived. These phase space jets represent a portion of the electron population accelerated from a small region near the edge of a caviton. The process by which these the jets emerge, together with their characteristics, suggests that they are the result of breaking Langmuir waves. This hypothesis is supported by further simulations, and by a simple model for the process based on a fluid treatment including Landau damping. This theory is an extension of the work of Akhiezer and Polovin [51] on breaking Langmuir waves in a uniform medium. The energy distribution and the maximum energy within a jet can

be calculated from conservation of energy, provided one assumes that all of the potential energy of the wave is imparted to the electrons at the breaking wavefront.

2.2 The Relativistic Vlasov-Poisson System

2.2.1 Governing Equations

The model used is a one dimensional relativistic Vlasov-Poisson system of electrons and protons with a mass ratio $m_i/m_e = M_r$, and no magnetic field. The Vlasov equation given in Eq.(1.45) is a three dimensional non-relativistic treatment. For the case of a one-dimentional electrostatic system, this simplifies to

$$\frac{\partial f_e}{\partial t} + v\frac{df_e}{dx} - \frac{e}{m_e}E_x\frac{df_e}{dv} = 0 \tag{2.1}$$

for the electrons and

$$\frac{\partial f_e}{\partial t} + v\frac{\partial f_e}{\partial x} - \frac{e}{m_e}E_x\frac{\partial f_e}{\partial v} = 0 \tag{2.2}$$

for the ions. With E_x given by Poisson's equation

$$\frac{\partial E}{\partial x} = -\frac{e}{\epsilon_0}\left(\int f_e dv - \int f_i dv\right). \tag{2.3}$$

The system can be modified to account for relativistic dynamics by replacing the velocities, v, with momenta, p_x. Where $p_x = \gamma m_e v$ and $\gamma = (1 + {p_x}^2/m_e^2c^2)^{1/2}$ is the Lorentz factor. This fully nonlinear, relativistic, self consistent system is governed by the Vlasov equations for the electrons and ions

$$\frac{\partial f_e}{\partial t} + \frac{p}{m_e\gamma}\frac{\partial f_e}{\partial x} - eE\frac{\partial f_e}{\partial p} = 0, \tag{2.4}$$

$$\frac{\partial f_i}{\partial t} + \frac{p}{m_i\gamma}\frac{\partial f_i}{\partial x} + eE\frac{\partial f_i}{\partial p} = 0, \tag{2.5}$$

and Poisson's equation for the electric field, as given in Eq.(2.3).

2.2.2 Normalisation

Taking $\tilde{z}$ to represent the normalised form of the variable z, the following dimensionless normalisation, appropriate to a relativistic system, is adopted: $x = (c/\omega_{pe})\tilde{x}$, $t =$

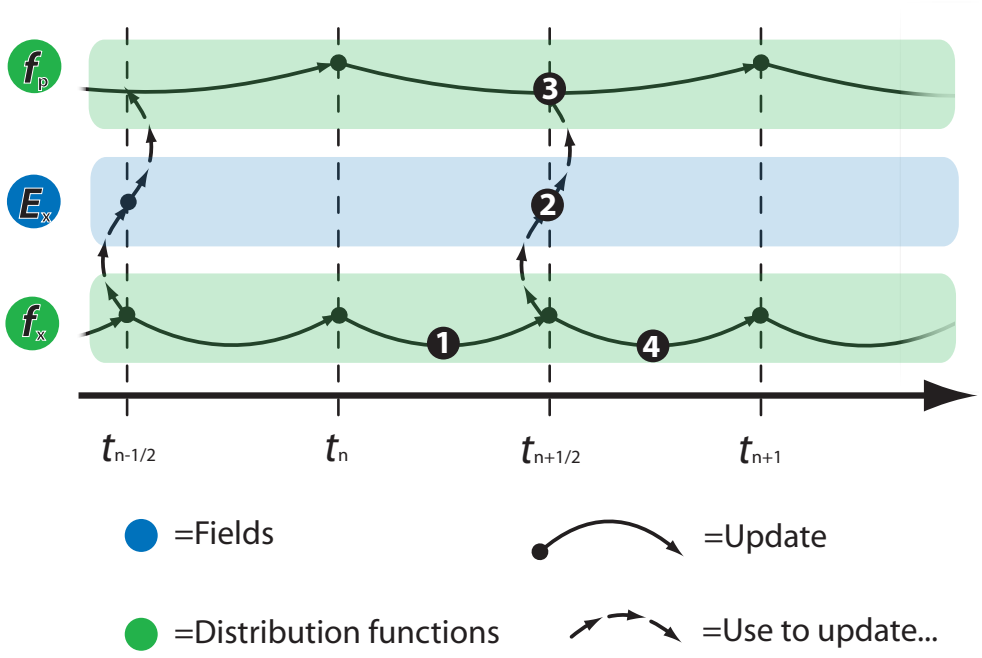

Figure 2.1: The time-stepping algorithm for the electrostatic Vlasov-Poisson solver. **1.** Advect distribution functions in x forward one half timestep. **2.** Update E_x using the time centred density profile given after step 1. **3.** Advect ditribution functions in v forward one whole timestep using the time centred electric field calculated in step 2. **4.** Advect distribution functions forward the remaining half timestep in x.

$(1/\omega_{pe})\tilde{t}$, $v = c\tilde{v}$, $E = (\omega_{pe}cm_e/e)\tilde{E}$, $p = m_e c\tilde{p}$. It follows that frequencies are normalised to the plasma frequency, $\omega = \omega_{pe}\tilde{\omega}$, wavenumbers to the ratio of the plasma frequency to the speed of light, $k = (\omega_{pe}/c)\tilde{k}$, and temperatures are normalised such that $T_{e,i} = (\kappa/m_{e,i}c^2)\tilde{T}_{e,i}$. All simulations are carried out using a mass ratio $M_r = m_i/m_e = 100$. This value is sufficiently large to allow the development of phenomena on two disparate time-scales (since electron and ion plasma frequencies are an order of magnitude apart), without the increased runtime of the real mass ratio.

2.2.3 Numerical Approach

The Vlasov-Poisson system is solved using the code detailed in Ref.[38]. This is a non-symplectic split Eulerian scheme in which the distribution functions (f_e, f_i) are calculated on a fixed Eulerian grid, and the solver is split into separate spatial and velocity space updates [52]. These updates are one dimensional, constant velocity advections of the form $\partial_t f + v\partial_x f = 0$ in space and $\partial_t f + E_x \partial_v f = 0$ in velocity space. These are carried out using the piecewise parabolic method [53]. The scheme is third order in space where the distribution function is smooth, first order at discontinuities and second order in time. The original code has been extended to solve the fully relativistic Vlasov-Poisson system, described above.

Equation (2.3), Poisson's equation, is solved in by taking the discrete Fourier transform (DFT) of the source term $\frac{e}{\epsilon_0}(n_i - n_e)$, on the numerical grid

$$ik\mathrm{F.T.}(E_x) = \frac{e}{\epsilon_0}\mathrm{F.T.}(n_i - n_e) \;\Rightarrow\; \mathrm{F.T.}(E_x) = \frac{e}{ik\epsilon_0}\mathrm{F.T.}(n_i - n_e) \qquad (2.6)$$

followed by the inverse DFT to give $E_x(x)$.
The timestepping algorithm, shown schematically in Fig.2.1, is as follows.

- Evolve $\partial_t f + v\partial_x f = 0$ for time $\frac{\Delta t}{2}$.
- Solve Poisson's equation for E_x.
- Evolve $\partial_t f + E_x \partial_v f = 0$ for time Δt.
- Evolve $\partial_t f + v\partial_x f = 0$ for time $\frac{\Delta t}{2}$.

A large amplitude external driving field $\tilde{E}_d = \tilde{E}_0 \sin(\tilde{k}\tilde{x}) \sin(\tilde{\omega}_0 \tilde{t})$ is added to the self consistent electric field found from Poisson's equation. The parameters of the driving field are chosen to ensure that the system is driven at resonance ($\omega_0 = \omega_{pe}$, or $\tilde{\omega}_0 = 1$ in normalised units), and that the intensity of the perturbations corresponds to the high quiver velocity regime $v_q^2/v_{Te}^2 > 1$, where $v_q = eE_0/m_e\omega_0$. Hence $E_0 > m_e\omega_0 v_{Te}/e$, or in normalised units:

$$\tilde{E}_0 > \tilde{v}_{Te}. \qquad (2.7)$$

This driving field, similar to the perturbation used in earlier work on the modulational instability [50], is necessary to drive the formation of cavitons and is only needed during the early stages of the simulation. In these simulations it is applied from $\tilde{t} = 0$ to $\tilde{t} = 10$, which is sufficient to seed the formation of cavitons.

Extending the presence of the driving field after $\tilde{t} = 10$ does not significantly effect the evolution of cavitions or the amplitude of Langmuir waves in the system. Hence the energy of accelerated electrons remains below 5MeV. However, Langmuir waves formed as a result of the the continued presence of $\tilde{E}_d$ result in more numerous and frequent phase space jets.

2.3 Results

2.3.1 Initial Conditions

The system is initialised with a Maxwellian distribution of both electrons and ions at equal temperatures with an electron thermal velocity

$$v_{Te}^2 = c^2/10^3 \tag{2.8}$$

and an ion thermal velocity

$$v_{Ti}^2 = c^2/10^3 M_r, \tag{2.9}$$

equivalent to a temperature ≈ 0.5keV. In normalised units this gives $\tilde{v}_{Te} = 10^{-3/2}$, hence from Eq.(2.7), $\tilde{E}_0 > 10^{-3/2}$. The simulation box is of length $\tilde{L}_x = 20\pi$ in normalised units, with periodic boundary conditions in space. In summary, the dimensionless initial conditions are $\tilde{T}_e = 0.001$, $\tilde{T}_i = 0.001$, $\tilde{L_x} = 20\pi$, $\tilde{E_0} = 0.5$, $\tilde{\omega_0} = 1$, $\tilde{k} = 2\pi/\tilde{L_x}$, and the initial maximum of f_e, $f_e^{max} = 9.2925$.

2.3.2 Caviton Formation and Jet Creation

The development of cavitons can be seen in both the isometric renderings of the electron distribution function (Figs.2.2 and 2.3) and plots of the density and electric field amplitude (Fig.2.4). Cavitons form in response to the ponderomotive force exerted on the electrons by the driving field E_d. Hence they are centred around regions where the

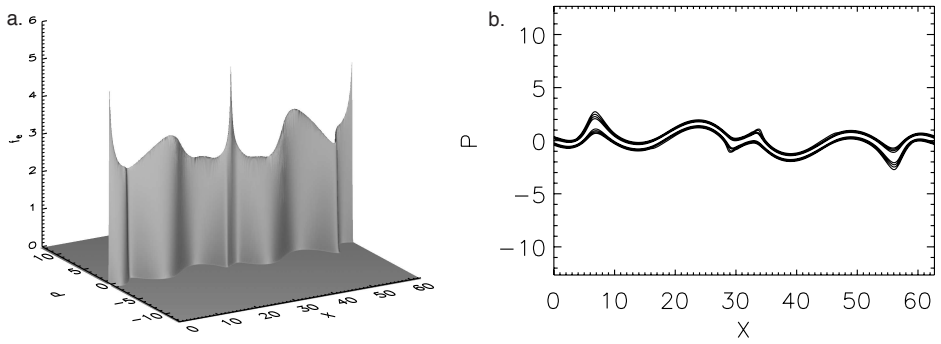

Figure 2.2: **a.** Isometric view of the electron distribution function f_e and **b.** contour plot of $\log(f_e > 10^{-6})$ at time $\tilde{t} = 20$. Here the relativistic Vlasov-Poisson system is driven from $\tilde{t} = 0$ to 10 at $\omega = \omega_{pe}$. The evacuation of electrons from localised regions of the simulation domain is seen in the electron distribution function; this is the early stage of cavitation. Caviton formation is due to the modulational instability initially driven by the external field E_d.

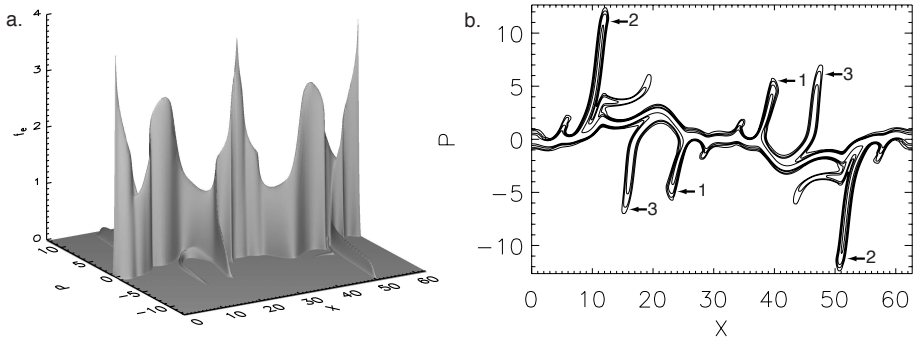

Figure 2.3: **a.** Isometric view of the electron distribution function f_e and, **b.** contour plot of $\log(f_e > 10^{-6})$ at time $\tilde{t} = 40$. Here the relativistic Vlasov-Poisson system was driven from $\tilde{t} = 0$ to 10 at $\omega = \omega_{pe}$. Fine jet-like structures in electron phase space are visible: jets marked '**1**' have recently formed on the inside edges of the two cavitons, whereas the jets marked '**2**' have formed in the same area at an earlier time and have since been advected through the system. The jets marked '**3**' are at an intermediate stage, having formed on the outside edges of the cavitons. These jets are the result of Langmuir wave-breaking at the edges of the evolving density holes.

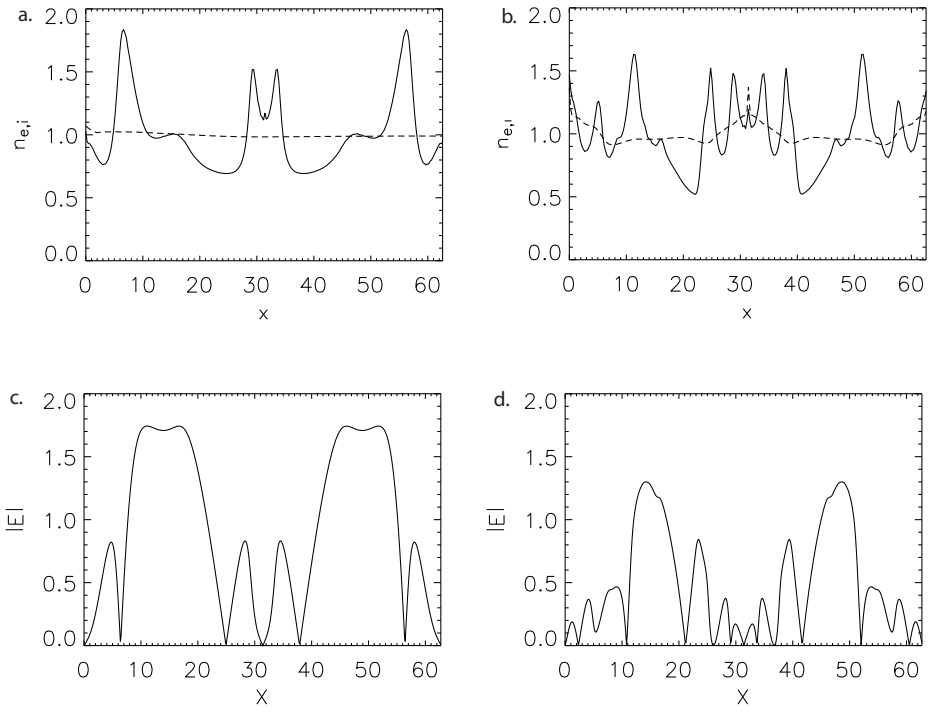

Figure 2.4: Plots of the electron (solid line) and ion (dashed line) density at **a.**$\tilde{t} = 20$ and, **b.** $\tilde{t} = 40$, together with the electric field amplitude at $\tilde{t} = 20$ (**c.**) and $\tilde{t} = 40$ (**d.**) for a relativistic Vlasov-Poisson system that was driven from $\tilde{t} = 0$ to 10 at $\omega = \omega_{pe}$. The formation of ion density holes can be clearly seen, together with localised growth in the electric field amplitude characteristic of caviton formation. Caviton formation is due to the modulational instability driven initially by the external field E_d.

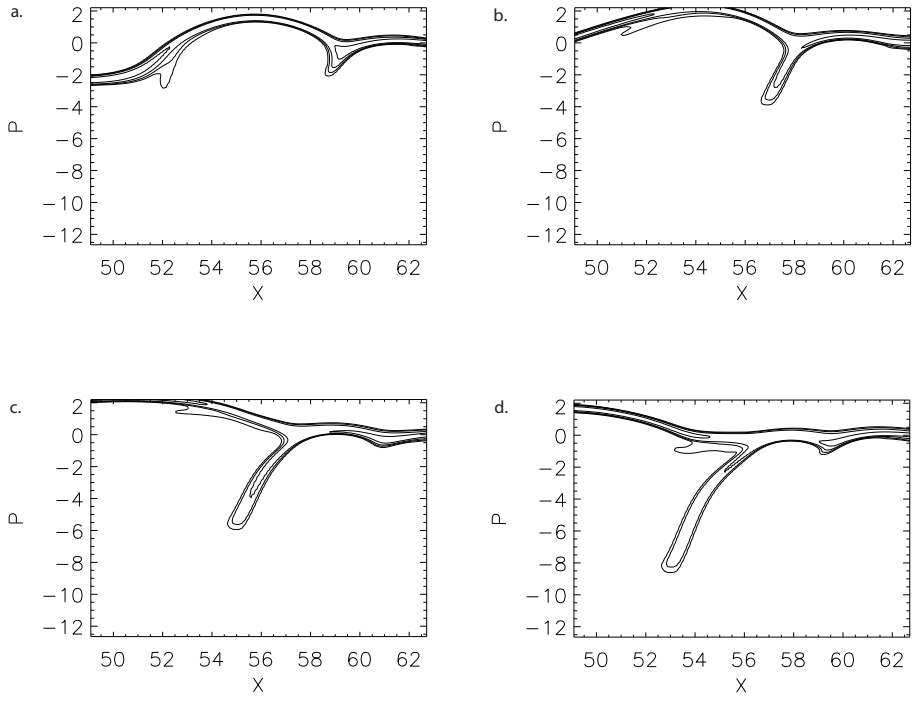

Figure 2.5: Contour plots of $\log(f_e > 10^{-6})$ in the region $50 \lesssim \tilde{x} \lesssim 60$ at times **a.** $\tilde{t} = 32$, **b.** 34, **c.** 36 and **d.** 38. These plots show a phase space jet developing at the outside edge of the caviton (see Fig.2.4) at $\tilde{x} \approx 60$. Electrons are accelerated from a compact region of the background distribution to form the jet, which extends and advects across the caviton.

amplitude of the driving field is strongest, leading to symmetry in $n_{e,i}$ and $|E|$ about the centre of the system $\tilde{x} = 10\pi$. By $\tilde{t} = 20$ two prominent holes, driven by the ponderomotive force, have formed in the electron density centred at $\tilde{x} \approx 25$ and 37. As the system continues to evolve, the ions are slowly evacuated to form two broad density holes. These holes in both ion and electron densities are accompanied by a local increase in the electric field amplitude, characteristic of caviton formation, see Fig.2.4.

At later times, populations of accelerated electrons are clearly visible in the contour plots of the electron distribution function. These are the electron phase space jets. At $\tilde{t} = 20$, ten plasma periods after the driving field has been removed, there is no evidence of jet formation, see Fig.2.2. However, between $\tilde{t} = 20$ and $\tilde{t} = 40$ a series of phase space jets form on both edges of the deepening cavitons. Studying the evolution of the electron distribution function during this period allows one to identify phase space jets at different points in their evolution. In Fig.2.3 jets are highlighted at three separate stages of evolution. There are two jets (**1**) forming on the inside edges of the caviton as well as two old jets (**2**) which have been advected across the system, effectively crossing the cavitons on whose edges they formed. Finally, there are two intermediate jets (**3**), on the outer edges of the cavitons. The most energetic electrons within these jets have energies $\approx$ 5MeV. The appearance of these jets does not affect the development of the cavitons, which continue to deepen after the appearance of the phase space jets. In addition, the simulation is seeded with randomly distributed tracer particles. These do not contribute to the numerical solution of the Vlasov Poisson system and are simply moved in response to the total electric field (self consistent electric field plus driving field). Following the motion of these particles indicates that the electrons which form the jets are not accelerated from within the caviton - this effectively rules out caviton burn-out as an explanation for the origin of the phase space jets.

2.3.3 Jet Emergence

The process of jet emergence is best explained by observing the evolution of the electron distribution function, focusing on a region where a jet develops, during its early stages. Figure 2.5 shows a reduced section of the electron phase space, the region $50 \lesssim \tilde{x} \lesssim 60$

where the rightmost jet, labelled '2' in Fig.2.3, first appears. This region encompasses the right hand side of one of the deepening cavitons seen in Fig.2.4. The jet forms at the outer, right hand edge of this caviton at $\tilde{x} \approx 60$. The sequence of contour plots in Fig.2.5 shows that the jet then extends out from the main electron distribution, at $|\tilde{p}| \approx 2$, to momenta of $|\tilde{p}| \approx 8$ in approximately one plasma period.

2.4 Physics of Electron Jets

2.4.1 Wave Breaking

The key observed features of the phase space jets are:

1. Jets do not appear at early times in the simulation, they first require some degree of caviton evolution.

2. Jets are not directly related to the external driver, they appear after the removal of the external driving field.

3. Jets are not associated with caviton burn-out processes, since cavitons persist long after the appearance of jets.

4. Jets originate at the caviton edge. Electrons are accelerated from the main distribution to form the phase space jet which is then advected through the system. Their constituent electrons pass over the caviton on whose edge they formed, escaping the influence of the caviton completely. The direction of this advection indicates that phase space jets are the result of processes originating outside the caviton.

5. Electrons are accelerated up to energies of 5MeV from an initially Maxwellian population with temperature $\approx$ 0.5keV.

From extensive numerical simulations of the system, it is clear that the breaking of Langmuir waves on the density gradients at the edges of the cavitons is responsible for the creation of the phase space jets. Figure 2.6 provides a schematic illustration of the physical process, which is explored in the rest of this section. The Langmuir wave

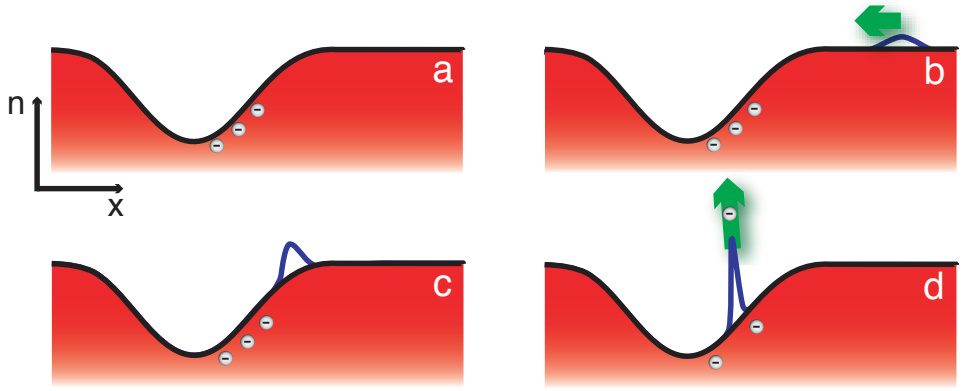

Figure 2.6: Schematic representation of electron acceleration by Langmuir wave-breaking. **a.** Density hole with a few sample electrons highlighted. **b.** The crest of a Langmuir wave moves towards the density hole. **c.** As the wavefront moves down the gradient at the edge of the density hole, its phase velocity falls and the wavefront steepens. **d.** For a density hole of sufficient depth and steepness, the incoming wave breaks, forming a strong localised electric field which accelerates electrons from the inside edge of the caviton to create jets in electron phase space.

first approaches the density hole. As it moves into the region of lower density, the phase speed at the front of the wave falls. If this proceeds rapidly enough to overcome the effect of Landau damping (which acts to damp the incoming wave energy, and thereby prevent it from breaking), then the wave will break. This creates a strong electric field localised at the wave crest, which accelerates electrons in the vicinity away from the background population to form phase space jets. The following three sections outline an analytical model of the competing processes of wave-breaking and Landau damping, together with a derivation of the electron energy distribution within the jet.

2.4.2 Wave Breaking Amplitude

The maximum amplitude E_{br} of a Langmuir wave which can be sustained in a plasma before it breaks is given by the Akhiezer and Polovin constraint [51]. For a non-relativistic phase velocity v_p, this is given by

$$eE_{br}/m_e\omega_{pe}v_p = 1 \tag{2.10}$$

where the breaking amplitude E_{br} is the maximum electric field amplitude which can be sustained by a Langmuir wave before it breaks. In normalised units Eq.(2.10) is equivalent to $\tilde{E}_{br} = \tilde{v}_p$; the breaking amplitude depends on the phase velocity of the wave, which is determined by the Langmuir dispersion relation

$$\omega^2 = \omega_{pe}^2 + 3{v_{Te}}^2 k^2 \tag{2.11}$$

Consider a Langmuir wave moving through a region of decreasing density

$$\tilde{n} = \tilde{n}(\tilde{x}) \tag{2.12}$$

where n falls from an initial value n_0, corresponding to a plasma frequency of $\omega_{pe}^0 = \left(n_0 e^2/m_e\epsilon_0\right)^{1/2}$. As a first approximation, we may assume that the amplitude and frequency of the Langmuir wave remain fixed at E_L ($\tilde{E}_L$ in normalised units) and $\omega \approx \omega_{pe}^0$ ($\tilde{\omega} \approx 1$ in normalised units) respectively. Taking the dispersion relation Eq.(2.11) in normalised units

$$\tilde{\omega}^2 = \tilde{n}(\tilde{x}) + 3\tilde{T}_e\tilde{k}^2 \tag{2.13}$$

with $\tilde{\omega} \approx 1$ gives an estimate of the local wavenumber of the Langmuir wave as a function of $\tilde{n}(x)$:

$$\tilde{k} = \left(\left(1 - \tilde{n}(x)\right)/3\tilde{T}_e\right)^{1/2} \tag{2.14}$$

This corresponds to a phase velocity $\tilde{v}_p = \tilde{\omega}/\tilde{k} \approx 1/\tilde{k}$ given by

$$\tilde{v}_p = \left(3\tilde{T}_e/(1 - \tilde{n}(\tilde{x}))\right)^{1/2} = \tilde{E}_{br} \tag{2.15}$$

the breaking amplitude, by Eq.(2.10). For the case of a linear density ramp $\tilde{n}(\tilde{x}) = 1 - \eta\tilde{x}$ where $0 < \tilde{x} < 1/\eta$, Eqs.(2.14) and (2.15) imply

$$\tilde{k} = \left(\eta\tilde{x}/3{\tilde{T}_e}^2\right)^{1/2} \tag{2.16}$$

and

$$\tilde{v}_p = \left(3\tilde{T}_e/\eta\tilde{x}\right)^{1/2} = \tilde{E}_{br}. \tag{2.17}$$

As the wavefront moves down the density ramp, the phase velocity falls, reducing the maximum wave amplitude which can be sustained. If the breaking threshold falls sufficiently, it will be satisfied by the incoming wave, which will then break. The wave

breaking condition

$$\tilde{E}_{br} \leq \tilde{E}_L \tag{2.18}$$

together with Eq.(2.16) gives

$$\left(3\tilde{T}_e/\eta\tilde{x}\right)^{1/2} \leq \tilde{E}_L \tag{2.19}$$

Thus far, this treatment has not taken into account the effect of Landau damping of the Langmuir wave as it moves down the density ramp, which could reduce the field amplitude at a rate which ensures the breaking condition is never achieved. If the initial amplitude of the Langmuir wave is $\tilde{E}_{L0}$, then the damped amplitude at time $\tilde{t}$ is given by

$$\tilde{E}_L = \tilde{E}_{L0} e^{-\Gamma(\tilde{t})} \tag{2.20}$$

Here the local damping decrement γ_L determines $\Gamma(t)$

$$\Gamma\left(\tilde{t}\right) = \int_0^{\tilde{t}} \gamma_L dt \tag{2.21}$$

$$\gamma_L = \left(\frac{\pi}{8}\right)^{\frac{1}{2}} \frac{\omega_{pe}}{k^3\lambda_D^3} \exp\left(-\frac{3}{2} - \frac{1}{2k^2\lambda_D^2}\right) \tag{2.22}$$

Using the estimate for $\tilde{k}$ given in Eq.(2.16) and solving the integral in Eq.(2.21) for $\tilde{x}$ following the wave, given that

$$\frac{\partial\tilde{x}}{\partial\tilde{t}} = \tilde{v}_g = \frac{\partial\tilde{\omega}}{\partial\tilde{k}} = \left(3\tilde{T}_e\eta\tilde{x}\right)^{1/2} \tag{2.23}$$

yields

$$\tilde{E}_L = \tilde{E}_{L0} \exp\left(\frac{1}{\eta\sqrt{\tilde{T}_e}}\left(\frac{\pi}{2}\right)^{\frac{1}{2}} \exp\left(-\frac{3}{2} - \frac{3}{2\eta\tilde{x}}\right)\right) \tag{2.24}$$

Combining Eqs.(2.24) and (2.18) gives the condition for wave-breaking, and hence phase-space jet formation

$$\tilde{E}_{L0} \exp\left(\frac{1}{\eta\sqrt{\tilde{T}_e}}\left(\frac{\pi}{2}\right)^{\frac{1}{2}} \exp\left(-\frac{3}{2} - \frac{3}{2\eta\tilde{x}}\right)\right) - \left(\frac{3\tilde{T}_e}{\eta\tilde{x}}\right)^{1/2} \geq 0 \tag{2.25}$$

for a Langmuir wave with initial electric field amplitude $\tilde{E}_{L0}$ moving down a linear density ramp with gradient $-\eta$. In the steep gradient limit (i.e. $\eta \to \infty$), this is equivalent to Eq.(2.19). To summarise, as the Langmuir wave moves down the density ramp it

experiences Landau damping which reduces the wave amplitude from its initial value. The wave-breaking condition is then only satisfied if the decline in density reduces E_{br} to the value where it is equal to the damped Langmuir wave amplitude $\tilde{E}_L$ given by Eq.(2.24). Thus for a density ramp with edge gradient η and depth Δ, the wave will break, thereby accelerating electrons to form phase space jets, if Eq.(2.25) is satisfied for some $\tilde{x}$, $0 < \tilde{x} < \Delta/\eta$. This relation has been derived from a simple fluid treatment, modified to take into account the effect of Landau damping, which depends on caviton gradient η and depth Δ. It is supported by numerical simulations using fixed background density profiles containing cavitons with a chosen depth and edge gradient, which are presented below.

2.4.3 Fixed Ion Simulations

In order to test the model outlined above and demonstrate that the phase space jets are a direct result of breaking Langmuir waves, a further series of numerical simulations was conducted. These simulate the interaction of a Langmuir wave with a system having immobile ions whose initial density profile is fixed to provide density holes of a prescribed size and shape, as shown in Fig.2.7. A Langmuir wave was created by perturbing the initial electron distribution function to create a traveling wave of a given amplitude and wavelength. This initialisation relies on the linear dispersion relation, and so is only valid for small amplitudes. As the wave propagates across the simulation domain, it encounters the density hole created by the fixed ion background density profile. By varying the parameters of the density hole and the Langmuir wave, it is possible to change the nature of the phase space jets and confirm the functional dependence on caviton depth and gradient predicted by Eq.(2.25).

Figure 2.8 shows an area of (Δ, η) parameter space partitioned by Eq.(2.25), for a Langmuir wave of amplitude $\tilde{E}_{L0} = 0.12$ and wavelength $\tilde{\lambda}_L = 2\pi$. It also displays the results of simulations of the interaction of this Langmuir wave for a range of (η, Δ), classified by the presence or absence of phase space jets. The criterion used for jet formation is the presence of a second maximum, separated from the main distribution, in the region of the density ramp. This requires that f_e pass through a critical value

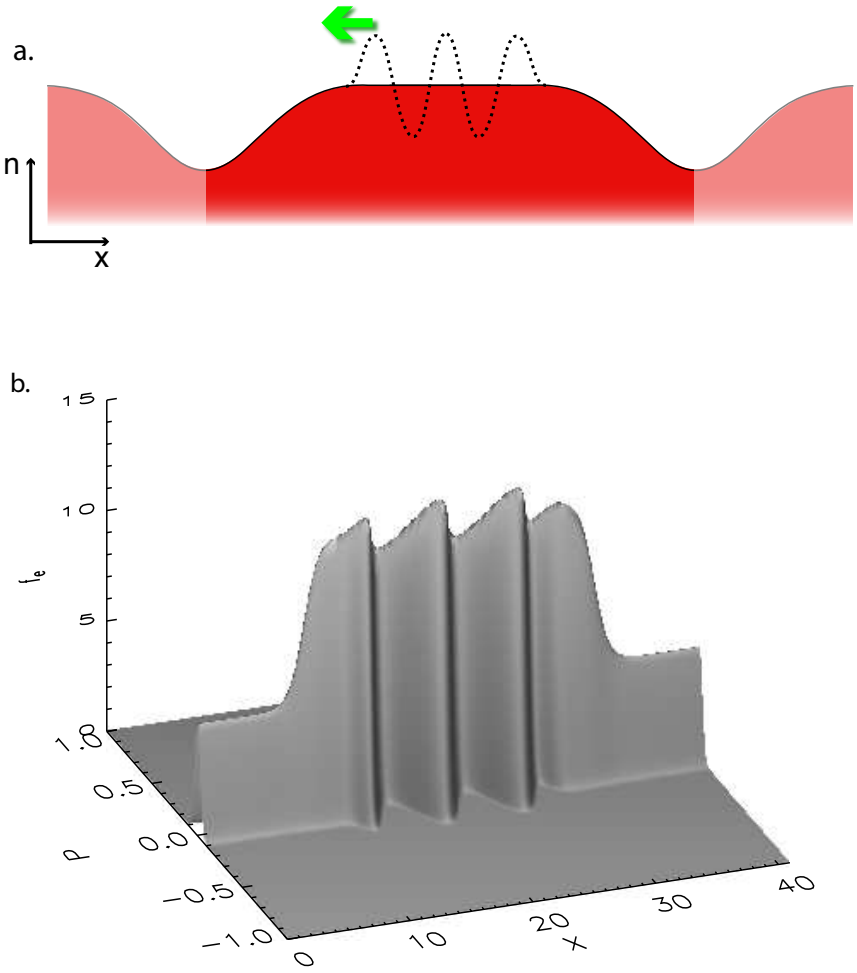

Figure 2.7: **a.** Schematic of the initial density profile used for fixed ion simulations. The simulation boundaries are periodic with density holes defined by a 'tanh' function. A traveling Langmuir wave of fixed wavelength and amplitude is added in the form of a sinusoidal electron density and velocity perturbation at the centre of the system. **b.** Isometric rendering of the electron distribution function from the fixed ion simulations at $\tilde{t} = 0$.

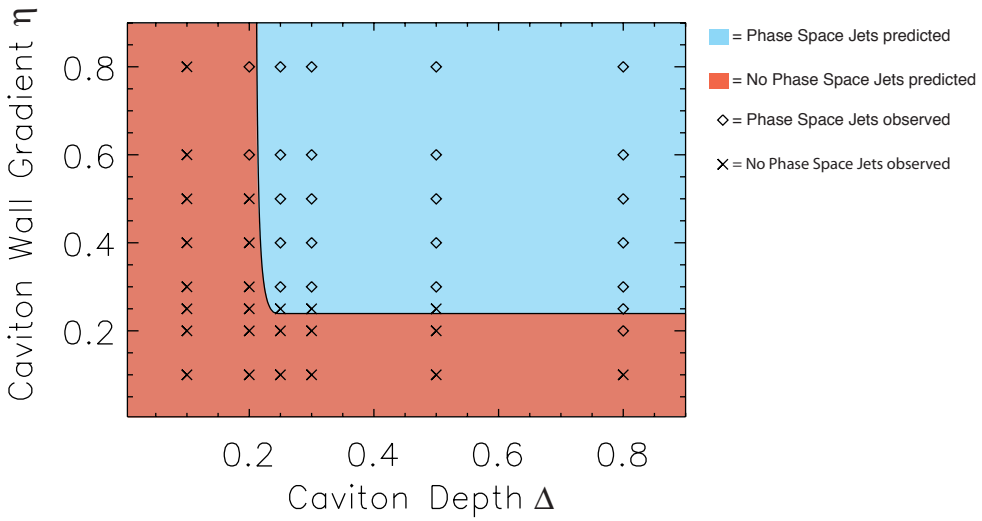

Figure 2.8: Jet formation and non-formation, plotted with respect to caviton parameter space (Δ, η), where Δ represents the caviton depth and η the edge gradient. The space is partitioned into regions of jet formation and non-formation by the breaking condition Eq.(2.25), and superimposed are the results from simulations using a fixed ion background to produce the desired caviton structure. The Langmuir wave considered here has amplitude $\tilde{E}_{L0} = 0.12$ and wavelength $\tilde{\lambda}_L = 2\pi$.

f_c four times for some point in the density ramp. The value f_c is chosen to be 1% of the initial maximum f_e^{max} of f_e. The simulation results support the analytical breaking condition Eq.(2.25) derived above. Figure 2.9 shows such a simulation at $\tilde{t} = 56$: a series of phase space jets have formed as a Langmuir wave ($\tilde{\lambda}_L = 2\pi$, $\delta n_e = 0.12$) encountered a density hole of depth $\Delta = 0.6$ and gradient $\eta = 0.5$.

2.4.4 Electron Energy Distribution within Jets

The maximum energy achieved by electrons in a phase space jet, and the distribution of electrons within the jet, can be calculated from the assumption that the total energy carried by the sum of jet electrons comes from the potential of the breaking Langmuir wave. Considering the fully relativistic case, conservation of energy is used to derive the electron energy distribution along the jet. Following the same approach as [54],

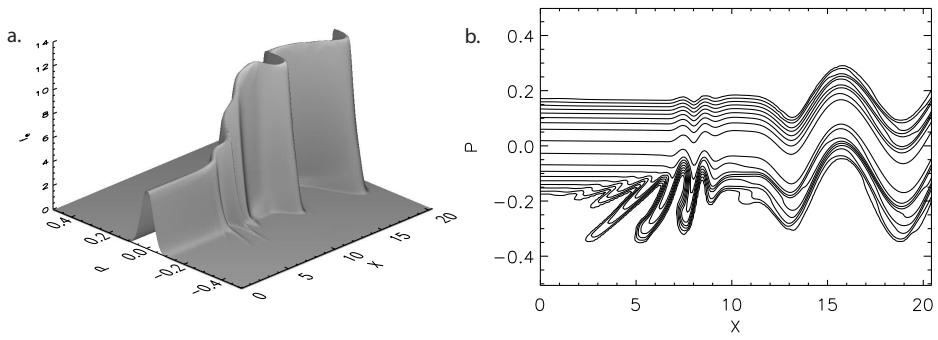

Figure 2.9: **a.** Isometric view of the electron distribution function f_e and, **b.** contour plot of $\log(f_e > 10^{-6})$ at time $\tilde{t} = 56$ from a simulation of the interaction of a Langmuir wave with an ion density hole (created and maintained via the prescribed immobile ion distribution of Fig.2.7a). A Langmuir wave ($\tilde{\lambda}_L = 2\pi$, $\delta n_e = 0.12$) has encountered the density hole of depth $\Delta = 0.6$ and gradient $\eta = 0.5$. The incoming wave breaks as it moves into the density hole, producing a strong localised electric field which accelerates electrons from the bulk of the distribution to form a jet.

assume the energy gain of electrons accelerated by the breaking wave is a positive, continuous, single-valued function of their initial position (i.e. their proximity to the breaking wavefront). From this, construct an expression for the electron density as a function of energy gain $\Delta\epsilon$. However, there is the possibility that two electrons from different spatial positions could achieve the same energy gain, which must be accounted for. Therefore, the domain is partitioned into regions where the number density of accelerated electrons is a single valued function of $\Delta\epsilon$, as shown schematically in Fig.2.10. The total number of accelerated electrons N^{Jet} is given by integrating the electron density over the spatial region S_0 from which electrons are accelerated:

$$N^{Jet} = \int_{S_0} n(\tilde{x}_0) d\tilde{x}_0 \tag{2.26}$$

where $\tilde{x}_0$ represents the initial position of the electron. This can be rewritten in terms of a new variable $\Delta\epsilon(\tilde{x}_0)$, the energy gain as a function of initial position, to give

$$N^{Jet} = \sum_j \int_{Q_j} n_j \left(\tilde{x}_0 \left(\Delta\epsilon\right)\right) \left|\frac{d\Delta\epsilon}{d\tilde{x}_0}\right|_j^{-1} d\Delta\epsilon \tag{2.27}$$

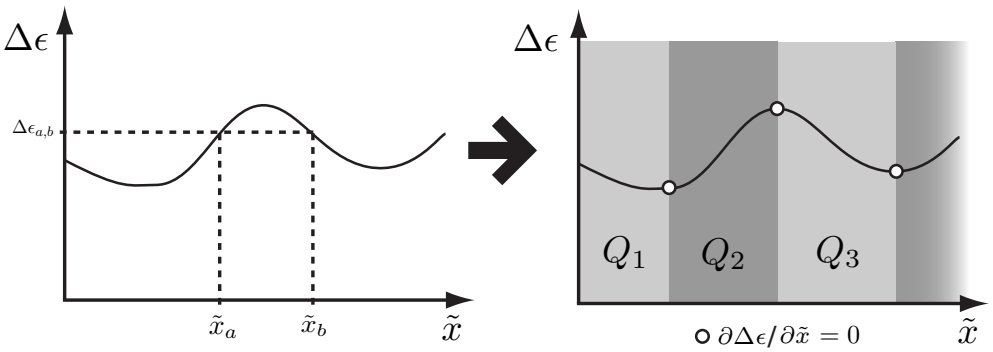

Figure 2.10: Schematic representation of the decomposition of the spatial domain S_0 into sub-domains $\{Q_j\}_{j\in\mathbb{N}}$ at Eq.(2.27). The domain S_0 represents the region of space from which electrons are accelerated to form a phase space jet. In order to find the energy spectrum, $n(\Delta\epsilon)$ for a phase space jet, one requires $\Delta\epsilon(\tilde{x})$. However, the possibility that $\Delta\epsilon$ could be multi-valued with respect to $\tilde{x}$ must be accounted for, for example $\Delta\epsilon(\tilde{x}_a) = \Delta\epsilon(\tilde{x}_b) = \Delta\epsilon_{a,b}$. Dividing S_0 into $\{Q_j\}_{j\in\mathbb{N}}$, where the sub-domain boundaries are defined by the condition that $\partial\Delta\epsilon/\partial\tilde{x} = 0$, avoids the problem of $\Delta\epsilon(\tilde{x})$ being multi-valued.

Here the region of integration S_0 is partitioned into sub-domains $\{Q_j\}_{j\in\mathbb{N}}$: within each sub-domain Q_j, the function $\Delta\epsilon(\tilde{x}_0)$ is single valued and has no turning points, as illustrated in Fig.2.10. The boundaries between the sub-domains are defined by the location of the turning points of $\Delta\epsilon(\tilde{x}_0)$. Denoting the energy spectrum within the jet as a function of energy gain by $n^{Jet}(\Delta\epsilon)$, the total number of electrons in the jet N^{Jet} can be written as an integral of n^{Jet} over $\Delta\epsilon$

$$N^{Jet} = \int_{S_0} n^{Jet}(\Delta\epsilon) d\Delta\epsilon \tag{2.28}$$

Equating this to Eq.(2.27) gives

$$n^{Jet}\left(\Delta\epsilon\right) = \sum_j n_j\left(\tilde{x}_0\left(\Delta\epsilon\right)\right) \left|\frac{d\Delta\epsilon}{d\tilde{x}_0}\right|_j^{-1} \tag{2.29}$$

The function $x_0(\Delta\epsilon)$ comes from the potential function of the Langmuir wave. Since the electric field of the wave near to breaking will be of nonlinear sawtooth form, its potential $\tilde{\phi}_L$ can be represented [54] by a parabolic function with amplitude $\tilde{\phi}_0$

$$\tilde{\phi}_L = \tilde{\phi}_0 \left(\frac{4\tilde{x}_0^2}{\tilde{\lambda}_L^2} - \frac{4\tilde{x}_0}{\tilde{\lambda}_L}\right) \tag{2.30}$$

over the range of one wavelength $\tilde{\lambda}_L$. From the assumption that electrons accelerate using the local potential energy of the Langmuir wave, it follows that $\Delta\epsilon(\tilde{x}_0) = \tilde{\phi}_L(\tilde{x}_0)$, with the maximum possible energy gain $\Delta\epsilon_{max} = \tilde{\phi}_0$:

$$\Delta\epsilon = \Delta\epsilon_{max} \left(\frac{4\tilde{x}_0^2}{\tilde{\lambda}_L^2} - \frac{4\tilde{x}_0}{\tilde{\lambda}_L}\right) \tag{2.31}$$

Inverting this expression yields

$$\tilde{x}_0 = \tilde{\lambda}_L \left(1 + \left(1 + \Delta\epsilon/\Delta\epsilon_{max}\right)^{1/2}\right)/2 \tag{2.32}$$

while differentiating with respect to $\tilde{x}_0$ gives

$$\left|\frac{d\Delta\epsilon}{d\tilde{x}_0}\right| = \Delta\epsilon_{max} \left(\frac{8\tilde{x}_0}{\tilde{\lambda}_L^2} - \frac{4}{\tilde{\lambda}_L}\right) \tag{2.33}$$

Substituting Eqs.(2.32) and (2.33) into Eq.(2.29), for a constant background density profile, gives the energy spectrum for a single phase space jet:

$$n^{Jet}(\Delta\epsilon) = n^{Jet}(0) \left(\frac{1}{\left(1 + \Delta\epsilon/\Delta\epsilon_{max}\right)^{1/2}}\right) \tag{2.34}$$

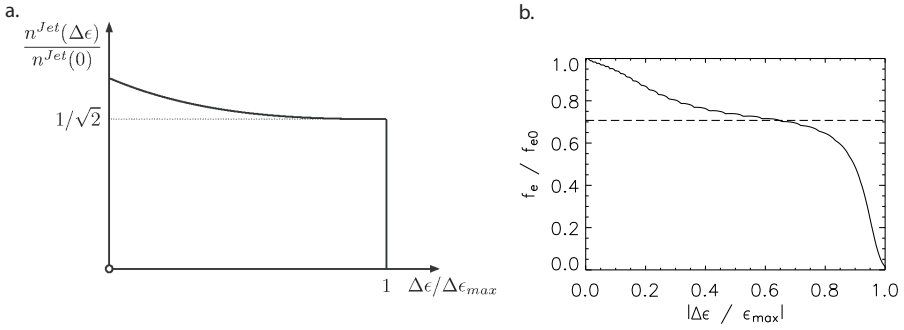

Figure 2.11: Similarity of predicted and measured forms of the energy distribution of electrons within a jet. **a.** Analytical result Eq.(2.34). **b.** The value of the distribution function f_e, normalised to its value f_{e0} at the base of the phase space jet. The energy gain of electrons in the phase space jet is normalised to the maximum observed energy $\approx 5MeV$.

Here the equation is normalised using $n^{Jet}(\Delta\epsilon = 0) = n_0\tilde{\lambda}_L/4\Delta\epsilon_{max}$, for a local electron density of n_0. It follows that the ratio of highest energy to lowest energy electrons within the jet is given by

$$n^{Jet}(\Delta\epsilon_{max})/n^{Jet}(\Delta\epsilon = 0) = 1/\sqrt{2} \tag{2.35}$$

The analytically derived energy spectrum Eq.(2.34), shown in Fig.2.11a, is consistent with the electron distribution function that is obtained from the simulations discussed earlier. Figure 2.11b shows a plot of f_e, normalised to its value f_{e0} at the base of the phase space jet, along the ridge of the phase space jet shown in Fig.2.5.

2.5 Summary

Shortly after exposing a fully relativistic Vlasov-Poisson system to a strong external driving field at resonance $\omega_0 = \omega_{pe}$, the formation of fine structures in the electron distribution function are observed. They correspond to the acceleration of a small population of electrons up to high energies (≈ 5MeV). These phase space jets result from the breaking of Langmuir waves (initially excited by the driving field) in the density gradients of cavitons formed via the ponderomotive force exerted by the external driving

field. Restricting the presence of the driving field to $\tilde{t} < 10$ allows direct acceleration by the driving filed to be ruled out as a mechanism. The origin of the small populations of electrons which form the jets has been explained by the breaking of Langmuir waves. A necessary condition for the formation of jets, and estimate the energy distribution of electrons within the phase space jet, has been derived, starting from a basic fluid treatment - this is supported by further numerical simulations. This process may arise whenever Langmuir waves move through a strong density gradient, and is not limited to one dimension or to caviton formation. It may therefore require consideration in laser-plasma interaction contexts spanning inertial confinement fusion and particle acceleration.

Chapter 3

Particle Acceleration in Astrophysical Plasmas

The work in this chapter is based on work submitted for publication [N. J. Sircombe, M. E. Dieckmann, P. K. Shukla and T. D. Arber, *Stabilisation of BGK modes by relativistic effects*, Astronomy and Astrophysics, In Press]. Some elements of the work also feature in [M. E. Dieckmann, N. J. Sircombe, M. Parviainen, P. K. Shukla and R. O. Dendy, *Phase speed of electrostatic waves: The critical parameter for efficient electron surfing acceleration*, Plasma Phys. Control. Fusion **48** (2006) 489] which also deals with PIC simulations of supernova remnant particle acceleration. This chapter focuses on the elements directly relating to the electrostatic Vlasov simulation of particle acceleration mechanisms.

3.1 Background

Cosmic rays consist of a small fraction of extremely high energy electrons ($\approx 10^{14}$eV). These are believed to be accelerated by Supernova remnant (SNR) shocks. As the blast shell created by a supernova expands into the interstellar medium (ISM) elctrons can be accelerated from the background population via a process known as first order Fermi acceleration [55, 56, 57, 58].

3.1.1 Fermi Acceleration at Quasi-Perpendicular and Quasi-Parallel Shocks

In Fermi Acceleration, electrons are repeatedly reflected across the shock front gaining energy at each crossing. In this manner, electrons can achieve ultra-relativistic velocities. In quasi-perpendicular shocks, the magnetic field is near perpendicular to the shock normal. By contrast, the magnetic field in a quasi-parallel shock is orientated near parallel to the shock normal. The microstructures of both types of shock have a common feature - the reflection of ions and electrons. At quasi-perpendicular shocks, the reflected particles gyrate for a partial gyro-orbit before encountering the shock again and being swept through into the downstream region. For quasi-parallel shocks, reflected particles stream away along the magnetic fields and diffuse back across the shock by scattering on upstream magnetic inhomogeneities [57, 59], providing an efficient acceleration mechanism to ultra-high energies.

3.1.2 The Injection Problem

In the case of both quasi-parallel and quasi-perpendicular shocks, the particles must initially be energetic enough to make repeated crossings of the shock front. This necessitates an initially energetic background electron population; with kinetic energies of the order of 100keV [60], higher than expected in the ISM or stellar wind of the progenitor. This 'seed' electron population must, therefore, be created via a different acceleration mechanism. For the case of quasi-perpendicular shocks, a promising candidate for the electron pre-acceleration mechanism is electron surfing acceleration (ESA)[61]. Electrons trapped in an an electrostatic wave traveling across the magnetic field experience an acceleration perpendicular to both the magnetic field and the wave direction. In order for the ESW to produce the seed population required for Fermi acceleration there must exit stable, large amplitude electrostatic waves (ESWs). Such waves can be excited as follows. As the shock front of a supernova remnant expands into the ISM, it reflects a substantial fraction of the ISM ions, as observed in simulations [62, 63]. The reflected ions form a beam that can reach a peak speed comparable to twice the shock speed in the ISM frame of reference [64]. This ion beam can then be reflected by the

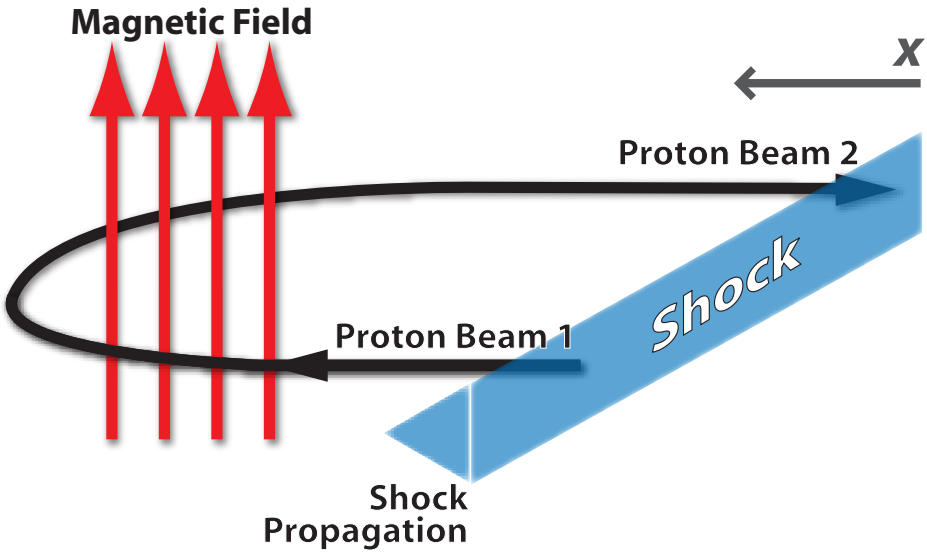

Figure 3.1: As the SNR shock expands it reflects a fraction of the ISM protons. These protons move back into the upstream region and form beam 1. The upstream $\mathbf{B}$ rotates beam 1 which returns as beam 2. The simulation box covers a one dimensional region of x in front of the shock sufficiently small that it can be assumed to be spatially homogeneous and one dimensional.

upstream magnetic field to produce two counter propagating ion beams (as shown in Fig.3.1) which relax by their interaction with electrostatic and electromagnetic waves. The proton beams can excite ESWs via the relativistic Buneman instability. Recent numerical studies [62, 65, 66, 67, 68] have examined these mechanisms with a particular focus the ESW lifetime.

A full treatment of the ESA requires a multi-dimensional model with magnetic, as well as electrostatic, fields.This chapter focusses on a simplified one-dimensional electrostatic model, adopted in previous studies, to investigate the excitation and saturation of ESWs in a system dominated by the presence of two counter propagating ion beams, as well as secondary acceleration mechanisms.

3.1.3 Outline

In the remainder of this chapter the electrostatic Vlasov model is used to investigate the dependence of the ESW stability and electron acceleration on the ion beam speed v_b. These simulations are in agreement with previous studies, displaying a reduction in wave stability with increasing non-relativistic beam speeds and a return to stability at higher, relativistic, speeds.

The ESWs saturate by the trapping of electrons, forming BGK modes. These are in turn unstable to the sideband instability, a resonance between trapped electrons and secondary ESWs. Simulations demonstrate that the collapse of these BGK modes couples energy to three families of waves. Firstly a continuum of electrostatic waves that move with approximately the beam speed. Secondly, for high beam speeds the growth of quasi-monochromatic modes with frequency comparable to the Doppler-shifted bouncing frequency of the trapped electrons in the wave potential. These are the sideband modes [69]. Thirdly, waves that do not have a clear connection to any characteristic particle speed. These modes appear to be produced by parametric coupling and can reach phase speeds well above the maximum speed the initial trapped electron population reaches. They grow to sufficient amplitude to trap and accelerate electrons. This mechanism has not been previously observed in simulations [66, 67]. In principle, such a mechanism would allow the ion beams reflected by shocks expanding at speeds comparable to SNR shocks to accelerate electrons to energies in excess of 100 keV - suffichent to undergo Fermi acceleration.

3.2 The system

3.2.1 Physical model

Consider a small interval of the ISM plasma just ahead of a SNR shock (see Fig. 3.1) and treat the ISM plasma as an electron proton plasma with a spatially homogeneous Maxwellian velocity distributions. The simulation box is placed close to the SNR shock, so that the shock-reflected ISM protons can cross it. The protons that have just been reflected constitute beam 1 and beam 2 represents the protons that return to the shock

after they have been rotated by the global foreshock magnetic field [64]. The magnetic field in this region is expected to be turbulent. The large scale average $\mathbf{B}$ is approximately orthogonal to the shock normal so that the ion beam experiences a field sufficient to rotate it back towards the shock. However on a smaller scale, at the shock front, in the region of the simulation box the turbulent field may be aligned with the proton beams. This is clearly a severe restriction to the applicability of the model. Ideally one should also consider a higher dimensional system and relax the assumption that the proton beams are directed along $\mathbf{B}$. However, this description has been used extensively in the literature. It serves as simple model for the stability of ESWs, which has implications for the effectiveness of ESA.

The system is modeled using the electrostatic, relativistic Vlasov-Poisson solver. The size of the simulation box is small compared to the distance across which the beam parameters change, due, for example, to a rotation by $\mathbf{B}$ or by the scattering of beam protons by the ESWs. System boundaries are taken to be periodic with Maxwellian velocity distributions for both beams. These have the same mean speed, $|v_b|$, but move in opposite directions giving a zero net current in the simulation box. Beam 2 is initialised with a higher temperature than beam 1 to reflect the scattering of the beam protons as they move through the foreshock. These velocity distributions are shown in Fig.3.2

3.2.2 Linear instability

The plasma frequency of each species i is given by $\omega_{p,i} = \left(e^2 n_i / m_i \epsilon_0\right)^{1/2}$ where e, n_i, m_i and ϵ_0 are the magnitude of the elementary charge, the number density of species i in the rest frame of the species, the particle mass of species i and the dielectric constant. All $\omega_{p,i}$ are defined in the box frame of reference. Species 1 and 2 are the ISM electrons and protons. Species 3 is beam 1 and species 4 is beam 2.

The system as described is unstable to the Buneman instability [70]. For the case of a cold non-relativistic plasma, the growth rate can be found by solving the dispersion relation

$$1 - \sum_i \frac{\omega_{p,i}^2}{(\omega - k v_i)^2} = 0 \tag{3.1}$$

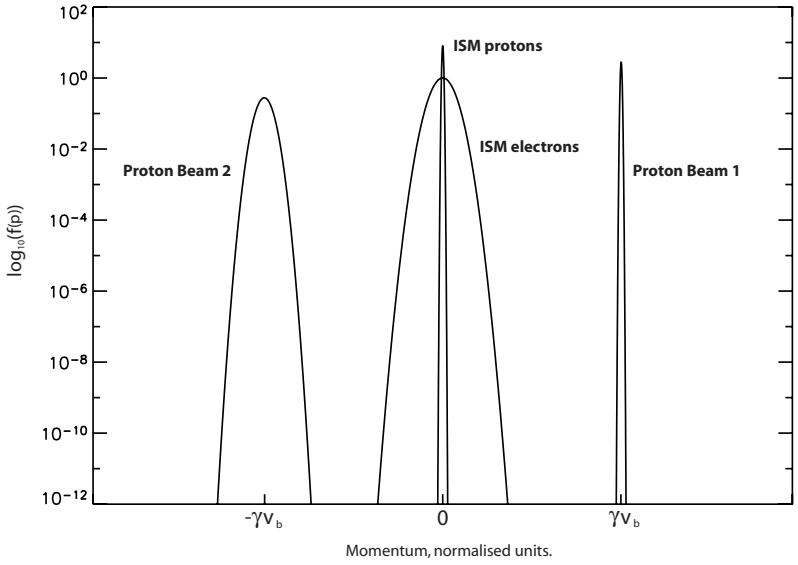

Figure 3.2: The initial velocity distribution showing the ISM electrons and protons, proton beam 1 and proton beam 2. The expanding SNR shock reflects a fraction of the ISM protons which form beam 1. The upstream $\mathbf{B}$ rotates beam 1 to create beam 2. Since the beam has been scattered by ESWs on its path through the foreshock, its thermal spread has increased. Both beams can grow ESWs with a speed similar to v_b which saturate by their interaction with the ISM electrons. By assuming that the plasma parameters do not change over the simulation box,the plasma can be represented by the four spatially homogeneous species shown.

where v_i is the streaming velocity of the species, zero for species 1 and 2, $\pm v_b$ for species 3 and 4. Due to their greater inertia, the ions dominate Eq.(3.1) and the contribution of species 1 can be neglected. Together with relativistic corrections, the linear dispersion relation becomes

$$\frac{\omega_{p,1}^2}{\omega^2} + \frac{\omega_{p,3}^2}{\gamma^3(v_b)(\omega - v_b k)^2} + \frac{\omega_{p,4}^2}{\gamma^3(v_b)(\omega + v_b k)^2} - 1 = 0 \tag{3.2}$$

in the cold plasma limit.

During the linear growth phase, each proton beam will grow an ESW by its streaming relative to the electrons. Both waves are well separated in their phase speed and the linear dispersion relation can be solved separately for each ESW by neglecting either the term with $\omega_{p,3}$ or $\omega_{p,4}$ in Eq.(3.2) [70, 71]. The most unstable Buneman mode has a frequency, in the box frame, of $\omega_u \approx \omega_{p,1}$, a wave number $k_u \approx \omega_{p,1} v_b^{-1}$ and growth rate $\Omega \approx (3\sqrt{3}\omega_{p,3}^2 \omega_{p,1}/16)^{1/3}/\gamma(v_b)$. Taking a number density ratio of $n_3/n_1 = 0.2\gamma(v_b)$, with $n_4 = n_3$ and $n_2 = n_1 - n_3 - n_4$ in the box frame of reference. These parameters are representative for a shock with a high Mach number [59]. This density ratio gives $\omega_{p,1}/\omega_{p,3} \approx 96\gamma(v_b)^{-0.5}$ and a growth rate of $\Omega \approx 0.033/\gamma(v_b)^{2/3}$. The growth rate is reduced by increasing the plasma temperature. The wave length of the most unstable ESW is $\lambda_u = 2\pi/k_u$. The sideband instability couples energy to modes with $k \leq k_u$, for non-relativistic phase speeds. The simulation box length is chosen as $L = 2\lambda_u$ to resolve more than one unstable sideband mode, which leads to a wave collapse. This L is short compared to the typical size of the foreshock which justifies the spatially homogeneous initial conditions and periodic boundary conditions. The amplitude of the initial ESW and that of the sideband modes are used as indicators of the wave collapse.

3.2.3 Numerical Simulation

As described in chapter 2, in the absence of a magnetic field the one dimensional relativistic Vlasov-Poisson system of electrons and protons is given by the Vlasov equation for the electron distribution function $f_e(x, p, t) = f_1$

$$\frac{\partial f_e}{\partial t} + \frac{p}{m_e \gamma}\frac{\partial f_e}{\partial x} - eE\frac{\partial f_e}{\partial p} = 0, \tag{3.3}$$

the Vlasov equation for the proton distribution function $f_p(x,p,t) = f_2 + f_3 + f_4$

$$\frac{\partial f_p}{\partial t} + \frac{p}{m_p \gamma}\frac{\partial f_p}{\partial x} + eE\frac{\partial f_p}{\partial p} = 0, \tag{3.4}$$

and Poisson's equation for the electric field, Eq.(2.3) The Vlasov-Poisson system is solved using a version of the code parallelised in momentum space using domain decomposition and Message Passing Interface (MPI) code. This approach is detailed, for the more complex problem of parallelisation in x-space, in chaper 4.

3.2.4 Initial Conditions

It is common to adopt a reduced mass ratio in numerical simulations - as in section 2.2.2 and, for example in the context of SNR shocks, in Ref. [72]. Previous work has found the evolution of the shock and the role of the two-stream and Buneman instabilities in the heating of the particle populations to be dependent on the mass ratio used [65, 73, 74]. Throughout this chapter a realistic mass ratio, $m_p/m_e = M_r$, of $M_r = 1836$ is adopted at the expense of computational time.

The system length L is resolved by 512 cells in the $x-$direction, each with length $\Delta x = \pi v_b/128\omega_{p,1}$. To accurately resolve the filamented phase space distributions of the particles that result from the sideband instability [68], a momentum-space grid with between 4096 and 16384 grid points (N_p) is used. This ensures that the momentum grid spacing for each species, $\Delta p_{x,i}$, is small. Specifically, $\Delta p_{x,i} < 0.1 m_i v_{th,i}$ where $v_{th,i}^2 = \kappa T_i/m_i$ is the thermal speed of species i.

The temperatures of the four species are set to $T_1 = 5.4\times10^5$ K, $T_2 = T_3 = 10T_1$ and $T_4 = 100T_2$. This implies that $v_{th,1} = 10^{-2}c$. Each is described by a Maxwellian momentum distribution of the form

$$f_i(p) = C_i \exp\left(\frac{-m_i\left(\gamma(p-p_0)-1\right)}{T_i}\right) \tag{3.5}$$

where p_0 is the initial momentum offset, zero for species 1 and 2, $\pm v_b/(1-v_b^2/c^2)^{0.5}$ for species 3 and 4 respectively. For each species the constant C_i is calculated to ensure that $\int f_i dp = n_i$ and that $\int (f_2 + f_3 + f_4)\, dp = n_1$, so there is no net charge in the system.

In order to excite the linear instability, the proton distribution (species 2, 3 and 4) is perturbed at the most unstable wavenumber with a density perturbation of the form $n' = a \cos k_u x$, where a is small, typically of the order of 1% of the background density.

3.3 Simulation results

Simulations use the system of normalised units given in section 2.2.2. Where appropriate in the figures, x is re-normalised in units of $2\pi/k_u$, the most unstable wavelength for a given initial beam speed. This ensures that the spatial units are identical for all beam speeds.

3.3.1 Growth and Non-Linear Saturation of the Buneman Instability

Figure 3.3 shows the initial growth stage of the most unstable mode, $E(k = k_u)$, for a range of initial beam velocities. From these the growth rate of the instability (Ω), in normalised units, are estimated to be $0.0256, 0.0264, 0.0270, 0.0246, 0.0201$ and 0.0137 for beam speeds of $v_b = 0.15c, 0.2c, 0.4c, 0.6c, 0.8c$ and $0.9c$, respectively. These compare favourably with the linear theory. Writing $\alpha(v_b)$ as the ratio between observed and theoretical growth rates we find; $\alpha(0.15c) \approx 0.79$, $\alpha(0.2c) \approx 0.81$, $\alpha(0.4c) \approx 0.87$, $\alpha(0.6c) \approx 0.87$, $\alpha(0.8c) \approx 0.86$ and $\alpha(0.9c) \approx 0.72$. As detailed in [67], where a similar systematic reduction has been observed in PIC simulations (in this case by 15-20%), this is connected to the fast growth rate of the instability itself. The assumption that there is a single discrete unstable mode is not entirely accurate. Rather, there is a spread in frequency over which unstable waves are excited. As a result, the growth rate should be lower than Ω, since a the energy is spread over damped frequencies close to ω_u. The ESWs saturate by the trapping of electrons and the formation of BGK modes. This is shown in Fig. 3.4, for the case of $v_b = 0.2c$, and Fig. 3.5 for $v_b = 0.9c$. Phase-space holes characteristic of particle trapping are visible in the electron distribution. While the saturation mechanism is the same in both cases, for the high velocity beam two counter-propagating BGK modes develop. This is because at lower beam speeds the ESW

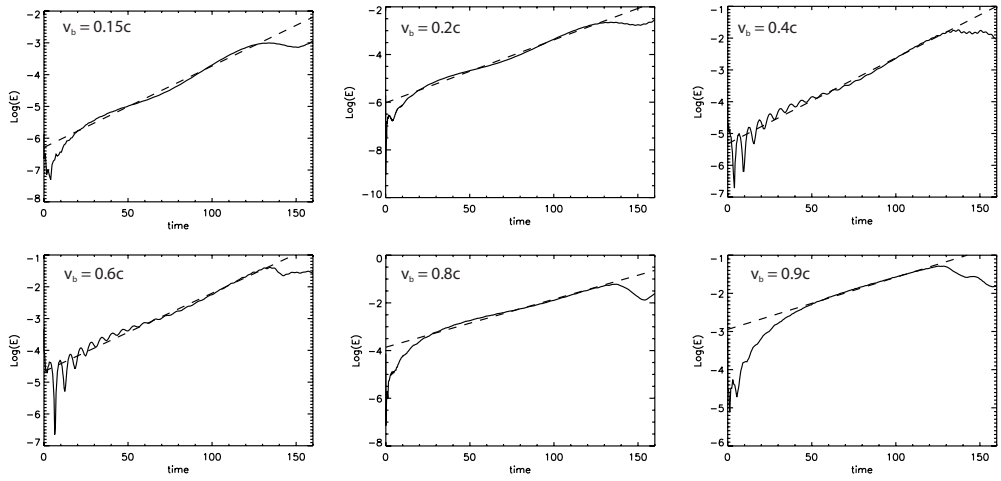

Figure 3.3: The logarithmic amplitude of the most unstable mode $E(k_u, t)$ is plotted against time, in normalised units, for a variety of beam speeds. The dashed lines on each plot represent a linear fit over the region of exponential growth. Using this linear fit gives growth rates for the relativistic Buneman instability, in normalised units, of $\Omega \approx 0.0256$, 0.0264, 0.0270, 0.0246, 0.0201 and 0.0137 for beam speeds of $v_b = 0.15c$, $0.2c$, $0.4c$, $0.6c$, $0.8c$ and $0.9c$, respectively.

instability driven by the cooler beam (at $+v_b$) dominates whereas for higher, relativistic, beam speeds forwards and backwards propagating ESWs grow in unison. At lower beam speeds the increased temperature of beam 2 (species 4) is more significant, since the thermal velocity of the beam is a larger proportion of the beam speed than is the case at $v_b = 0.9c$. Thus, the growth rate for the hot beam is sufficiently reduced for the system to be dominated by the growth of the cooler proton beam (species 3). The growth of a counter propagating ESW which begins to trap electrons after $t = 150$ is observed. However, the final momentum distribution is dominated by electrons accelerated by the ESW with positive phase velocity. At $v_b = 0.9c$, the thermal spread of both proton beams is negligible in comparison to the beam velocities the growth and saturation of ESWs associated with both beams is observed.

3.3.2 Wave Collapse and Secondary Electron Trapping

Trapping of electrons in electrostatic waves produces BGK modes which eventually collapse via the sideband instability. The sideband instability is due to the nonlinear

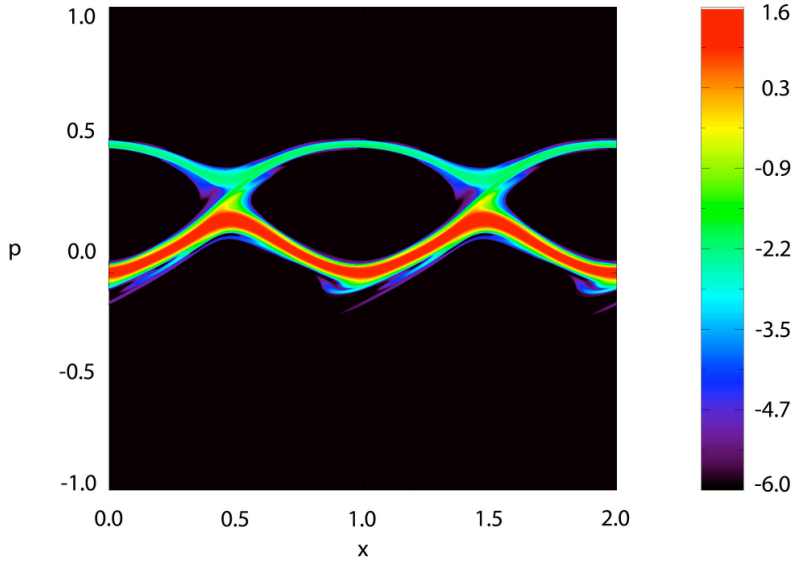

Figure 3.4: Contour plot of $\log(f_e > 10^{-6})$ at time $t = 150$ for a system with an initial beam velocity of $v_b = 0.2c$. The exponential growth of the ESW is in the process of saturating via the trapping of electrons, forming a BGK mode at $p \approx +0.2$.. The thermal spread of beam 2 inhibits its growth slightly, allowing the system to become dominated by one ESW. Hence, we do not observe electron trapping around $p \approx -0.2$. Here x is given in units of $2\pi/k_u$.

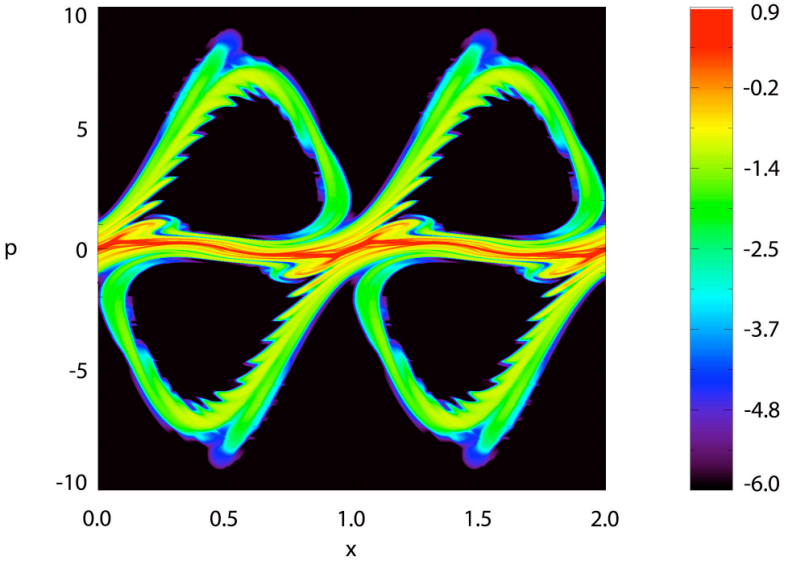

Figure 3.5: Contour plot of $\log(f_e > 10^{-6})$ at time $t = 200$ for a system with a relativistic initial beam velocity of $v_b = 0.9c$. The exponential growth of the ESW is in the process of saturating via the trapping of electrons, forming a pair of BGK modes at $p \approx \pm 3$. The reduced significance of the higher temperature of species 4, with respect to species 3, at high beam speeds allows the growth of forwards and backwards propagating ESWs simultaneously. Here x is given in units of $2\pi/k_u$.

oscillations of the electrons in the potential of the ESW. For electrons close to the bottom of the wave potential, their oscillation is that of a harmonic oscillator. The monochromatic bouncing frequency is Doppler shifted, due to the phase speed of the ESW. These sidebands can couple to secondary high-frequency ESWs, which must have a wave number $k \leq k_u$. The sideband instability is a limiting factor for the lifetime of the ESW which has implications in the presence of an external magnetic field in particular. Figure 3.6 shows the amplitude of the ESW driven by beam 1 at $k = k_u$ for beam speeds ranging from $0.15c$ to $0.9c$. The ESWs moving at nonrelativistic phase speeds saturate smoothly. Their lifetime is significant and, in the presence of a weak external magnetic field, $\mathbf{B}$, orthogonal to the wave vector, $\mathbf{k}$, the trapped electrons would undergo a substantial period of ESA [75]. However, the ESA is proportional to $v_{ph}|\mathbf{B}|$ and the comparatively low v_{ph} would limit the maximum energy the electrons can reach. The ESW driven by the beam with $v_b = 0.6c$ grows to a larger amplitude and then collapses abruptly, which confirms earlier findings [76] that the BGK modes become more unstable the larger the ratio between beam speed and electron thermal speed becomes. The Lorentz force, $ev_{ph}|\mathbf{B}|$, exerted by a $\mathbf{B}\perp\mathbf{k}$ would be significantly higher than for the case $v_b = 0.15$, however the short lifetime of the wave prevents electrons from reaching highly relativistic speeds. By increasing the beam speed to $v_b = 0.9c$ a stabilisation of the ESW is achieved, in line with the results in Ref.[67]. Here the Lorentz force is strong and the lifetime of the saturated ESW is long constituting a formidable electron accelerator, provided the electrostatic field evolution is not strongly influenced by $\mathbf{B}$.

The principal results from each beam speed are summerised below. Window Fourier Transforms of the amplitudes of the ESWs at the wavenumbers $k_u/2$ and k_u are used to identify the origins of the various observed modes.

3.3.3 Beam Speed, $v_b = 0.15c$.

Figure 3.7 displays a strongly asymmetric ESW growth for $v_b = 0.15c$. Here the thermal spread of the individual plasma species is not small compared to v_b. Therefore the ESW driven by the cooler beam 1 grows and saturates first. It collapses rapidly and this collapse inhibits a further growth of the ESW driven by beam 2. The initial

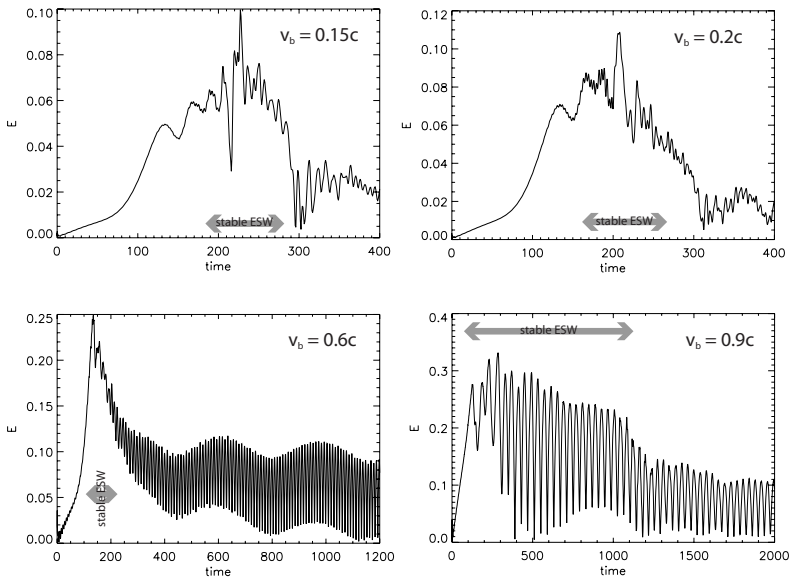

Figure 3.6: The time evolution of the ESW amplitudes with $k = k_u$ that are driven by beam 1 for beam speeds of $0.15c$, $0.2c$, $0.6c$ and $0.9c$. ESWs generated at non-relativistic beam speeds saturate smoothly and stabilise briefly. At $v_b = 0.6$ the ESW collapses abruptly and at relativistic beam speeds, $v_b = 0.9c$ we observe a stabilisation of the ESW for a period of almost $1000\omega_{p,e}^{-1}$, equivalent to almost 160 plasma periods. Approximate regions of stability are highlighted on each plot.

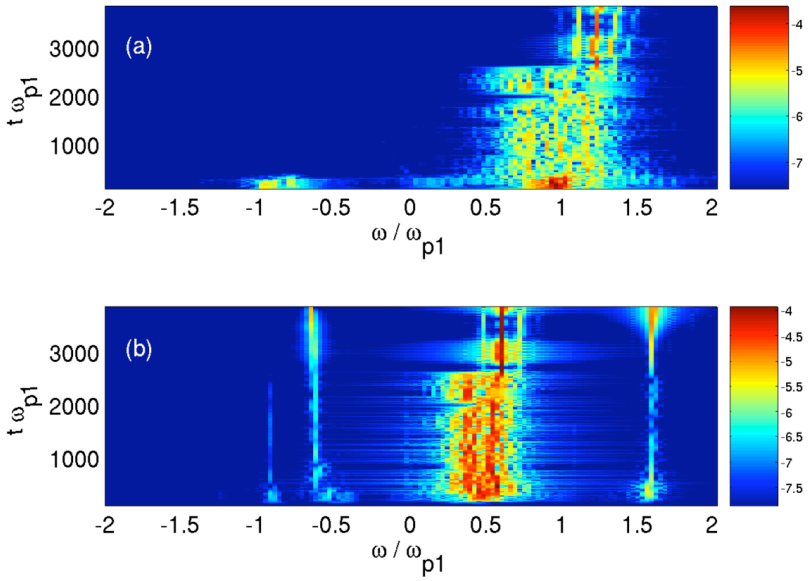

Figure 3.7: Reproduced from Ref.[77]. The ESW spectrum for a beam speed of $v_b = 0.15c$: **a.** shows the frequency power spectrum of $k_c = k_u$ and **b.** shows the frequency power spectrum of $k_c = k_u/2$ as a function of time. The ESW driven by beam 1 with $v_b > 0$ corresponds to the wave with $\omega = \omega_{p,1}$ in **a**.

monochromatic ESW collapses into a broad wave continuum centred around $\omega = \omega_{p,1}$. There is an equivalent broad wave continuum for $k = k_u/2$ centred at $\omega = \omega_{p,1}/2$. These waves propagate at phase speeds comparable to v_b and represent the structures remaining of the initial BGK mode. The ESW spectrum at $k = k_u/2$ further shows two wave bands that are separated by a frequency of $\omega_{p,1}$ from the main peak. These two wave bands could be pumped by a beat between the turbulent structure centred at $\omega = \omega_{p,1}/2$, $k = k_u/2$, the turbulent structure centred at $\omega = \omega_{p,1}$ and $k = k_u$ and the Langmuir wave with $k = k_u/2$. Evidence for this is the correlation between both turbulent structures and the wave bands at $t \approx 2500$. At this time most wave power at $\omega \approx \omega_{p,1}/2$ is absorbed at $k \approx k_u/2$. At the same time wave power at $\omega \approx \omega_{p,1}$ is absorbed at $k = k_u$ while the power in the wave bands with $\omega \approx \omega_{p,1}/2$ and $\omega \approx 1.5\omega_{p,1}$ grows at $k = k_u/2$. The faster of these two has a phase speed of $\omega/k \approx 3v_b = 0.45c$. This beat wave is therefore considerably faster than the initial ESW. As shown in Fig.3.8 this mode is able to trap electrons, forming a BGK mode in the electron distribution

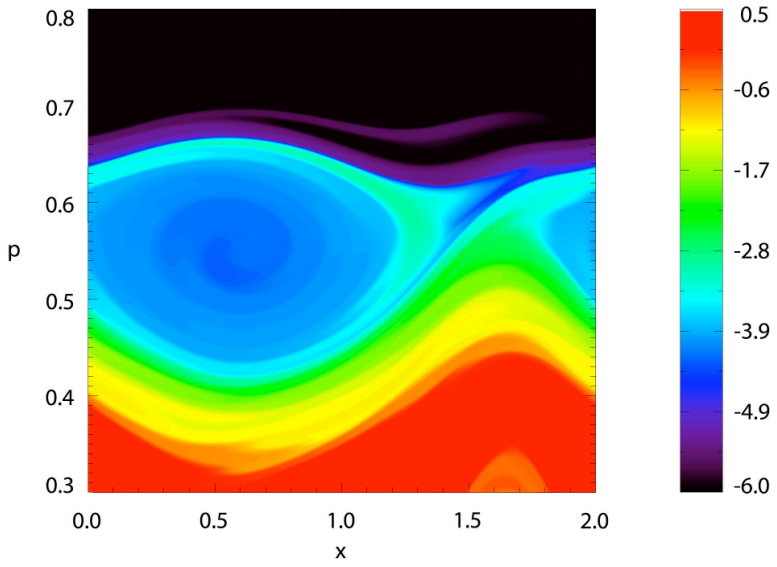

Figure 3.8: Contour plot of $\log(f_e > 10^{-6})$ for $v_b = 0.15c$ at the time $t = 3500$: The initial electron BGK modes have collapsed and they can be shown to form a plateau distribution at $p/m_e c < 0.3$. Centred at $p/m_e c \approx 0.52$ we find BGK modes driven by the beat wave.

centred around a momentum $p/m_e c \approx 0.52$ which corresponds to a speed $0.46c$. The fastest electrons of this BGK mode reach $p/m_e c \approx 0.68$ or a speed of $0.56c \approx 3.75 v_b$.

3.3.4 Beam Speed, $v_b = 0.2c$.

The simulation with $v_b = 0.2c$ displays similar wave coupling to the $v_b = 0.15c$ case as shown in Fig. 3.9. There is a turbulent ESW spectrum driven by the beam 1 centred at v_b with a spread corresponding to a significant fraction of the beam speed. Initially an ESW is also driven by beam 2 at $\omega \approx \omega_{p,1}$ but, in line with Fig.3.7, it collapses simultaneously with the ESW driven by beam 1. The turbulent wave spectrum with $\omega \approx \omega_{p,1}$ at $k = k_u$ appears to couple with the equivalent spectrum at $\omega \approx \omega_{p,1}/2$ at $k = k_u/2$ and the Langmuir wave with $\omega = \pm\omega_{p,1}$ and $k = k_u/2$ to give wave bands at $\omega \approx -0.5\omega_{p,1}$ and at $\omega \approx 1.5\omega_{p,1}$. The phase speed of the ESW band at $\omega \approx 1.5\omega_{p,1}$ is $\omega/k \approx 3v_b$ and that of the band at $\omega \approx \omega_{p,1}/2$ is $\omega/k \approx v_b$. Both bands are able to trap electrons, this is shown in Fig.3.10 with BGK modes centred at $p/m_e c \approx 0.75$ or a speed of 0.6c. These modes extend up to a peak momentum of $p/m_e c \approx 1$ or a speed

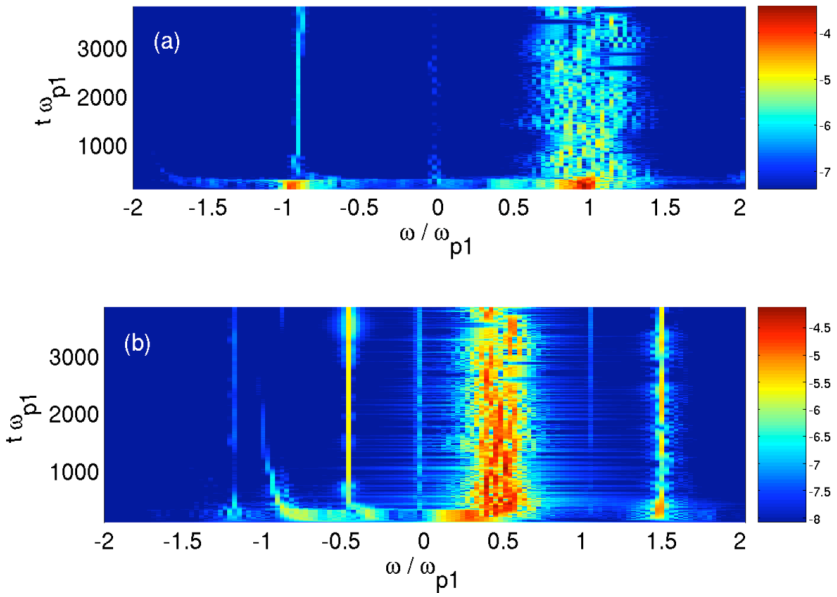

Figure 3.9: Reproduced from Ref.[77]. The ESW spectrum for a beam speed of $v_b = 0.2c$: **a.** shows the frequency power spectrum of $k_c = k_u$ and **b.** shows the frequency power spectrum of $k_c = k_u/2$ as a function of time. The ESW driven by beam 1 with $v_b > 0$ corresponds to the wave with $\omega = \omega_{p,1}$ in **a**

of $0.87c$, equivalent to $4.5v_b$.

3.3.5 Beam Speed, $v_b = 0.4c$.

As the beam speed is increased to $v_b = 0.4c$ the ESW driven by beam 1 stabilises and the collapsing ESW driven by beam 2 drives the broadband turbulence, as can be seen in Fig. 3.11.

ESWs grow at $k = k_u$ with $|\omega| \approx 2\omega_{p,1}$, since these ESWs have the same wave number as the initial wave they can not be produced by self-interaction of the initial ESW since this would also double the wave number. These high frequency waves correspond to the Doppler shifted bouncing frequency of the trapped electrons in the potential of the strong ESW. The fastest electrons reach approximately twice the phase speed v_{ph} of the ESW as can be seen, for example, at the lower beam speed of $v_b = 0.2c$ in Fig.3.4. These electrons are therefore, due to the fixed wave number k_u of the BGK modes, interacting with secondary ESWs with $\omega \approx 2\omega_{p,1}$. The ESWs with $|\omega| \approx 1.2\omega_{p,1}$ at

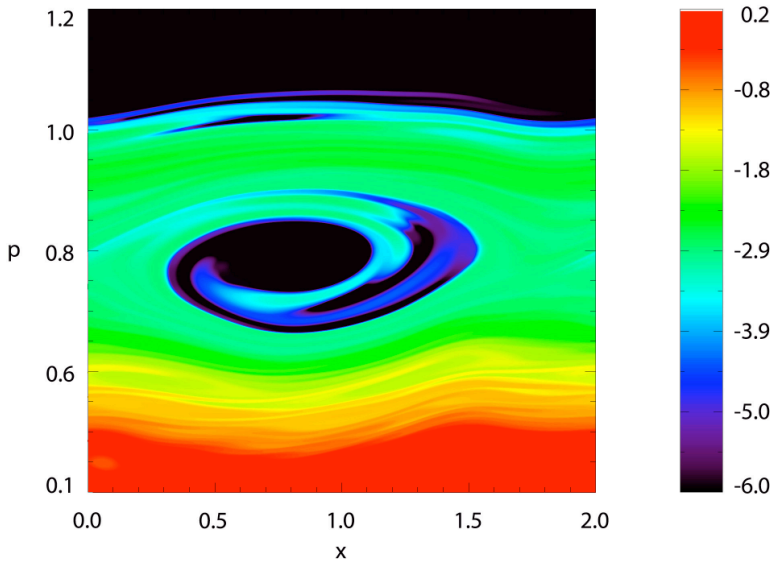

Figure 3.10: Contour plot of $\log(f_e > 10^{-6})$ for $v_b = 0.2c$ at the time $t = 2000$: The initial electron BGK modes have collapsed and form a plateau distribution. Centred at $p/m_e c \approx 0.75$ are BGK modes driven by the beat wave.

$k = k_u/2$ appear to be a result of beating between the ESWs with $|\omega| = \omega_{p,1}$ at $k = k_u$ and the ESWs with $|\omega| = \omega_{p,1}/2$ at $k = k_u/2$ and Langmuir waves.

3.3.6 Beam Speed, $v_b = 0.6c$.

The ESW wave spectrum for $v_b = 0.6c$ is similar to that for $v_b = 0.4c$. Again both beams grow strong ESWs close to $|\omega_u| = \omega_{p,1}$ but it is still the stronger ESW driven by beam 1 that stabilises while that driven by beam 2 collapses into a broadband spectrum. This is reflected by the ESW spectrum at $k_u/2$ which displays the strongest wave activity at $\omega \approx -\omega_{p,1}/2$. Two additional wave bands with frequencies $\omega \approx \omega_{p,1}$ are observed at $k_u/2$, i.e. long Langmuir waves are produced by the nonlinear processes. These waves have twice the phase speed of the initial ESWs and by their superluminal phase speed they can not interact resonantly with the electrons. At $k = k_u$ there are high-frequency modes at $|\omega| \approx 1.6\omega_{p,1}$ with a subluminal phase speed $\omega/k_u \approx 0.95c$. The phase speeds of these ESWs is higher than the peak speed the electrons reach in the inital BGK mode as shown in Fig. 3.13. Its growth cannot be explained by a streaming instability between

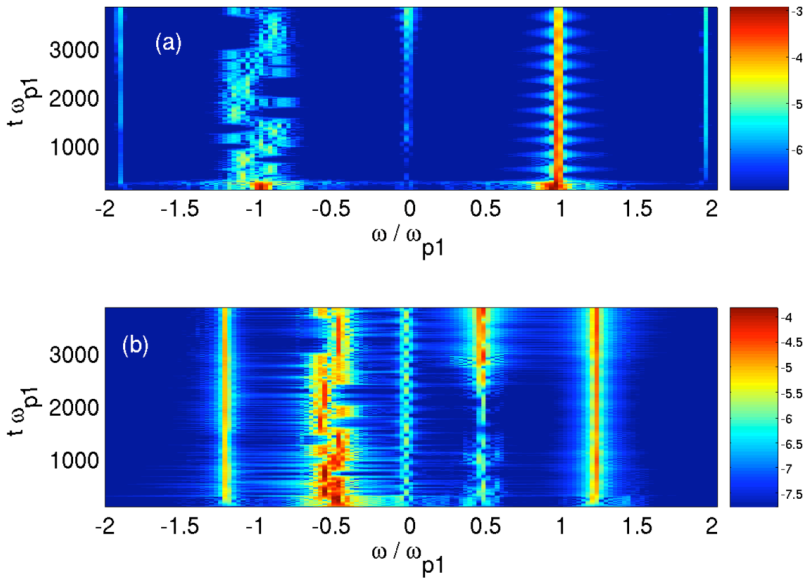

Figure 3.11: Reproduced from Ref.[77]. The ESW spectrum for a beam speed of $v_b = 0.4c$: **a.** shows the frequency power spectrum of $k_c = k_u$ and **b.** shows the frequency power spectrum of $k_c = k_u/2$ as a function of time. The colour scale shows logarithmic amplitude. The ESW driven by beam 1 with $v_b > 0$ corresponds to the wave with $\omega = \omega_{p,1}$ in **a**.

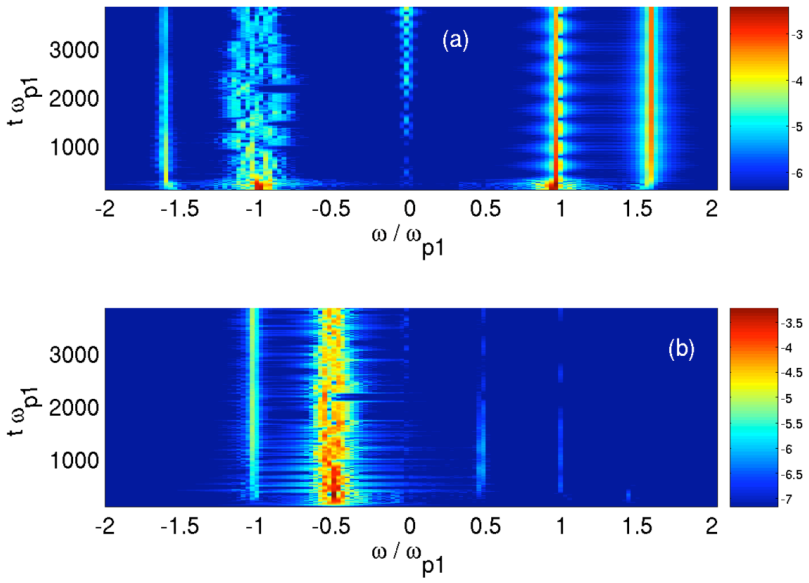

Figure 3.12: Reproduced from Ref.[77]. The ESW spectrum for a beam speed of $v_b = 0.6c$: **a.** shows the frequency power spectrum of $k_c = k_u$ and **b.** shows the frequency power spectrum of $k_c = k_u/2$ as a function of time. The colour scale shows logarithmic amplitude. The ESW driven by beam 1 with $v_b > 0$ corresponds to the wave with $\omega = \omega_{p,1}$ in **a**.

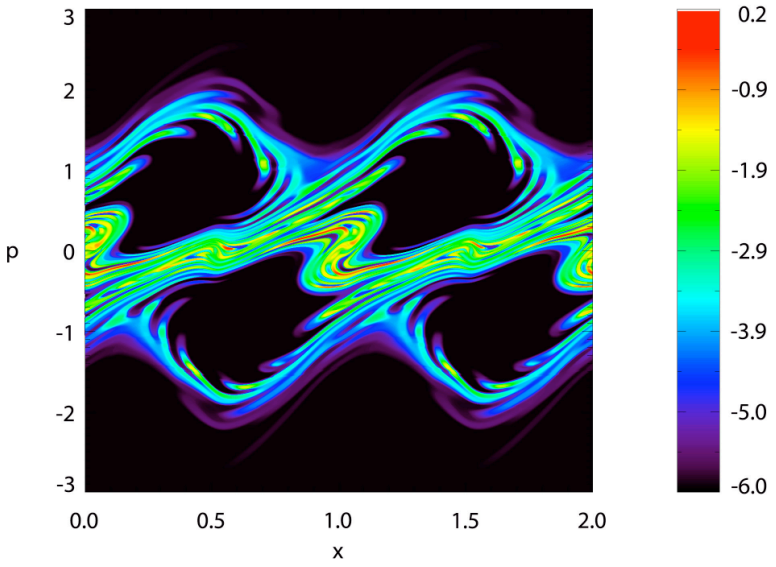

Figure 3.13: Contour plot of $\log(f_e > 10^{-6})$ for $v_b = 0.6c$ at the (early) time $t = 200$: The initial electron BGK modes have just been formed and the trapped electrons reach a momentum up to $p/m_e c \approx 3$.

the trapped electrons and, for example, the untrapped electrons. One can obtain phase speeds of the ESW bands that are higher than the speed of the trapped electron beam, however, by applying the relativistic Doppler shift to the electron bouncing frequency in the ESW wave potential. The rest frame of the ESWs moves with the speed $v_{ph} = 0.6c$. The frequency of the ESWs in the observer frame is, according to Fig.3.12, $\omega_o \approx 1.6\omega_{p,1}$. The relativistic Doppler equation gives a bouncing frequency of the electrons in the ESW frame of reference of $\omega_b = ([1 - v_{ph}/c]/[1 + v_{ph}/c])^{1/2}\omega_o = 0.8\omega_{p,1}$. Using the nonrelativistic estimate of the electron bouncing frequency in a parabolic electrostatic potential $\omega_b^2 = ek_u E/m_e$ and the corresponding width of the trapped electron island $v_{tr}^2 = 2eE/m_e k_u$ to eliminate the electric field E. this gives the relation; $\omega_b/k_u = v_{tr}/\sqrt{2}$. Taking the velocity width of the island of trapped electrons to be comparable with v_{ph} gives an estimate for $\omega_b \approx \omega_{p,1}/\sqrt{2}$ which is close to ω_o. The two sidebands observed in Fig.3.12 can be interpreted as as the Doppler shifted bouncing frequency of the electrons.

These sideband modes driven by the beams of trapped electrons have a phase

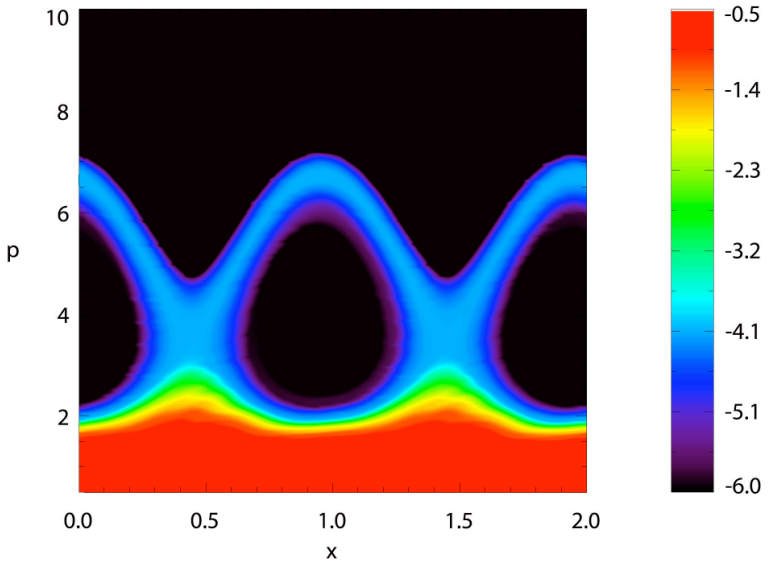

Figure 3.14: The electron momentum distribution for $v_b = 0.6c$ at the (late) time $t = 3500$: The initial electron BGK modes have collapsed and the electrons that are trapped by the sideband mode reach a momentum up to $p/m_e c \approx 7$.

speed that is just below c and a large amplitude. Since their phase speed is comparable to the fastest speed the electrons reach in the initial BGK mode, they should be capable of trapping some of these electrons. This is confirmed by Fig. 3.14 where BGK modes are centred at the momentum $p/m_e c \approx 3.4$ which accelerate electrons up to the peak momentum $p/m_e c \approx 7$ or a speed of $0.99c$.

3.3.7 Beam Speeds, $v_b = 0.8c$ and $v_b = 0.9c$.

As the beam speed is increased increase the beam speed to $v_b = 0.8c$ the qualitative evolution of the ESWs changes. At this high beam speed the thermal spread of the plasma species is negligible. The growth rates of the waves for both beams is approximately that of the cold beam instability and the ESWs grow symmetrically. Both saturated ESWs are stable. After the saturation each ESW shows a sideband, similar to that in Fig.3.13 at a frequency modulus $\omega \approx 1.3\omega_p$. The phase speeds of these sideband modes are just above c. There is a secondary growing mode at $k = k_u/2$ with frequency modulus $\omega \approx 0.8\omega_{p,1}$. The same growth of sideband modes is observed for the fastest

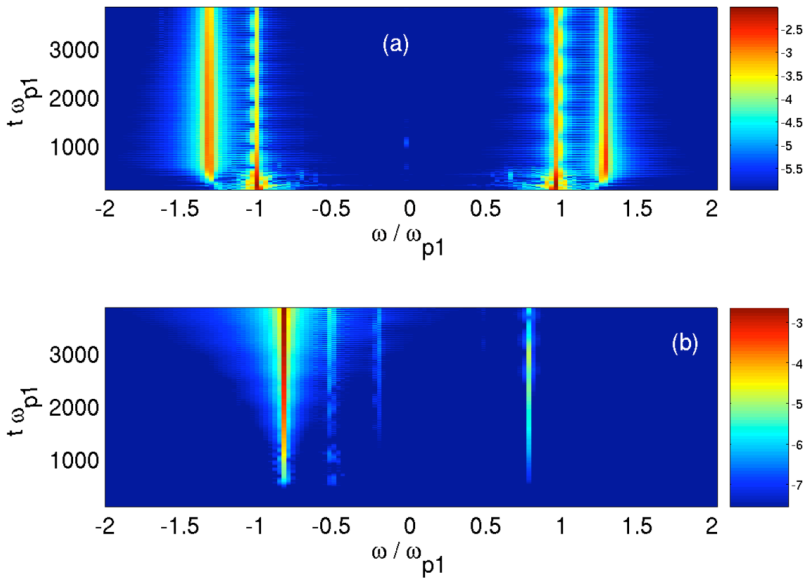

Figure 3.15: Reproduced from Ref.[77]. The ESW spectrum for a beam speed of $v_b = 0.8c$: **a.** shows the frequency power spectrum of $k_c = k_u$ and **b.** shows the frequency power spectrum of $k_c = k_u/2$ as a function of time. The colour scale shows logarithmic amplitude. The ESW driven by beam 1 with $v_b > 0$ corresponds to the wave with $\omega = \omega_{p,1}$ in **a**.

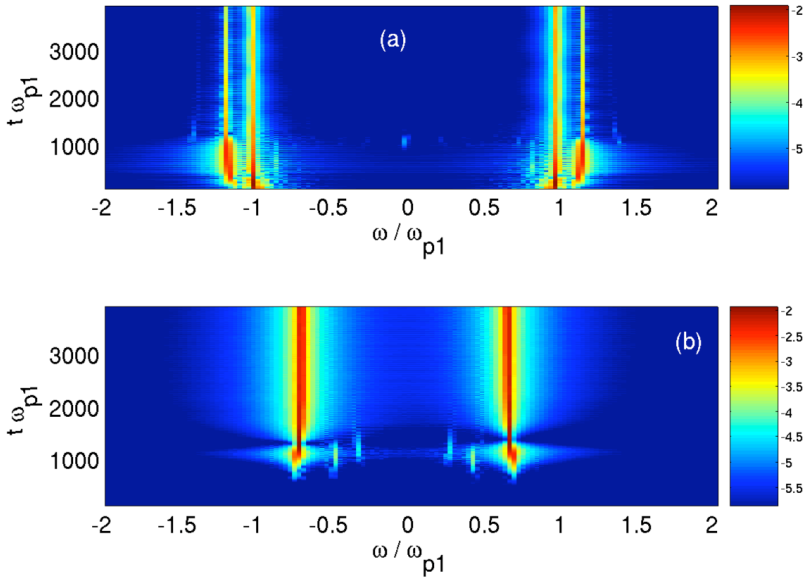

Figure 3.16: Reproduced from Ref.[77]. The ESW spectrum for a beam speed of $v_b = 0.9c$: **a.** shows the frequency power spectrum of $k_c = k_u$ and **b.** shows the frequency power spectrum of $k_c = k_u/2$ as a function of time. The colour scale shows logarithmic amplitude. The ESW driven by beam 1 with $v_b > 0$ corresponds to the wave with $\omega = \omega_{p,1}$ in **b**.

beam speed of $v_b = 0.9c$ in Fig. 3.16. The sideband modes at $k = k_u$ have a frequency modulus $\omega \approx 1.2\omega_{p,1}$ and phase speeds just above c. As for $v_b = 0.8c$ the sideband mode at $k = k_u/2$ has a frequency of $\omega \approx 0.8\omega_{p,1}$ and thus a superluminal phase speed. For both beam speeds $v_b = 0.8c$ and $v_b = 0.9c$ the sideband modes appear to have a superluminal phase speed and they can therefore not trap electrons. No secondary BGK modes should develop for these beam speeds.

3.3.8 Secondary Acceleration Mechanisms

In contrast to the PIC simulations in Ref.[67] the Vlasov simulation code shows the growth of modes resulting from a parametric coupling. These secondary waves grow to a large amplitude at which they can nonlinearly interact at the electrons. For the beam speeds up to $v_b = 0.4c$ the waves generated by the parametric interaction have been strongest. Here the turbulent wave fields interact with the waves with $\omega_{p,1}$ to produce

a wave with a higher frequency. Its larger phase speed can accelerate the trapped electrons to higher peak speeds. For a beam speed of $v_b = 0.6c$ the turbulent wave fields do not noticably interact with those at $\omega_{p,1}$. Instead a sideband unstable mode with $k = k_u$ develops. This mode has for $v_b \leq 0.6c$ a phase speed below c and the electron phase space distribution shows a fast BGK mode driven by it. For even higher v_b the superluminal phase speed of the sideband modes suppresses their interaction with the electrons.

The complex spectrum of secondary waves and their nonlinear interactions with the electrons has not been observed previously and suggests a strong dependence of the electron heating on v_b.

3.3.9 Peak Kinetic Energies

The peak relativistic kinetic energies $K = mc^2 e^{-1}(\gamma - 1)$ in eV the electrons reach are $K(v_b = 0.15c) = 1.3{\times}10^5$ eV, $K(v_b = 0.2c) = 2.2{\times}10^5$ eV, $K(v_b = 0.4c) = 5{\times}10^5$ eV, $K(v_b = 0.6c) = 3.2{\times}10^6$ eV, $K(v_b = 0.8c) = 3.6{\times}10^6$ eV and $K(v_b = 0.9c) = 8{\times}10^6$ eV. Note that all these peak electron energies are comparable or above the threshold energy of 10^5 eV: the injection energy for Fermi acceleration at perpendicular shocks [60].

3.4 Discussion

The observation of the emission of highly energetic cosmic ray particles by SNRs suggests the acceleration of particles from the thermal pool of the ISM plasma to highly relativistic energies by such objects. The acceleration site is apparently linked to the shock that develops as the supernova blast shell encounters the ambient plasma [78]. Such shocks are believed to accelerate electrons and ions to highly relativistic energies by means of Fermi acceleration [55, 56]. The Fermi acceleration of electrons is most efficient if the shock is quasi-perpendicular [59]. For such shocks, however, Fermi acceleration works only where there is a relativistically hot electron population prior to the shock encounter, since slow electrons could not repeatedly cross the shock and pick up energy. Since the

plasma, into which the SNR shock expands, has a thermal speed comparable to that of the ISM or the stellar wind of the progenitor star with temperatures of up to a few eV, taking the solar wind as reference, no mildly relativistic electrons may exist. A mechanism is required to pre-accelerate electrons. Electrons could be pre-accelerated from the initial thermal pool to mildly relativistic energies by their interaction with strong ESWs in the foreshock region [59] which, in turn, are driven by shock-reflected beams of ions.

This chapter has examined the growth, saturation and collapse of ESWs in a system dominated by the presence of two counter-propagating proton beams. The currents of both beams cancel, allowing the introduction of periodic boundary conditions. These initial conditions can be explained as follows: The upstream protons, that have initially been reflected by the shock, are rotated by the global magnetic field, that is oriented perpendicularly to the shock normal, and return as a second counter propagating proton beam, with a slightly increased temperature. The beam temperature should rise as it moves through the foreshock due to ion scattering by waves. The system modeled here is represents a small region ahead of a SNR shock. The magnetic field structure in this region is expected to be turbulent, with varying orientation. Globally, the magnetic field is orthogonal to the shock normal but over the simulation box the local field orientation is assumed to be such that the shock reflected proton beams move along the local magnetic field.

The system is unstable to the relativistic Buneman instability which saturates via the trapping of electrons to form BGK modes [79]. These trapped particle distributions are themselves unstable to the sideband instability and collapse after a period of stability. Since the model assumes that the protons move parallel to the local magnetic field magnetic field effects are neglected and the system is simulated using the electrostatic Vlasov Poisson model. Previous work [71, 66, 26, 65] has made extensive use of PIC codes. However, the problem benefits from the Eulerian Vlasov code's ability to resolve electron and ion phase space accurately, irrespective of the local particle density. This allows a secondary acceleration mechanism to be identified. Overall these results are in agreement with previous studies [66, 26] showing the lifetimes of the BGK modes to

be dependent on the initial beam velocity. As v_b is increased, there is a reduced ESW stability up to $v_b = 0.8c$ but with a significantly increased stability at the highest beam speed.

At low beam velocities ($v_b = 0.15c, 0.2c, 0.4c, 0.6c$) long wavelength, high phase-velocity modes are observed. These are able to trap electrons, producing a population with kinetic energies above the injection energy for Fermi acceleration, even at non-relativistic beam, and therefore shock, velocities. These secondary (i.e. not associated with the initial ESW saturation) trapped distributions appear to be the result of trapping in ESWs produced by parametric coupling between low frequency oscillations and plasma waves at $\omega_{p,1}$. Above $v_b = 0.6c$ the ESWs produced by this coupling have super-luminal phase velocities and are unable to trap electrons. As a result such BGK modes are not observed for the case of $v_b = 0.8c$, or $0.9c$. The simulation box, at $4\pi/k_u$ in length, can only accommodate one wavemode with wavenumber below that of the most unstable mode and this may have an influence on the appearance of this secondary acceleration.

Further work is required to examine how these parametric instabilities depend on a magnetic field and on the introduction of a second spatial dimension. Ideally, one would need to consider significantly larger simulation boxes, capable of resolving a broader spectrum below k_u. It may be the case that the availability of modes with $k < k_u$ will result in the partition of ESW energy across a greater region of the spectrum, perhaps inhibiting the trapping of electrons at high velocity. However, it may be the case that the observed coupling and resultant electron trapping is the first step of a cascade, capable of accelerating electrons to high energies for relatively modest shock velocities. This is because electrons can reach energies of 10^5 eV, even for v_b as low as 0.15c, or corresponding shock speeds of $7.5 \times 10^{-2}c$ which can be reached by the fastest SNR main shocks [80], allowing the electrons to undergo Fermi acceleration to highly relativistic speeds.

The numerical simulations in this chapter thus present strong evidence for the ability of ESWs and processes driven by electrostatic turbulence to accelerate electrons beyond the threshold energy at which they can undergo first order Fermi acceleration [59].

Chapter 4

The Electromagnetic Vlasov-Maxwell System

4.1 Outline

The interaction of electromagnetic radiation with a plasma is modelled kinetically via the direct solution of the Vlasov equation on a fixed Eulerian grid. This chapter details the model and numerical approach used. This model is tested against existing literature and extended for greater flexibility.

4.2 Solving the Vlasov-Maxwell system

4.2.1 The system

The interaction of EM radiation with a two component plasma of electrons and ions is treated in one dimension along the EM wave vector. The electric field $\mathbf{E}$ is given by

$$\mathbf{E} = -\nabla\phi - \partial_t \mathbf{A} \tag{4.1}$$

fixing the vector potential $\mathbf{A}$ in the transverse plain, $\mathbf{A} = \mathbf{A}_\perp$, the transverse and longitudinal components can be separated to give

$$\mathbf{E}_\perp = -\partial_t \mathbf{A}_\perp \tag{4.2}$$

$$E_x = -\nabla\phi = -\partial_x\phi. \tag{4.3}$$

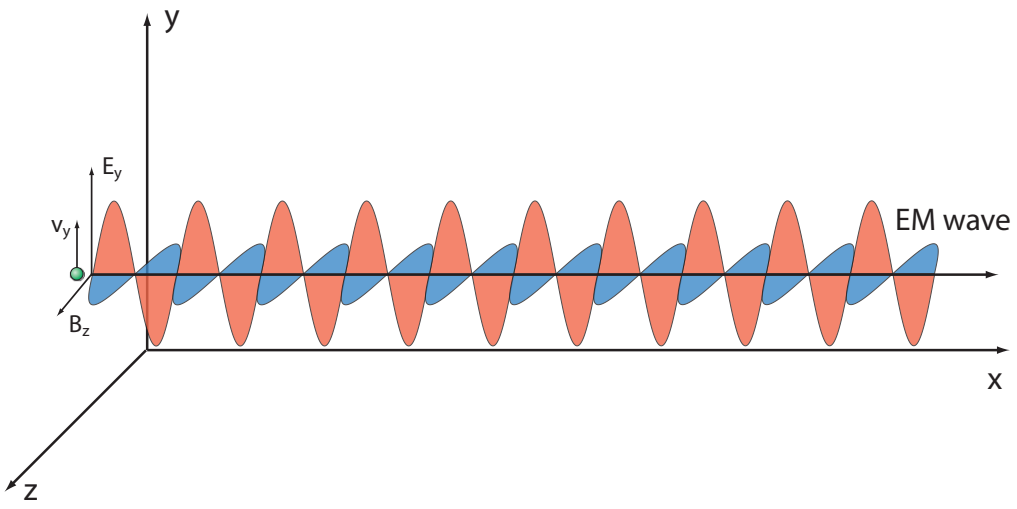

Figure 4.1: Geometry of the electromagnetic Vlasov Maxwell system with one spatial dimension. Distribution functions are evolved in (x, p_x) space. Transverse electric and magnetic fields are taken along the y and z axis respectively. Transverse motion of particles in the y direction are treated as fluid-like.

The magnetic field is given by the curl of the vector potential, $\mathbf{B} = \nabla \wedge \mathbf{A}$. For linearly polarised waves, the transverse electric and magnetic field can be oriented along the y and z axis respectively.

$$\mathbf{E}_\perp = \hat{\mathbf{e_y}} E_y \tag{4.4}$$

$$\mathbf{B}_\perp = \hat{\mathbf{e_z}} B_z \tag{4.5}$$

This arrangement is shown in Fig.4.1.

Relativistic Vlasov Equation

The Vlasov equation given in Eq.(1.45) is a non-relativistic treatment. As described in chapter 2, The Vlasov equation can be adapted to allow for relativistic dynamics, replacing the velocity, $\mathbf{v}$ with momentum $\mathbf{p} = m_e \gamma \mathbf{v}$, where $\gamma = (1 - v^2/c^2)^{-1/2} = (1 + |\mathbf{p}|^2/m_e^2 c^2)^{1/2}$ is the relativistic factor. This gives the relativistic Vlasov equation for electrons

$$\frac{\partial f_e}{\partial t} + \frac{\mathbf{p}}{\gamma m_e} \cdot \nabla_x f_e - e\left(\mathbf{E} + \mathbf{v} \wedge \mathbf{B}\right) \cdot \nabla_p f_e = 0 \tag{4.6}$$

and similarly for ions

$$\frac{\partial f_i}{\partial t} + \frac{\mathbf{p}}{\gamma m_i} \cdot \nabla_x f_i + e\left(\mathbf{E} + \mathbf{v} \wedge \mathbf{B}\right) \cdot \nabla_p f_i = 0 \tag{4.7}$$

The transverse velocities are assumed to be non-relativistic and their contribution to distribution function $f(x, \mathbf{p}, t)$ neglected, so that f is a function of p_x rather than $\mathbf{p}$. This is equivalent to taking the class of solutions with distribution functions given by $f(x, \mathbf{p}, t) = \delta(\mathbf{p}_\perp - e\mathbf{A}) f(x, p_x, t)$. The transverse motion of particles is essentially fluid like and, in the case of electrons, is given by

$$\mathbf{p}_\perp - e\mathbf{A} = 0 \tag{4.8}$$

Using Eqs.(4.2) and (4.4) gives $\partial_t p_y = -eE_y$ and taking $\mathbf{p}_\perp = m_e \mathbf{v}_\perp$, since $\gamma_\perp \approx 1$, gives $\frac{\partial v_{ey}}{\partial t} = -\frac{e}{m_e} E_y$. Maxwell's equations (Eqs.(1.27), (1.29) and (1.30)) in one dimension provide the self consistent electric and magnetic fields, closing the system

$$\frac{\partial E_x}{\partial x} = \frac{e}{\epsilon_0}\left(n_i - n_e\right) \tag{4.9}$$

$$\frac{\partial B_z}{\partial t} = -\frac{\partial E_y}{\partial x} \tag{4.10}$$

$$\frac{\partial E_y}{\partial t} = -c^2 \frac{\partial B_z}{\partial x} - \frac{1}{\epsilon_0} J_y \tag{4.11}$$

where the ion and electron densities are given by $n_{i,e} = \int f_{i,e} dv$, and $J_y = e\left(n_i v_{iy} - n_e v_{ey}\right)$ is the transverse current.

The transverse EM fields, E_y and B_z, are re-cast in terms of two new variables, $F^\pm$, the forwards and backwards propagating components of the TEM field[81, 82]. Defined as

$$F^\pm = \frac{1}{2}\left(E_y \pm c B_z\right) \tag{4.12}$$

Equations (4.10) and (4.11) then become

$$\frac{\partial F^\pm}{\partial t} \pm c \frac{\partial F^\pm}{\partial x} = -\frac{1}{2\epsilon_0} J_y \tag{4.13}$$

two advection equations which amount to solving Maxwells equations along their vacuum characteristics. Transverse fields can be recovered from $F^\pm$ since, $E_y = F^+ + F^-$ and $cB_z = F^+ - F^-$

The equations

The final system of equations is

$$\frac{\partial f_e}{\partial x} + \frac{p_x}{\gamma m_e}\frac{\partial f_e}{\partial t} - e\left(E_x + v_{ey}B_z\right)\frac{\partial f_e}{\partial p_x} = 0 \tag{4.14}$$

$$\frac{\partial f_i}{\partial x} + \frac{p_x}{\gamma m_i}\frac{\partial f_i}{\partial t} + e\left(E_x + v_{iy}B_z\right)\frac{\partial f_i}{\partial p_x} = 0 \tag{4.15}$$

$$\frac{\partial F^+}{\partial t} + c\frac{\partial F^+}{\partial x} = -\frac{1}{2\epsilon_0}J_y \tag{4.16}$$

$$\frac{\partial F^-}{\partial t} - c\frac{\partial F^-}{\partial x} = -\frac{1}{2\epsilon_0}J_y \tag{4.17}$$

$$\frac{\partial v_{ey}}{\partial t} = -\frac{e}{m_e}E_y \tag{4.18}$$

$$\frac{\partial v_{iy}}{\partial t} = \frac{e}{m_i}E_y \tag{4.19}$$

$$\tag{4.20}$$

with

$$n_e = \int f_e dv \tag{4.21}$$

$$n_i = \int f_i dv \tag{4.22}$$

$$J_y = e\left(n_i v_{iy} - n_e v_{ey}\right) \tag{4.23}$$

$$E_y = F^+ + F^- \tag{4.24}$$

$$B_z = \frac{1}{c}(F^+ - F^-). \tag{4.25}$$

4.2.2 Numerical Approach

Units and Normalisation

A system of normalised dimensionless units is adopted for the EM Vlasov code. These are given below where, for example, $\tilde{z}$ represents the dimensionless form of the variable z

$$\begin{aligned} \tilde{x} &= x\tfrac{\omega_{pe}}{c} & \tilde{t} &= t\omega_{pe} \\ \tilde{v} &= v\tfrac{1}{c} & \tilde{p} &= p\tfrac{1}{m_e c} \\ \tilde{E} &= E\tfrac{e}{\omega_{pe} c m_e} & \tilde{B} &= B\tfrac{e}{\omega_{pe} c^2 m_e} \\ \tilde{J} &= J n_0 e c \end{aligned} \tag{4.26}$$

The Time Stepping Algorithm

Due to the need to advance the transverse fields, the algorithm is more complex than for the electrostatic case, shown in Fig.2.1. Updates of the distribution functions proceed much as before, with an extra contribution to the velocity advection from the $\mathbf{v} \wedge \mathbf{B}$ term. The transverse fields are advanced along their vacuum characteristics using time and space centered values for the transverse current, J_y. To achieve this the transverse fields are updated alternately with the transverse velocities in a leapfrog regime, leaving them one half time-step out of phase with the other system variables, which must be taken account of in the initial conditions. An alternate to the leap-frog scheme would be a predictor corrector scheme. Such a scheme would allow all variables to be kept in sync but it would require additional versions of the distribution functions (the predictors) to be held in memory. The leapfrog scheme is scheme is shown in Fig.4.2.

Field and Distribution Function Updates

Distribution functions are evolved on a uniform fixed Eulerian grid in (x, p_x) space of size (N_x, N_p). Transverse fields and fluid variables are evolved on a one-dimensional grid of size N_x. Updates to E_x, f_e and f_i are carried out using the same approach as the electrostatic code. The transverse fields, $F^{\pm}$, can be advanced along their vacuum characteristics a distance $\Delta x = c\Delta t$ (or $\Delta\tilde{x} = \Delta\tilde{t}$, in normalised units) as follows. The transverse fields at x are advanced from $t - 0.5\Delta t$ to $t + 0.5\Delta t$ by advecting the field one full grid cell and adding the spatially averaged contribution of the transverse current

$$F^{\pm}(x, t + 0.5\Delta t) = F^{\pm}(x \mp \Delta x, t - 0.5\Delta t) - \frac{\Delta t}{2} J(x \mp 0.5\Delta x, t) \tag{4.27}$$

This approach has the advantage that the advection requires no interpolation and can be carried out efficiently using array shifts. However, the spatial and temporal resolution are unavoidably linked. The system is fixed at the CFL limit, and not below. Running within the CFL limit, that is $\Delta t = \alpha\Delta x$, where $\alpha < 1$ requires values for $F^{\pm}(x \mp \alpha\Delta x, t - 0.5\Delta t)$ and $J(x \pm 0.5\alpha\Delta x)$ which in turn requires reconstructions of $F^{\pm}$ and J from their gridded values. Using a piecewise parabolic reconstructions of the variables,

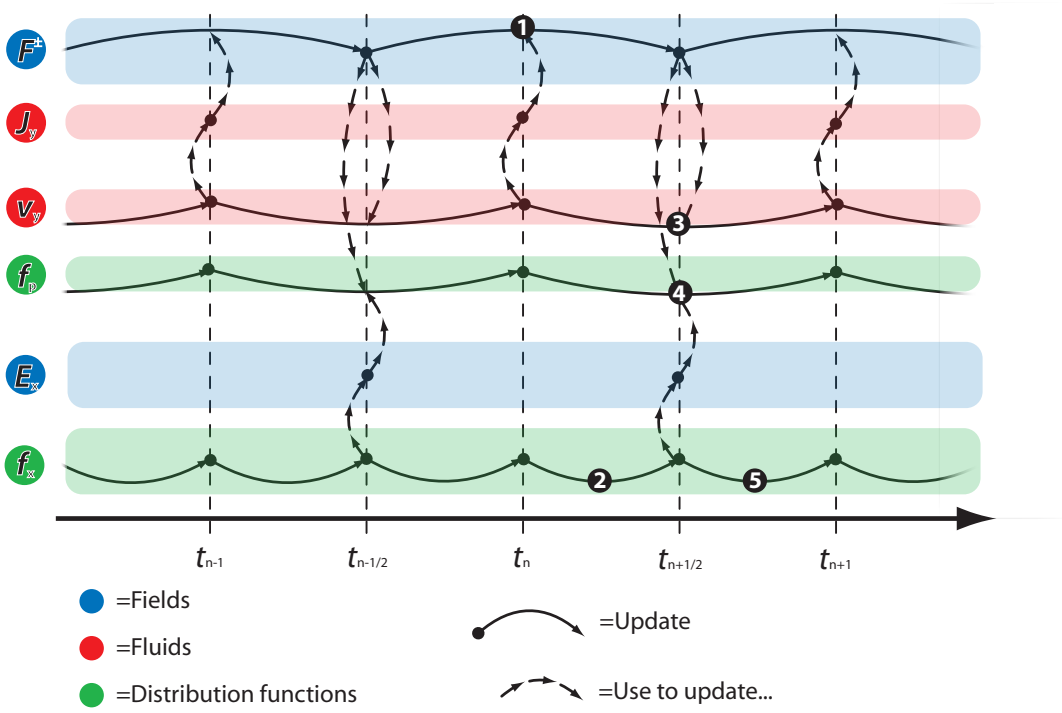

Figure 4.2: Time stepping algorithm for the electromagnetic Vlasov-Maxwell code. **1.** TEM fields $F^{\pm}$ are updated from $t_{n-1/2}$ to $t_{n+1/2}$ using the spatially averaged transverse current J_y calculated from the transverse velocities at t_n. **2.** Distribution functions are advected in x from t_n to $t_{n+1/2}$. **3.** Transverse velocities are updated from t_n to t_{n+1} using the E_y calculated in step 1. **4.** Distribution functions are advected in p_x using the time-centred transverse fields given by step 1 and the time centred transverse electric field calculated by solving Poisson's equation on the distribution functions after their advection in x (step 2). **5.** Finally, the distribution functions are advected the remaining half time step in x.

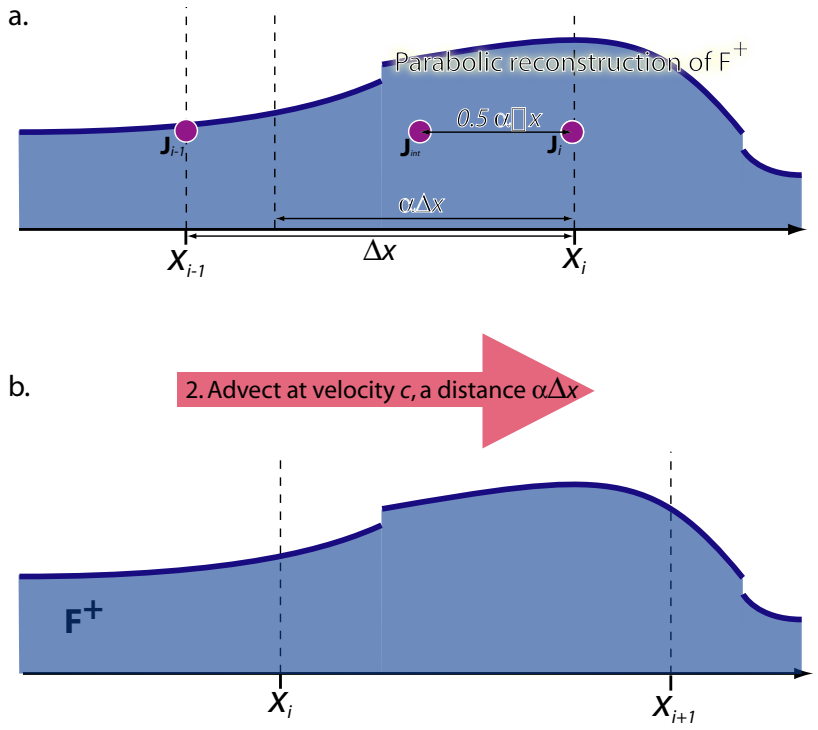

Figure 4.3: Advection of the transverse fields via PPM. The parabolic reconstruction of the transverse fields (**a.**) is used to advect $F^{\pm}$ a distance $\pm\alpha 0.5\Delta x$ (**b.**). The space and time centred transverse current, J_{int} is also given by a parabolic reconstruction.

see Figure 4.3, the transverse fields can be advanced thus

$$F^{\pm}(x, t + 0.5\Delta t) = F^{\pm}(x \mp \alpha\Delta x, t - 0.5\Delta t) - \frac{\Delta t}{2} J(x \mp 0.5\alpha\Delta x, t) \qquad (4.28)$$

The primary advantage of using a PPM advection scheme is that the core solver used to advance the distribution functions, whose reliability is already proven [38, 83], can be employed for the transverse field updates. Also, PPM is an explicit scheme and well suited to domain decomposition, facilitating the parallelisation of the scheme (as described later). The update of the longitudinal field remains the same as the electrostatic Vlasov solver. The densities, given by integrating the distribution functions in p_x are used to solve Poisson's equation spectrally. This method is only applicable for a periodic

system, the non-periodic case is described in section 4.4.

4.3 Testing

Results from the code are compared with existing literature.

4.3.1 Test Problem

Stimulated Raman Scattering provides an ideal test problem for the code.

Initial Conditions

The system is initialised with a TEM parent wave and a density perturbation to seed the growth of the Langmuir daughter wave. The system is periodic and the TEM parent wave is not externally driven. System length $\tilde{L}_x = 8.92$, equivalent to $\approx 115.5\lambda_D$ and the electron thermal velocity $v_{Te} = 0.08c \Rightarrow \tilde{T}_e = 0.0064$, equivalent to 3.2KeV. The density n_0 corresponds to $0.08n_c$. The wave numbers of the parent, $E1$, and seed, L waves are given by

$$\tilde{k}_{E1} = 3 \times \frac{2\pi}{\tilde{L}_x} \tag{4.29}$$

$$\tilde{k}_{L} = 4 \times \frac{2\pi}{\tilde{L}_x} \tag{4.30}$$

The parent TEM wave has amplitude $\tilde{E}_{E1} = 0.28$, the density perturbation at $k = k_L$ has amplitude $\delta n = 0.01$. The three wave system is completed by a backscattered TEM wave, $E2$ at

$$\tilde{k}_{E2} = -1 \times \frac{2\pi}{\tilde{L}_x} \tag{4.31}$$

which is initialised with zero amplitude.

For these wavenumbers the corresponding frequencies are

$$\tilde{\omega}_{E1} = 2.338 \tag{4.32}$$

$$\tilde{\omega}_{L} = 1.073 \tag{4.33}$$

$$\tilde{\omega}_{E2} = 1.223 \tag{4.34}$$

giving a small frequency mismatch $\delta\tilde{\omega} = \tilde{\omega}_{E1} - \tilde{\omega}_L - \tilde{\omega}_{E2} = 0.041$.

4.3.2 Manley-Rowe Relations

The Manley-Rowe relations are a statement of energy conservation between parametrically coupled waves. They serve as a useful diagnostic, particularly during the early stages of instabilities such as SRS. They are derived from a simple Zakharov-like treatment of the plasma and do not take account of secondary instabilities or kinetic effects such as detuning. Considering only the slowly varying amplitude of three coupled waves, a_i, $i = 1, 2, 3$.

$$\begin{aligned} \frac{da_1}{dt} &= -\beta\omega_1 a_2 a_3 \\ \frac{da_2}{dt} &= \beta\omega_2 a_1 a_3^* \\ \frac{da_3}{dt} &= \beta\omega_3 a_1 a_2^* \end{aligned} \tag{4.35}$$

Where β is the coupling coefichent. Since $\omega_1 = \omega_2 + \omega_3$, Eq.(4.35) gives

$$\frac{d}{dt}\left(|a_1|^2 + |a_2|^2 + |a_3|^2\right) = 0 \tag{4.36}$$

With the appropriate rescaling of the wave amplitudes, $|a_i|^2$ represents the energy density of the wave, thus Eq.(4.36) is a statement of the conservation of energy. For the case of SRS, a_1 is the incident EMW, a_2 the reflected EMW and a_3 the Langmuir wave. Each a_i is defined as follows

$$\begin{aligned} a_{1,2} &= \frac{1}{2}\epsilon_0 |E_{1,2}|^2 \\ a_3 &= \frac{1}{2}\epsilon_0 |E_3|^2 \frac{\omega_3^2}{\omega_{pe}^2} \end{aligned} \tag{4.37}$$

It follows from Eq.(4.36) that

$$-\frac{1}{\omega_1}\frac{d}{dt}|a_1|^2 = \frac{1}{\omega_2}\frac{d}{dt}|a_2|^2 = \frac{1}{\omega_3}\frac{d}{dt}|a_3|^2 \tag{4.38}$$

These are the Manley-Rowe relations, the quantity $|a_i|^2/\omega_i$ is refered to as the wave action density. In the case of SRS the parent wave, a_1 is of much greater amplitude, a_2 and a_3 will grow at its expense. The growth of the daughter waves is bounded, eventually energy will be transfered back from a_2 and a_3 into a_1 and the system will begin to oscillate about an equilibrium energy distribution.

4.3.3 Results

Figure 4.4 summarises the results from the SRS test. Figure 4.5 shows key results from the literature [81] for the same test problem. The amplitudes of the incident, reflected and Langmuir modes show the reflected EMW growing at the expense of the pump wave. As discussed earlier, this is the result of scattering from the Langmuir wave. The process creates a feed back loop and is unstable with the two daughter waves initially growing exponentially. The Manley-Rowe relations (Eq.(4.38)) are obeyed through much of the simulation time. Qualitative predictions made above by interpretation of the relations is also borne out by the resullts, clearly visible is the transfer of energy from the initially larger amplitude parent wave to the daughters. This growth is certainly bounded and the system settles into an oscillatory phase after $\tilde{t} \approx 250$.

There are two instances when the Manley-Rowe relations are clearly inaccurate. Firstly, in the interval $\tilde{t} \approx 50, 80$ the Langmuir mode at $\tilde{k}_L = 4 \times \frac{2\pi}{\tilde{L}_x}$ appears to be receiving less energy than Eqs.(4.36) would suggest. This is due to the acceleration and trapping of electrons in the wave, which is visible in the electron distribution function shown in Fig.4.6b. These electrons have taken energy from the wave but are not accounted for in the Manley-Rowe relations which are inherently fluid-like. This is an example of a kinetic phenomena which a fluid-like model cannot take into account *a priori*. Secondly, at $\tilde{t} \approx 160$ there is a transient deviation for the relations. This can be attributed to the excitation of a lower wave number Langmuir wave at $\tilde{k}_{L2} = 2 \times \frac{2\pi}{\tilde{L}_x}$. This wave is a result of stimulated forward Raman scattering of the parent wave, it is the recipient of some of the incident energy - as a result breaking the three-wave assumption used in the derivation of Eqs.(4.36). This forward scattering is not present immediately since the mode is not seeded initially and the frequency mismatch is greater ($\approx 0.096\omega_{pe}$). The effect of this long wavelength mode on the distribution function can be seen in Fig.4.6c, the trapped distributions from the two Langmuir waves merge and the system evolves towards a homogeneous plateaux extending to $\tilde{p} \approx 1.2$. This demonstrates the potential of SRS to produce hot electrons which pre-heat the target core, reducing the efficiency of compression.

The results outlined above are in close agreement with the those in Ref.[81]. This

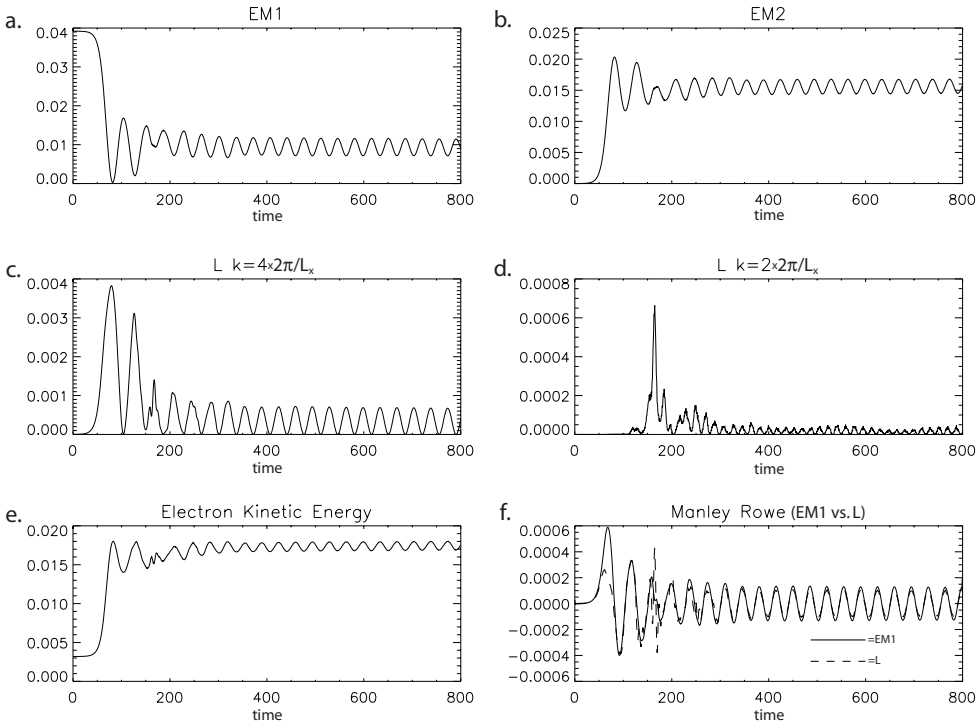

Figure 4.4: Amplitudes of the; **a.** parent EM; **b.** daughter EM wave; **c.** daughter Langmuir wave and **d.** daughter Langmuir wave from forward scattering. Together with; **e.** total electron kinetic energy and **f.** action conservation between parent EM and Langmuir daughter waves. These plots demonstrate the scattering of incident EM radiation by a Langmuir wave - Stimulated Raman Scattering (SRS). The Daughter EM and Langmuir waves grow at the expense of the parent wave until the system saturates and begins to oscillate about an equilibrium energy partition. Action conservation between the parent EM an daughter Langmuir wave holds for much of the simulation time. Significant deviations are the result of electron trapping and the growth of a second Langmuir wave, again at the expense of the parent EM wave.

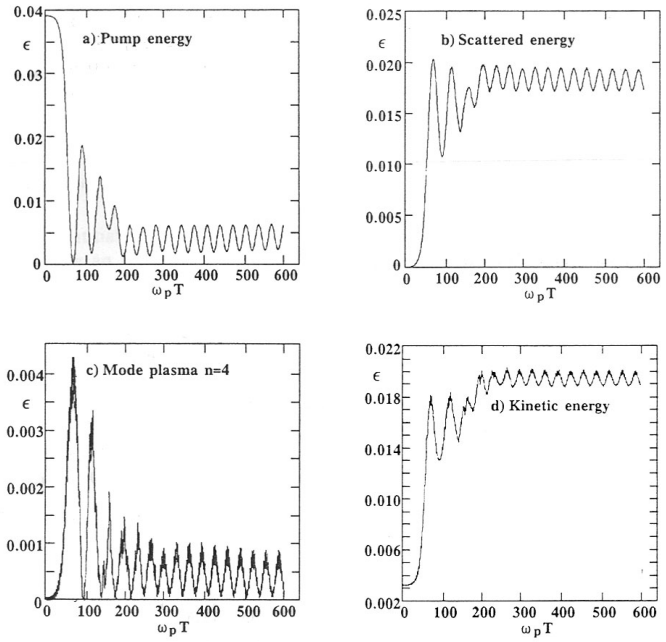

Figure 4.5: Reproduced from Ref.[81]. These results are in close agreement with those outlined in Fig.4.4.

problem demonstrates some of the key physics issues in LPI (such as particle trapping and hot electron production) and highlights the strengths of the Eulerian Vlasov solver - in particular the ability to resolve the particle phase space to high resolution even in regions of low particle density, such as the hot electron plateaux.

4.4 Extension

The problems considered above were for periodic systems only a few wavelengths of incident light in length. The code is extended to problems of greater physical extent necessitating more grid points. To achieve this without rendering the simulations too time consuming the code is adapted to run on multi-processor computer systems. Furthermore, examples given so far are un-driven. From $\tilde{t} = 0$ no additional energy is provided to the incident wave. The evolution of the system broadly obeys the predictions of the Manley-Rowe equations, eventually oscillating about an equilibrium energy partition. Considering a small region in a realistic laser-plasma system, the incident beam will be driven at the edge of the system with an externally imposed amplitude. The development of a parallel, non-periodic, driven version of the code is outlined below.

4.4.1 Parallel Implementation

The code is parallelised in the x-direction using the Message Passing Interface (MPI) libraries. The simulation box is decomposed into n separate domains, as shown in Fig.4.7, the Vlasov-Maxwell equations are then solved in each domain by a separate processor. Each time step, the processors update their ghost cells with values from their neighbours - in this way the system continues to function as a cohesive whole, despite being distributed across several processors.

The update of the longitudinal electric field E_x is not a time limiting step, and so is not parallelised. As shown in Fig.4.8, the processors share their local density information until each has the density for every point in the system. The field can then be calculated as before for the complete system on all processors simultaneously with each processor retaining the portion of E_x which applies to its domain.

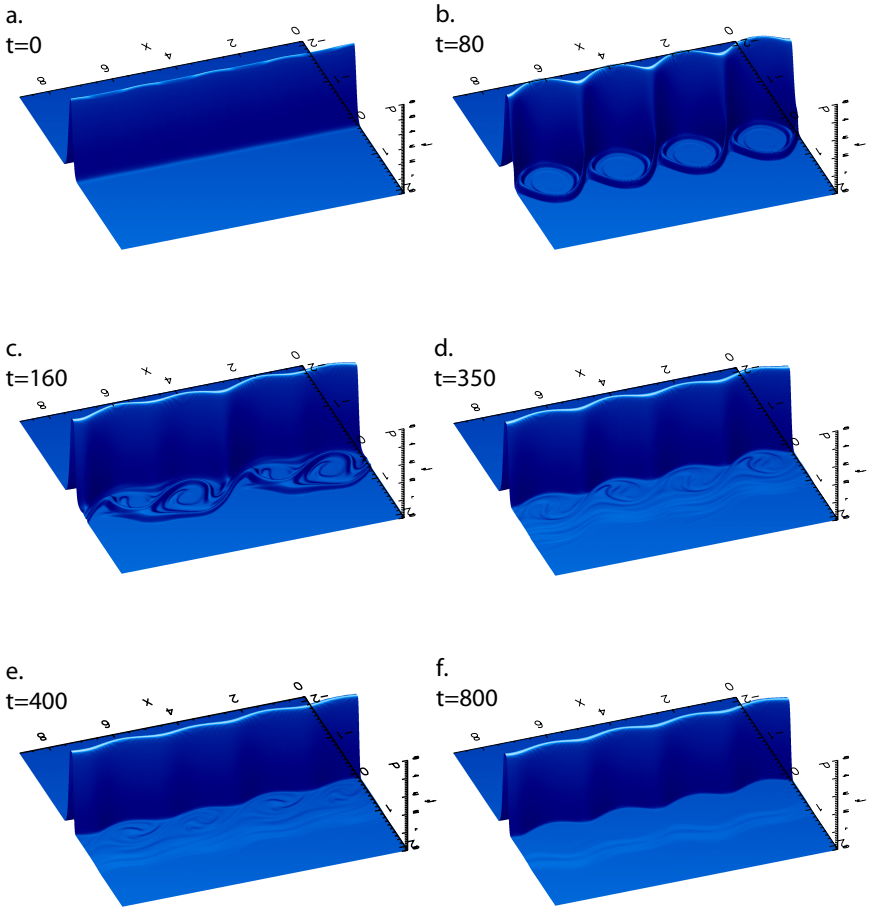

Figure 4.6: Surface plots of the electron distribution function for the SRS test problem at various times. Key features are the trapping of electrons in the Langmuir wave, producing the phase space holes visible at $\tilde{t} = 80$, and the eventual production of a plateaux of hot electrons.

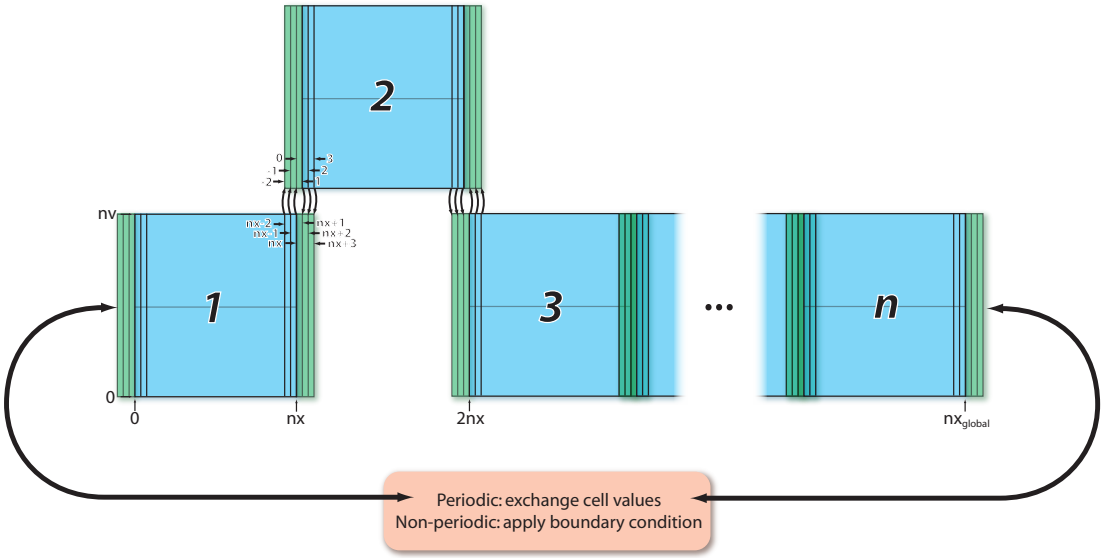

Figure 4.7: The system domain, with nx_{global} grid cells is divided up into n separate processes, each with $nx = nx_{\mathrm{global}}/n$ grid cells and six ghost cells. Ghost cells are copies of grid values from neighboring processes, they are used to calculate variables at the boundaries between processes. The ghost cells are updated each timestep. The ghost cells for the first and last processes in the system may be subject to different boundary conditions for the case of a non-periodic simulation box.

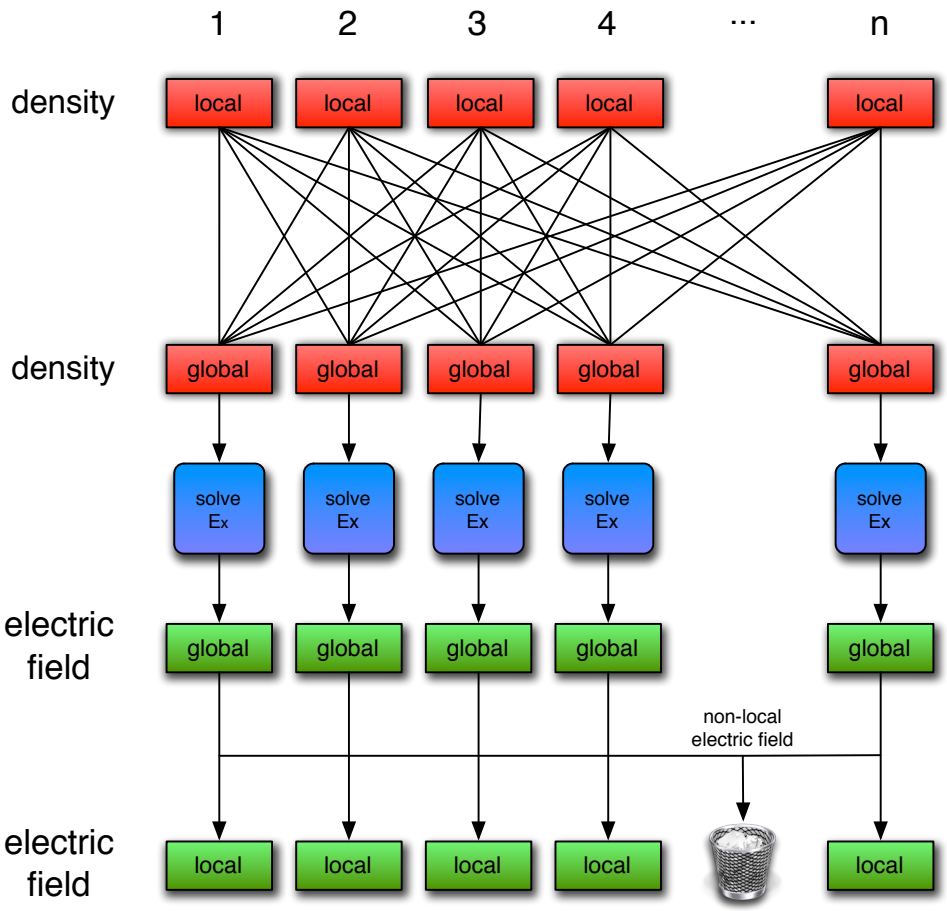

Figure 4.8: Schematic of the process of solving Poisson's equation in the parallel code. All processes share density information until each has the complete density profile of the system. They then each solve Poisson's equation for the whole system to give E_x, retaining only the portion of the global electric field which covers their domain.

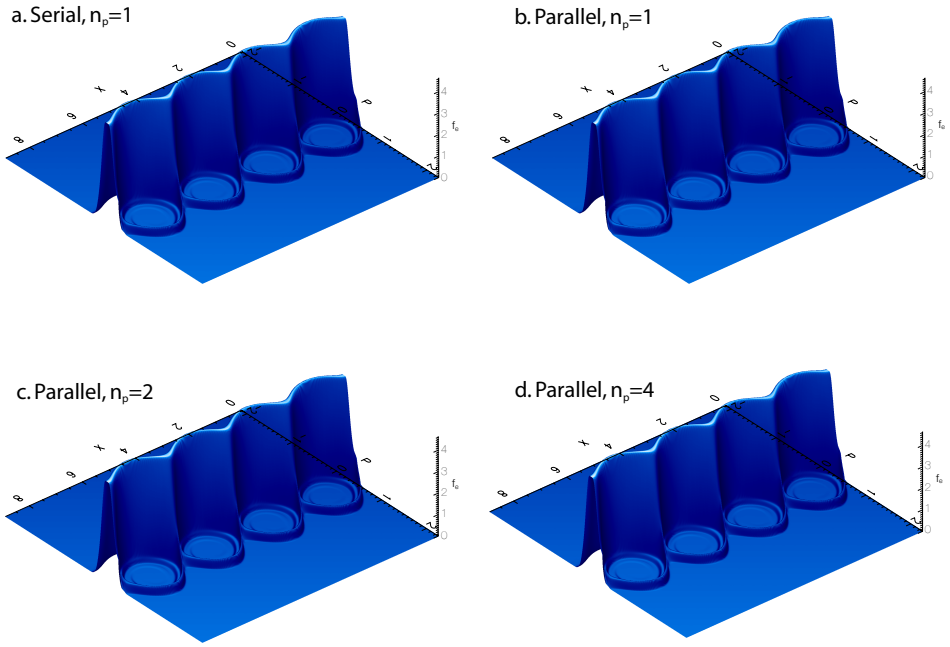

Figure 4.9: Serial and parallel codes produce identical results, to machine precision. Shown here are surface plots of the electron distribution function from the test problem outlined in section 4.3 at $\tilde{t} = 80$ for serial and parallel (with one, two and four processors) implementations.

Testing the Parallel Implementation

The SRS problem detailed in section 4.3 is used to test the parallel implementation. Results for one, two and four processors using the parallel code are compared with those from the original implementation and found to be identical, to machine precision. These results are sumerised in Fig.4.9.

4.4.2 Non-Periodic Systems

For a non-periodic systems, new boundary conditions for the system edges must be implemented and the electrostatic field solver replaced.

Taking Poisson's equation for the electrostatic potential $\tilde{\phi}_x$, in normalised units

$$\frac{d^2\tilde{\phi}_x}{dx^2} = (n_i - n_e) \tag{4.39}$$

approximate the second derivative on the numerical grid as

$$\left(\frac{d^2\tilde{\phi}_x}{dx^2}\right)^i \approx \frac{\tilde{\phi}_x^{i-1} - 2\tilde{\phi}_x^i + \tilde{\phi}_x^{i+1}}{\Delta\tilde{x}^2} \tag{4.40}$$

where $\tilde{\phi}_x^i$ is the value of $\tilde{\phi}_x$ on the ith grid point. Equation (4.39) then becomes

$$\tilde{\phi}_x^{i-1} - 2\tilde{\phi}_x^i + \tilde{\phi}_x^{i+1} = (n_i - n_e)\Delta\tilde{x}^2 \tag{4.41}$$

Solving Eq.(4.41) for the complete system is the equivalent of solving the matrix equation

$$\underline{\tilde{\phi}}_x = \underline{\underline{M}}^{-1}\underline{\rho} \tag{4.42}$$

where $\rho^i = (n_i^i - n_e^i)\Delta\tilde{x}^2$. The form of the matrix $\underline{\underline{M}}$ depends on the system boundary conditions. For periodic boundaries, $\underline{\underline{M}}$ is given by

$$\underline{\underline{M}} = \begin{pmatrix} -2 & 1 & 0 & & 0 & 0 & 1 \\ 1 & -2 & 1 & \cdots & 0 & 0 & 0 \\ 0 & 1 & -2 & & 0 & 0 & 0 \\ & \vdots & & \ddots & & \vdots & \\ 0 & 0 & 0 & & 1 & -2 & 1 \\ 1 & 0 & 0 & \cdots & 0 & 1 & -2 \end{pmatrix} \tag{4.43}$$

and Eq.(4.42) is solved using the Thomas algorithm[84].

With open boundaries, charge is free to leave the system. If this charge is not accounted for in the solution of the electrostatic field it can result in the creation of a D.C. field. The flux of charge through each system boundary is recorded to give the total charge in the system Q_S, the total charge outside the left-hand boundary Q_L and the total charge outside the right-hand boundary Q_R. Initially, $Q_S = Q_T$, where Q_T is the total charge. It follows that $Q_S + Q_L + Q_R = Q_T$ throughout. For neutral systems, $Q_T = 0$. The external charge is included in the solution of Eq.(4.42) as charge residing in ghost cells outside the system domain. Thus $\rho^0 = Q_L$ and $\rho^{nx+1} = Q_R$.

The potential external to the system is assumed to be uniform, such that $\tilde{\phi}_x^{-1} = \tilde{\phi}_x^0$ and $\tilde{\phi}_x^{nx+2} = \tilde{\phi}_x^{nx+1}$. Without loss of generality take $\tilde{\phi}_x^{-1} = 0$. It follows that

$$\underline{\underline{M}} = \begin{pmatrix} -2 & 1 & 0 & & 0 & 0 & 0 \\ 1 & -2 & 1 & \cdots & 0 & 0 & 0 \\ 0 & 1 & -2 & & 0 & 0 & 0 \\ & \vdots & & \ddots & & \vdots & \\ 0 & 0 & 0 & & 1 & -2 & 1 \\ 0 & 0 & 0 & \cdots & 0 & 1 & -1 \end{pmatrix} \tag{4.44}$$

The potential from grid cell 0 to grid cell $nx + 1$ (the simulation box plus two ghost cells) is given by $\phi_x^{(0,nx+1)}$ calculated by solving Eq.(4.42) using the form of $\underline{\underline{M}}$ given above together with $\rho^{(0,nx+1)}$, calculated from $n_{e,i}^{(1,nx)}$ and $Q_{L,R}$. The matrix equation given in Eq.(4.42) can easily be solved using an implicit tridiagonal matrix inversion algorithm[84]. This scheme still requires all the processors to solve ϕ_x for the complete system, as described in Fig.4.8. The electric field E_x can then be calculated from the second order accurate gradient of ϕ_x.

Boundary conditions for the distribution functions are chosen so that $\frac{\partial f_{e,i}}{\partial x} = 0$ at the system boundaries.

Chapter 5

Kinetic Scattering Effects in LPI

This chapter is an expansion of work submitted for publication [N. J. Sircombe, T. D. Arber and R. O. Dendy *Kinetic effects in Laser-Plasma coupling: Vlasov theory and computations*, Submitted to Plasma Physics and Controlled Fusion].

5.1 Introduction

Recent single hot-spot experiments on the Trident laser system [24, 25] identified backscatter resembling stimulated Raman scattering (SRS) but, importantly, from an electron plasma mode whose frequency is significantly below the plasma frequency. This mode was identified as the electron acoustic wave (EAW), an undamped mode supported by the trapping of electrons. The theoretical background to the EAW is described and the mode is then simulated, using the EM Vlasov code described in chapter 4, to demonstrate its undamped nature. The implications for laser plasma interactions are examined including the Langmuir decay instability (LDI) and stimulated electron acoustic scattering (SEAS).

5.2 The Electron Acoustic Wave

The possible existence of plasma waves at frequencies significantly below the electron plasma frequency was first identified by [85], although it was expected that Landau

damping in this regime would prohibit their formation. Later work [19, 20, 21, 22] showed that EAWs can indeed exist, supported by a population of trapped electrons. The conventional derivation of the plasma dispersion relations based on the two-fluid treatment described in section 1.4.1, yields high frequency Langmuir waves and low frequency ion-acoustic waves. The kinetic treatment described in section 1.4.2 shows these modes to be Landau damped provided that $\partial_v f|_{v_p} < 0$, where f is the particle distribution function and v_p the phase velocity of the wave. However if $\partial_v f|_{v_p} = 0$ then the wave may be undamped as is the case for the EAW.

The Plasma Dispersion Function

In order to construct a dispersion relation for the EAW, first consider the Landau dispersion relation (Eq.(1.59) for Maxwellian distribution with characteristic velocity v_{Te}:

$$\epsilon(\omega, k) = 1 - \frac{1}{k^2\lambda_d^2}\frac{1}{v_{Te}\sqrt{2\pi}}\int_{-\infty}^{\infty}\frac{v}{v-\omega/k}\exp\left(-\frac{v^2}{\sqrt{2}v_{Te}^2}\right)dv \tag{5.1}$$

This can be written in terms of the plasma dispersion function

$$Z(\zeta) = \frac{1}{\sqrt{\pi}}\int_{-\infty}^{\infty}\frac{1}{t-\zeta}\exp\left(-t^2\right)dt \tag{5.2}$$

Differentiating Eq.(5.2) with respect to ζ and integrating by parts with respect to t gives

$$Z'(\zeta) = -\frac{1}{\sqrt{\pi}}\int_{-\infty}^{\infty}\frac{2t}{t-\zeta}\exp\left(-t^2\right)dt = -2(1+\zeta Z). \tag{5.3}$$

Taking $t = v/(\sqrt{2}v_{Te})$ and $\zeta = \omega/(\sqrt{2}v_{Te}k)$ together with Eq.(5.3), Eq.(5.1) becomes

$$\epsilon(\omega, k) = 1 + \frac{1}{k^2\lambda_d^2}(1+\zeta Z(\zeta)) \tag{5.4}$$

Let ζ tend to zero from the upper half of the complex plane to give

$$Z(0) = \frac{1}{\sqrt{\pi}}P\int_{-\infty}^{\infty}\frac{1}{t}\exp\left(-t^2\right)dt + i\sqrt{\pi} = i\sqrt{\pi} \tag{5.5}$$

where the principal part of the integral is zero, since the integrand is an odd function. Equation (5.3) gives the linear differential equation $Z' = -2(1+\zeta Z)$ which can be solved using the boundary condition given in Eq.(5.5) together with an integrating factor of $\exp\left(\zeta^2\right)$ to give

$$Z(\zeta) = \exp\left(-\zeta^2\right)\left(i\sqrt{\pi} - 2\int_0^{\zeta}\exp\left(z^2\right)dz\right) \tag{5.6}$$

The EAW Dispersion Relation

This approach can be extended to case of a Maxwellian distribution with a flattened region at $v = v_p$ in the limit where the width of the flattened region, in velocity space, tends to zero while $\partial_v f|_{v_p} = 0$. This is defined by

$$\frac{\partial f}{\partial v} = \begin{cases} \frac{1}{\sqrt{2\pi}} \exp\left(\frac{-v^2}{\sqrt{2}v_{Te}}\right) & v \neq v_p \\ 0 & v = v_p \end{cases} \tag{5.7}$$

Similarly defining Z_{new} as

$$Z_{new}(\zeta) = \begin{cases} Z(\zeta) & \zeta \neq \frac{v_p}{\sqrt{2}v_{Te}} \\ 0 & \zeta = \frac{v_p}{\sqrt{2}v_{Te}} \end{cases} \tag{5.8}$$

gives the dispersion relation for the EAW as

$$\epsilon(\omega, k) = 1 + \frac{1}{k^2\lambda_d^2}(1 + \zeta Z_{new}(\zeta)). \tag{5.9}$$

However, by construction, for $\zeta = 0$, Z_{new} has no residue about the pole $t = 0$. Hence $Z_{new}(0) = 0$ and Eq.(5.6) becomes

$$Z_{new}(\zeta) = -2\exp(-\zeta^2)\int_0^{\zeta} \exp(z^2)dz = -2\mathrm{Daw}(z) \tag{5.10}$$

Finally, the dispersion relation for EAWs in the linear limit is given by

$$k^2\lambda_d^2 + 1 - 2\frac{\omega}{\sqrt{2}k}\mathrm{Daw}\left(\frac{\omega}{\sqrt{2}k}\right) = 0 \tag{5.11}$$

$$\mathrm{Daw}(z) = \exp(-z^2)\int_0^z \exp(t^2)dt \tag{5.12}$$

where Eq.(5.12) is the Dawson integral. Evaluating Eq.(5.11) numerically [84] gives the dispersion relation for undamped plasma waves in the limit of vanishing amplitude. The dispersion curve, labeled $\Delta v = 0$, is shown in Fig.5.1, where there are two distinct branches. The upper branch corresponds to an undamped form of the Langmuir wave and the lower branch, with $\omega < \omega_{pe}$, corresponds to the electron acoustic wave.

Finite Amplitude Case

Similar analysis can be carried out for distribution functions that have a finite flattened region of width Δv proportional to the wave amplitude, defined as

$$f = f_0 + f_1 \tag{5.13}$$

where f_0 represents a Maxwellian distribution, and flattening at $v = v_p$ is provided by

$$f_1(v) = \partial_v f_0|_{v_p}(v - v_p) \exp\left(\frac{-(v - v_p)^2}{\Delta v^2}\right). \tag{5.14}$$

where Δv is the width of the flattened region. With this f, Eq.(1.59) becomes

$$\begin{aligned} \epsilon(\omega, k) &= 1 + \frac{1}{k^2\lambda_d^2}(1 + \zeta Z(\zeta)) \\ &+ \frac{v_p \exp(-v_p^2)}{k^2\lambda_d^2}\left(2u + (2u^2 - 1)Z(u)\right) \end{aligned} \tag{5.15}$$

where $u = (\zeta - v_p)/\Delta v$. Note that as $\Delta v \to 0$ the dispersion relation given in Eq.(5.11) is recovered. Equation (5.15) gives a family of dispersion curves inside the ideal, infinitesimal amplitude case, as shown in Fig. 5.1.

5.3 Physical Interpretation

The EAW appears, at first, to be unphysical. In particular its low frequency is a characteristic not expected of electron plasma waves supported by distribution functions arbitrarily close to Maxwellian, in which ion dynamics play no role. Some physical understanding, for the case of small k, can be gained by considering a locally flattened distribution to be a superposition of a background Maxwellian population and a smaller drifting population, as shown in Fig.5.2

In the frame of reference of the background population, oscillations at the electron plasma frequency in the second population will be Doppler shifted such that

$$\omega = \omega' + kv \tag{5.16}$$

where

$$\omega' = \sqrt{\frac{e^2 n_2}{\epsilon_0 m_e}} \tag{5.17}$$

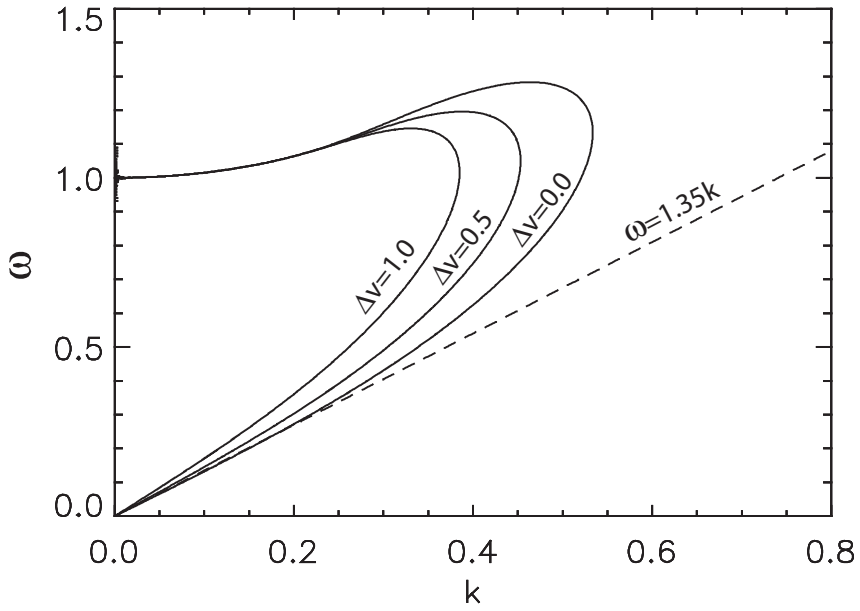

Figure 5.1: Dispersion relations for undamped BGK-like plasma modes in the linear limit (where the width Δv of the flattened region, in units of thermal velocity, tends to zero) and for two non-linear cases ($\Delta v = 0.5, 1.0$). Wavenumbers are normalised to λ_D^{-1} and frequencies to ω_{pe}. The lower branch represents the electron acoustic wave, which for low k follows $\omega \simeq 1.35k$. The upper branch represents an undamped form of the Langmuir mode.

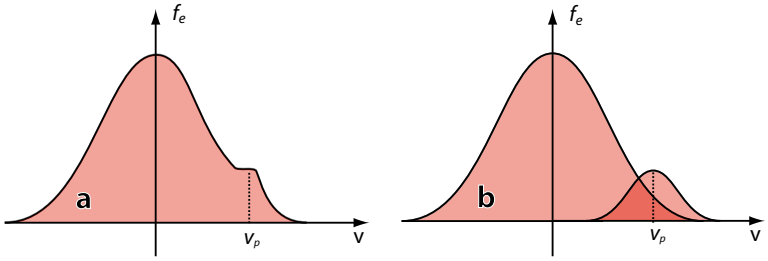

Figure 5.2: The distribution (**a**) which exhibits local flattening at v_p,can be considered as a background Maxwellian plus a smaller drifting electron distribution centred at v_p (**b**). The Doppler shifted frequency of plasma oscillations in the drifting electron distribution governs the EAW dispersion relation in the limit of small density.

is the electron plasma frequency for the second population, whose density is n_2. In the limit where the density of this second population tends to zero, we recover $\omega \sim vk$. This dispersion relation is linear in k for small k, and implies a frequency below the plasma frequency. While this interpretation does not give the value for the phase velocity of the EAW in the linear limit ($v_p \approx 1.35 v_{Te}$) it is helpful in understanding the origin of low frequency modes described by Eq.(5.11).

5.4 Simulating an EAW

A full treatment of the EAW requires a kinetic description of the plasma. This section outlines the development of initial conditions for, and the simulation of, a travelling EAW. The model used is the one-dimensional Vlasov-Poisson system with mobile electrons, immobile protons and no magnetic field. This is solved with the electrostatic Vlasov-Poisson code introduced previously and used extensively in chapters 2 and 3. This fully nonlinear self-consistent system is governed by the Vlasov equation for the electron distribution function f_e given in Eq.(2.4) and Poisson's equation for the electric field, Eq.(2.3).

As an initial condition, consider an unperturbed distribution function flattened at a phase velocity v_p chosen from the EAW branch of the dispersion relation. In this case, unperturbed distribution function is given by Eqs.(5.13) and (5.14). In order to create a traveling wave the distribution function must be perturbed. Adopting a similar approach to that used in section 1.4.4, linearise the Vlasov equation and consider small perturbations f_p to an equilibrium, f_u, given by a Maxwellian, flattened at $v = v_p$, as in Eq.(5.13). This gives

$$f_p = \frac{e}{m_e} \frac{1}{\omega - kv} E \partial_v f_u \tag{5.18}$$

Writing $\omega = \omega_r + i\gamma$, where both ω_r and γ are real, and prescribing an electric field of the form $E = E_0 \exp(ikx - i\omega_r t)$ gives

$$\mathrm{Re}(f_p) = \frac{-eE_0}{m(\omega - kv)} \left(\sin(kx - \omega_r t) - \frac{\gamma}{\omega_r - kv} \cos(kx - \omega_r t) \right) \times \partial_v f_u \tag{5.19}$$

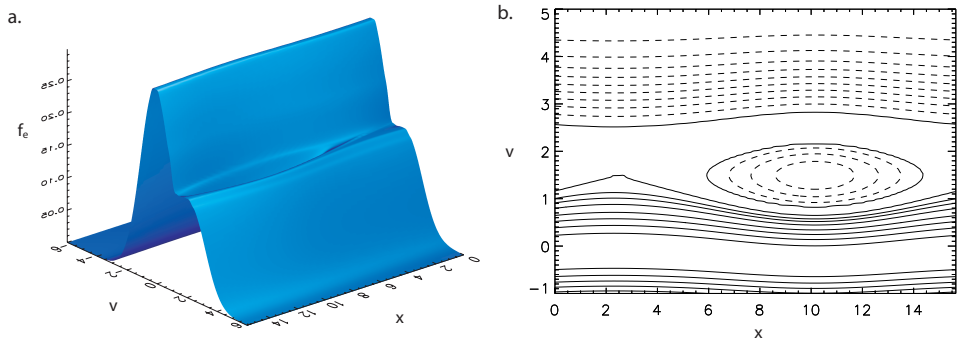

Figure 5.3: **a.** Surface plot of the electron distribution function for a large amplitude EAW ($\delta n = 0.1 n_e, \omega = 0.6\omega_{pe}, k = 0.4\lambda_D^{-1}$) at time $t = 10^3\omega_{pe}^{-1}$, simulated using the Vlasov-Possion code. **b.** Corresponding contour plot. Contours for $f_e < 0.135$ are drawn with dashed lines to highlight the trapped electron phase space structure.

In the limit of $\gamma \to 0$, this gives the perturbation

$$f_p(x,v) = \frac{-eE_0}{m_e(\omega_r - kv)} sin(kx - \omega_r t)\partial_v f_u \tag{5.20}$$

Note that Eq.(5.20) contains no singularities since $\partial_v f_u|_{v_p} = 0$ and ω_r is chosen to be real. This is not intended as an exact description of the EAW, rather it serves as an approximation sufficient to use an initial condition for numerical simulations. As described below, after some initial transient variation, the system settles into a stable traveling EAW.

The Vlasov-Poisson system is initialised in a periodic box with the distribution function $f_e = f_u + f_p$ and $\omega = 0.6\omega_{pe}$, $k = 0.4\lambda_D^{-1}$, $\delta n = 0.1 n_e$ where $\delta n = E_0/L_x$. In this regime of (ω, k) one would not normally expect an electron plasma wave to propagate, undamped or otherwise. Figure 5.3 shows the trapped electron distribution of the EAW after a thousand inverse plasma frequencies. Figure 5.4 shows that the amplitude of the EAW is effectively constant after an initial transient phase, only weak numerical damping remains. A non-Maxwellian distribution, specifically the flattening at the phase velocity of the wave, is a necessity for the propagation of an EAW.

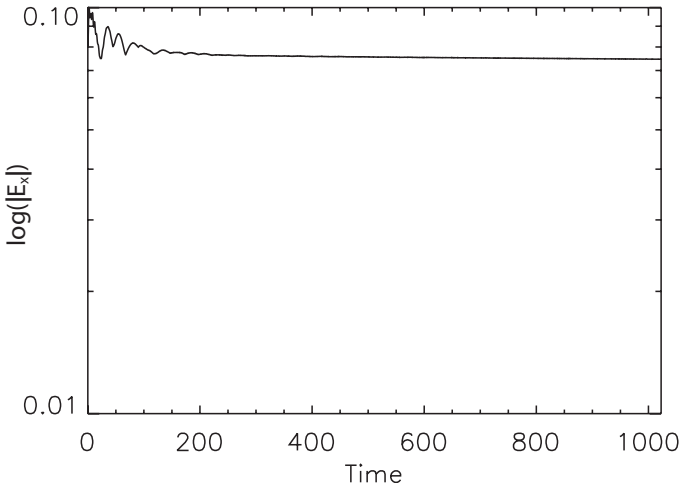

Figure 5.4: Logarithmic electric field amplitude of EAW ($\delta n = 0.1 n_e, \omega = 0.6\omega_{pe}, k = 0.4/\lambda_D$) against time. After an initial transient stage, the EAW persists as an electron plasma wave with frequency below the plasma frequency, which is undamped except for limited damping due to numerical diffusion

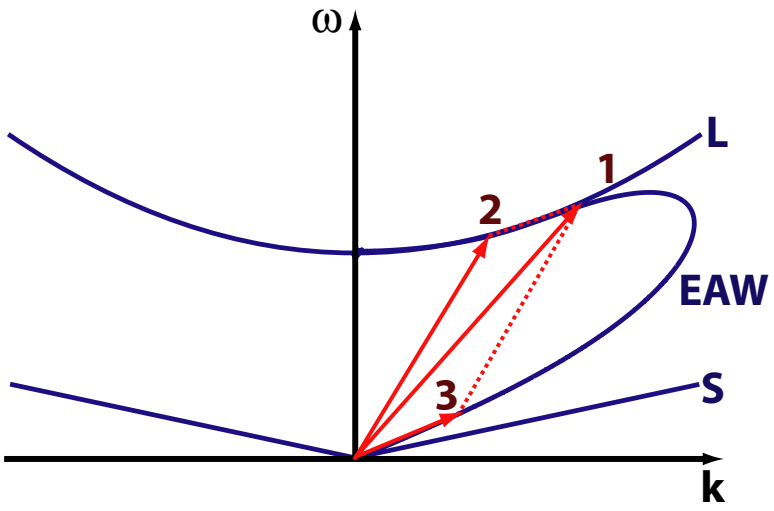

Figure 5.5: Diagrammatic representation of the dispersion relations for Langmuir waves (L), ion acoustic waves (S) and electron acoustic waves (EAW). The Langmuir decay instability is shown with an EAW in place of the ion acoustic wave.

5.5 Relevance to the Langmuir Decay Instability

A Langmuir wave can decay into a second Langmuir wave of lower wavenumber plus an ion-acoustic wave (IAW). This process can occur repeatedly, forming a Langmuir cascade [86]. Can the EAW perform the role of the IAW to produce a Langmuir cascade on electron timescales, as shown in Fig.5.5?

Section 1.5.7 discussed how the conventional Langmuir cascade [31] proceeds for all k above a critical value k_c, determined by the point where the group velocity, $\partial\omega/\partial k$, of the parent Langmuir wave (L) is equal to that of the IAW:

$$\frac{\partial\omega_L}{\partial k} = \frac{\partial\omega_{IAW}}{\partial k} \Rightarrow k_c = \frac{1}{3\lambda_D}\sqrt{\frac{m_e}{m_i}} \tag{5.21}$$

A similar analysis, for small k, can be performed in the case where the IAW is replaced with an EAW. Approximating the Langmuir dispersion relation by

$$\omega \approx \omega_{pe}\left(1 + 3k^2\lambda_D^2/2\right) \tag{5.22}$$

and the EAW dispersion relation by

$$\omega \approx \omega_{pe}\left(1.35k\lambda_D\right) \tag{5.23}$$

gives a critical wavenumber $k_c \approx 0.45\lambda_D^{-1}$, suggesting that LDI via the EAW might be a possibility. However, Eqns 5.22 and 5.23 are no longer valid for such a high k_c. The assumption of small k is therefore abandoned and the gradients calculated numerically [84] to give Fig. 5.6. It follows from this full treatment, valid for all k, that a process of Langmuir decay via the electron acoustic branch is not possible. However, this does not rule out all forms of interplay between LDI and EAWs. The upper branch of the dispersion relation, essentially an undamped form of the conventional Langmuir mode, may replace one or both of the Langmuir waves in the LDI without affecting the critical wavenumber. This scenario is left for future work.

5.6 Stimulated Electron Acoustic Scattering (SEAS)

The collective scattering of incident laser light from an EAW can be simulated using the Vlasov-Maxwell model developed in chapter 4. The relativistic Vlasov equation for

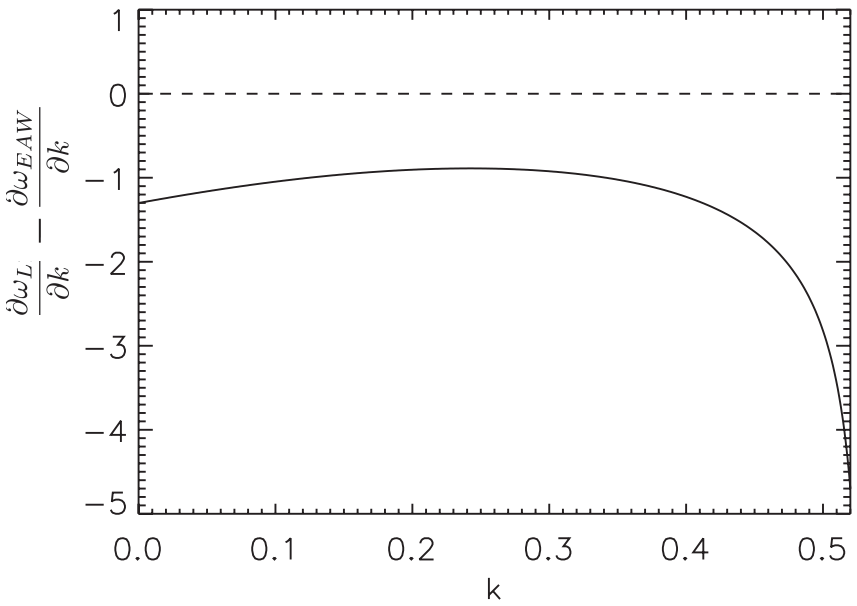

Figure 5.6: Difference between the gradients of the dispersion relations of the Langmuir and Electron Acoustic modes for a range of k. In order for Langmuir decay to occur this quantity must be greater than zero. The critical wavenumber k_c is the point at which the gradients are exactly equal. This curve remains negative for all k, demonstrating that Langmuir decay via the EAW, rather than the IAW, is not possible.

electrons in the presence of transverse fields (Eq.(4.14)) is solved against a stationary ion background, together with Maxwell's equations (Eqs.(4.9), (4.10) and (4.11)) in one dimension. The transverse motion of particles is treated as fluid-like using Eqs.(4.18) and (4.23).

The system of normalised units described in section 4.2.2 is adopted in which time is normalised in units of ω_{pe}^{-1} and velocities to units of c etc. The initial conditions are chosen with $n_e = 0.6n_c$, greater then quarter critical density to prohibit conventional SRS. The system is periodic in x and undriven, with a TEM wave present throughout the system initially, a similar configuration to the SRS problem discussed in section 4.3. A low amplitude density perturbation is added to a Maxwellian velocity distribution to seed the growth of the EAW. The wavenumbers and frequencies of the incident wave $E1$, scattered wave $E2$ and the EAW seed are chosen to satisfy the matching conditions for SEAS.

$$\tilde{k}_{E1} = 0.815 \tag{5.24}$$

$$\tilde{k}_{E2} = -0.108 \tag{5.25}$$

$$\tilde{k}_{EAW} = 0.923 \tag{5.26}$$

$$\tilde{\omega}_{E1} = 1.29 \tag{5.27}$$

$$\tilde{\omega}_{E2} = 1.0058 \tag{5.28}$$

$$\tilde{\omega}_{EAW} = 0.2842 \tag{5.29}$$

The incident wave amplitude is $\tilde{E}_1 = 0.3$ and the system length $\tilde{L}_x \approx 3084$. Figure 5.7 shows the electron distribution function at late time. The evolution of trapped electron structures, and resulting flattening of the distribution function, is visible, corresponding to an EAW. This represents SRS-like scattering in a plasma whose density is greater than quarter critical, incident light is scattered from an EAW, an electron plasma wave with a frequency below the plasma frequency.

This demonstrates the ability of Vlasov-based kinetic plasma model to simulate the scattering of incident laser light from non-Maxwellian, trapped particle distributions. The development of such instabilities in realistic parameter regimes, and in the presence

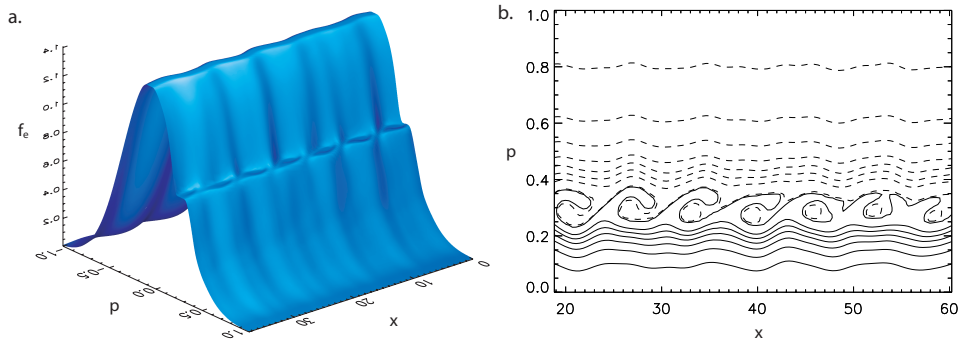

Figure 5.7: **a.** Surface plot of the electron distribution function at $\tilde{t} = 10^4$. Only a small section of the complete system is shown for clarity. Electron trapping and flattening of the distribution function can be seen: this is the EAW which has grown from a background density perturbation as a result of SEAS. Axes are given in relativistic units, c/ω_{pe} for space and $m_e c$ for momentum. **b.** Corresponding contour plot. Contours below $f_e = 0.725$ are drawn with dashed lines to highlight the trapped electron holes.

of an externally driven TEM wave, is now considered.

5.7 Kinetic Effects in Single Hot-Spot Experiments

Non-Maxwellian particle distributions, which require a kinetic treatment of the plasma, can significantly affect the scattering of incident light, disrupting the idealised three-wave parametric instability by allowing scattering from plasma oscillations omitted from conventional fluid treatments, such as the EAW. Section 5.2 summarised the linear theory underpinning the EAW, section 5.4 demonstrated its existence in the non-linear regime by way of electrostatic Vlasov-Poisson simulations, and section 5.6 confirmed the possibility of stimulated scattering, like SRS, from an EAW in a plasma of greater than quarter critical density. This section utilises the extended Vlasov-Maxwell code (see section 4.4) to investigate SEAS and related kinetic effects in a regime close to that achieved in single hot-spot experiments [24, 25]. Most significantly, this involves less than quarter critical densities (hence permitting SRS) and the presence of a continuous EM driver with non-periodic boundaries.

5.7.1 Initial Conditions

Again, the system of normalised units described in section 4.2.2 is adopted. The laser intensity I_0, electron temperature T_e and density n_e achieved in single hot-spot experiments were, approximately

$$I_0 = 1.6 \times 10^{16} \mathrm{Wcm}^{-2} \tag{5.30}$$

$$T_e = 350 \mathrm{eV} \tag{5.31}$$

$$n_e = 1.2 \times 10^{20} \mathrm{cm}^{-3} = 0.03 n_c \tag{5.32}$$

corresponding to simulation values for the parameters; incident EMW amplitude (E_{y_0}) and frequency (ω_0), thermal velocity (v_{Te}) and density (n_e) of

$$\tilde{E}_{y_0} = 0.33 \tag{5.33}$$

$$\tilde{\omega}_0 = 5.7775 \tag{5.34}$$

$$\tilde{v}_{Te} = 0.026 \tag{5.35}$$

$$n_e = 1 \times \omega_{pe}^2 \epsilon_0 m_e / e^2 = 0.03 n_c. \tag{5.36}$$

To minimise the charge loss from the system, a 'flat-top'density profile is chosen. Here the density of both electrons and the neutralising ion background drops smoothly from n_0 to zero over a distance ≈ 40, in normalised units, at the edges of the system. The simulation domain extends from $\tilde{x} = 0$ to $\tilde{x} = 220$, leaving a flat region at the centre of the simulation box approximately $140 c \omega_{pe}^{-1}$ in length, and from $\tilde{p} = -0.75$ to $\tilde{p} = 0.75$. The simulation grid has $16,384$ points in x and $1,024$ points in p. The simulation runs to an end time of $\tilde{t} = 1200$. Such resolution necessitates the use of the multiprocessor implementation of the EM Vlasov code.

5.7.2 Results

Figures 5.8 and 5.9 display windowed Fourier transforms of the electrostatic field and of the back-propagating EM field, taken with a Hanning window of size $\approx 75 \omega_{pe}^{-1}$, at the centre of the system. These show conventional SRS followed by scattering from low frequency plasma waves after $\tilde{t} = 600$.

In the initial SRS burst, starting at $\tilde{t} \approx 450$ the EM driver scatters from a Langmuir wave at $\tilde{\omega}_1 = 1.06$, $\tilde{k} = 0.27$, $v_p = 3.93 v_{Te}$, to produce reflected light at a frequency $\tilde{\omega}_1 = 4.72$. The instability saturates via the trapping of electrons. Figure 5.10a shows the electron distribution function during the late stages of the SRS burst, when electrons have been trapped and accelerated. A beam, similar to that observed in simulations of Raman forward scatter[81], forms in the electron distribution which is clearly visible in plots (Fig.5.10b). The trapping of electrons by the Langmuir waves driven through SRS evolves into a plateau in the electron distibution. This flattened region extends to low phase velocities, providing an environment in which low frequency plasma modes are able to grow and propagate. These low frequency modes are visible in the electrostatic field spectrum after the collapse of the initial SRS burst, and correspond to two distinct electron acoustic waves (eaw1 and eaw2) at $\tilde{\omega}_{eaw1} = 0.73$, $\tilde{k} = 0.27$, $v_p = 2.73 v_{Te}$ and $\tilde{\omega}_{eaw2} = 0.57$, $\tilde{k} = 0.28$, $v_p = 2.03 v_{Te}$.

The electron distribution at late times deviates significantly from a Maxwellian. The trapping of electrons in the initial SRS burst flattens the distribution around $p = 0.1$, allowing the development of low frequency plasma waves, the EAWs, whose trapped electrons further distort the distribution of particles. By the simulation's end, it has become clear that the plasma, and hence the modes which it supports, is not well described by linear or fluid approximations. Scattering observed in single hot-spot experiments was from EAWs with phase velocity $\tilde{v} = 1.4$ ($\tilde{k} = 0.29$, $\tilde{\omega} = 0.41$), with a backscattered wave amplitude aproximately three thousand times smaller than that from SRS. The amplitude of EAWs, and of the light scattered from them, observed in simulations is greater than observed experimentally. The simulations presented here also produce EAWs with higher phase velocities (i.e. $v_p \approx 2.7 v_{Te}$ and $v_p \approx 2.0 v_{Te}$ compared to $v_p \approx 1.4 v_{Te}$) than the scattered spectra from experiments indicates. These two deviations are closely related. As shown earlier, the dispersion relation for the EAW is dictated in part by the mode amplitude. As the EAW amplitude is increased, the dispersion relation shifts inwards (as shown in Fig.5.1) resulting in a higher phase velocity, at fixed wavenumber. Further work is required to explain this inconsistency between numerical and experimental results.

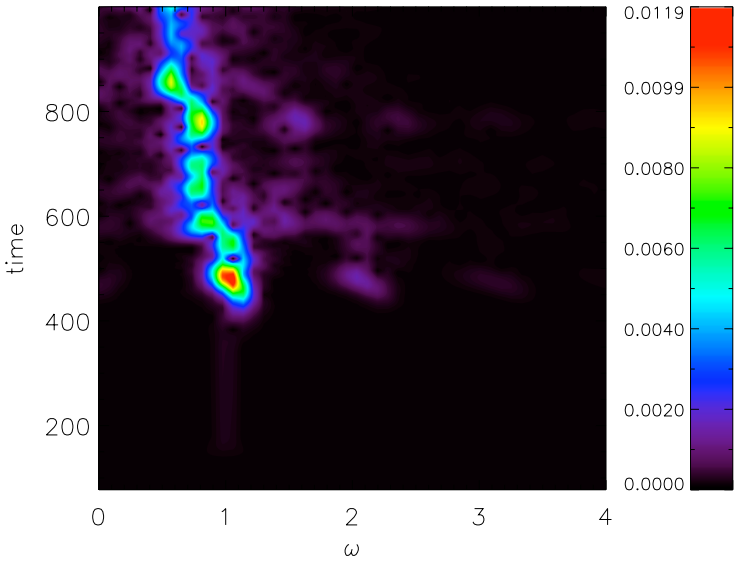

Figure 5.8: Windowed Fourier transform of the electrostatic field E_x at the centre of the system. An initial SRS burst at $\tilde{t} \approx 450$ saturates via the trapping of electrons which distort the initially Maxwellian distribution and provide an environment in which waves below the plasma frequency can grow and propagate. The traces at $\tilde{\omega} \approx 0.8$ and $\tilde{\omega} \approx 0.6$, first appearing at $\tilde{t} \approx 600$, represent EAWs with phase velocities at $v_p = 2.73 v_{Te}$ and $2.03 v_{Te}$ respectively.

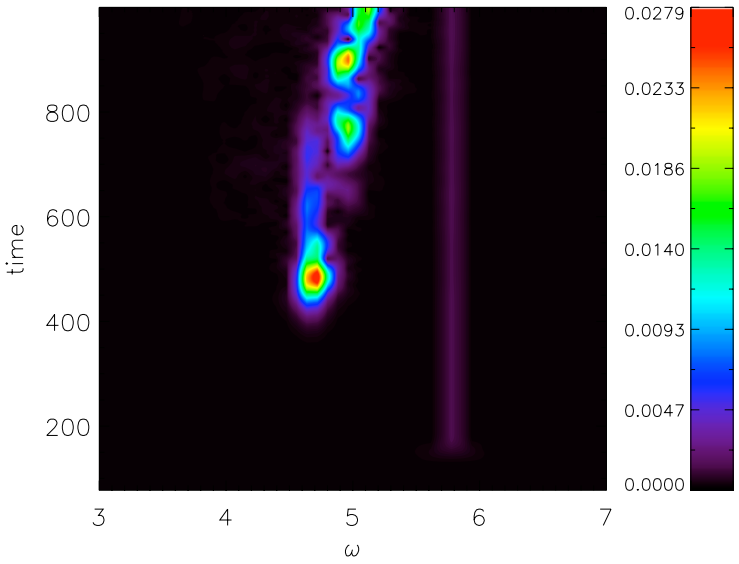

Figure 5.9: Windowed Fourier transform of the backwards propagating EM field at the centre of the system. The spectrum shows the light scattered by Langmuir waves (SRS) and EAW waves (SEAS) identified in the electrostatic spectrum at the same point in space (see Fig.5.8).

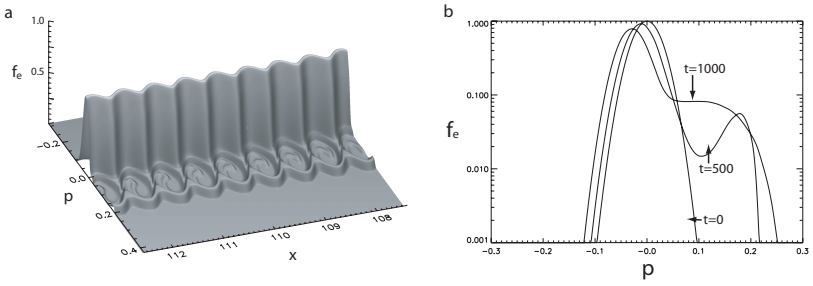

Figure 5.10: **a.** Surface plot of the electron distribution near the centre of the system at $\tilde{t} = 500$. Electron trapping, visible here, is responsible for the saturation of the Raman instability and the creation of the electron beam in the specially integrated distribution. **b.** Spatially integrated electron distribution functions, for $\tilde{t} = 0$, 500 and 800, normalised to the initial Maxwellian distribution. The trapping of electrons in the Langmuir wave driven by SRS temporarily creates a beam structure. The collapse of this structure is responsible in part for the formation of a broad plateau in momentum space at late times.

The simulation runtime, $\tilde{t} = 1200$, is equivalent to less than three picoseconds - this serves to highlight the how rapid the switch from the fluid to the kinetic regime may be, at the laser intensities considered here. As laser intensity increases, the kinetic effects discussed here will become more critical to the understanding of the associated laser-plasma interaction physics.

5.8 Summary

Experiments studying fundamental laser-plasma interaction in a single hotspot [24, 25] observed backscattered light from the interaction of the incident beam with two distinct plasma modes. First, there is scattering from waves with high phase velocity $\tilde{v}_p \approx 4.2$ and a frequency above the plasma frequency ω_{pe}, which was attributed to SRS the three-wave parametric instability involving a Langmuir wave. Second, there is scattering from waves of considerably lower phase velocity $\tilde{v}_p \approx 1.4$ whose frequency is below the plasma frequency, as low as $\tilde{\omega} \approx 0.41$, in normalised units. These low frequency modes were identified as the electron acoustic wave. Simulations have attempted to reproduce this scattering using a 1D Vlasov-Maxwell approach. These have been successful in achieving scattering from both high and low frequency electron plasma waves, but have not been able to reproduce exactly the phase velocities of the EAWs and the relative amplitudes of the scattering events.

The electron acoustic mode is a counter-intuitive phenomenon with a sparse literature: an electron plasma wave which propagates, free from Landau damping, at frequencies below the plasma frequency. This chapter has sought to clarify its characteristics, in terms of dispersion relation and the role of electron trapping, which present an interesting application of kinetic theory. Recent observations demonstrate the possibility for LPI involving the EAW. Simulations show this remains a possibility even in regimes where (for example) SRS is prohibited. Accurate representation and evolution of the complete phase space is of importance to SEAS, but it is also vital to the saturation of the Raman scattering instability and the subsequent evolution for the system, as demonstrated here.

The possibility of LDI involving an EAW is an interesting one. Since it would allow a potential saturation mechanism for SRS to evolve on electron (rather than ion) time scales. However, the analysis presented here demonstrates that the IAW cannot be replaced by an EAW in this context.

Simulations in a regime close to those achieved in single hot-spot experiments highlight the importance of kinetic effects in understanding LPI and the effect that the evolution of non-Maxwellian particle distributions may have on the scattering of incident light from an initially homogenous plasma.

Recent work [87, 88, 33] has identified the need for a deeper understanding of LPI, particularly in the regimes currently being approached by the next generation of lasers. Fluid-based treatments are not alone sufficient, and the saturation of SRS via LDI, Stimulated Brillouin Scattering (SBS), SEAS and the interplay between various instabilities benefits from being considered as a fully kinetic problem. The accurate, noise free, representation and evolution of the particle distribution functions provided by a Vlasov code make it a valuable additional tool. While a full 3D treatment is beyond the limits of current computing power, 1D and 2D Vlasov systems are tractable and can address many relevant problems.

Chapter 6

Conclusion

In this thesis the relativistic Vlasov Poisson model has been used to investigate non-linear kinetic acceleration mechanisms. It was shown in chapter 2 that the breaking of Langmuir waves as they move into regions of depleted density can accelerate small populations of electrons to high energies on time-scales of only one electron plasma period. These accelerated electrons form what has been termed a phase space jet. It was shown that the occurrence of wave breaking, for a Langmuir wave of given amplitude, is directly related to the depth and gradient of the density drop which the Langmuir wave encounters. The high phase space resolution of the Eulerian Vlasov code is ideally suited to resolving the fine phase space structure of the jets. This work has been published in [N. J. Sircombe, T. D. Arber and R. O. Dendy, *Accelerated electron populations formed by Langmuir wave-caviton interactions*, Phys. Plasmas, **12**, 012303 (2005)].

In chapter 3 the relativistic Vlasov Poisson model was used to consider the growth and saturation of electrostatic waves in systems dominated by the presence of two counter propagating ion beams. The stability of these electrostatic waves has a direct impact on the effectiveness of the electron surfing acceleration mechanism - proposed as a source of hot electrons at supernova remnant shock fronts. Such shocks are believed to be the source of ultra-relativistic electrons, accelerated by Fermi acceleration, observed in cosmic rays. Fermi acceleration, however, requires an initial electron population with sufficient kinetic energy to make repeated crossings of the

shock front. The stability of the electrostatic waves was found to be in agreement with previously published work and the noise-free representation of the particle phase space afforded by the Vlasov code allowed the identification of secondary acceleration mechanisms. Coupling between electrostatic waves excited by the counter propagating ion beams was shown to drive high phase velocity waves to amplitudes where they could trap and accelerate electrons. In this manner it may be possible to produce seed populations for Fermi acceleration with relatively low initial ion beam velocities. This work was based on work submitted for publication [N. J. Sircombe, M. E. Dieckmann, P. K. Shukla and T. D. Arber, *Stabilisation of BGK modes by relativistic effects*, Astronomy and Astrophysics, In Press] and [M. E. Dieckmann, N. J. Sircombe, M. Parviainen, P. K. Shukla and R. O. Dendy, *Phase speed of electrostatic waves: The critical parameter for efficient electron surfing acceleration*, Plasma Phys. Control. Fusion **48** (2006) 489].

The electrostatic Vlasov model has been extended to cover the full electromagnetic Vlasov Maxwell system in order to allow the direct simulation of laser plasma interaction. This required the development and testing of a numerical approach which utilised the existing core solver of the Vlasov Poisson code, as described in chapter 4. In chapter 5 it was explained how the Vlasov Maxwell model has been applied to the problem of scattering from the electron acoustic mode. This electron plasma wave is able to propagate, with negligible damping, at frequencies below the electron plasma frequency. It is supported by the trapping of electrons, and as such, requires a kinetic treatment. It was shown that is is possible to excite an electron acoustic wave and scatter incident light, even at densities where conventional Raman scattering would be prohibited. In a regime similar to those achieved in single hot-spot experiments, a considerable degree of backscatter was observed. The phase velocity and amplitudes of the electron acoustic waves observed in these simulations are higher than those observed in experiment. This is an inconsistency which requires further work and continued development of the Vlasov Maxwell code (as discussed below). This work has been submitted for publication [N. J. Sircombe, T. D. Arber and R. O. Dendy *Kinetic effects in Laser-Plasma coupling: Vlasov theory and computations*, Submitted to Plasma Physics and Controlled Fusion].

Future Work

The one-dimensional Vlasov Maxwell model is ideal for studying laser plasma interaction in regimes where kinetic effects are important. At the intensities planned for future laser systems, the saturation of instabilities such as Raman and Brillouin scattering can be best understood from a kinetic standpoint which accurately represents the particle trapping and the resulting phase space structure. To develop the code further, to the point where it has the ability to deliver accurate estimates of the reflectivity for future experimental programmes, would require its extension to higher dimensions. In two dimensions the Vlasov code would be able to address the full gamut of plasma instabilities, including two-plasmon decay, two-ion wave decay and beam filamentaion. This would equate to a significant increase in the computational power required for simulations but should remain tractable, while full three dimensional modelling would offer little real advantage for a considerable cost in terms of computational resources.

Bibliography

[1] J. Nuckolls, L. Wood, A. Thiessen, and G. Zimmerman. Laser Compression of Matter to Super-High Densities: Thermonuclear (CTR) Applications. *Nature*, 239:139, 1972.

[2] J. Lindl. Development of the indirect-drive approach to inertial confinement fusion and the target physics basis for ignition and gain. *Phys. Plasmas*, 2:3933, June 1995.

[3] T. R. Dittrich, S. W. Haan, M. M. Marinak, S. M. Pollaine, and D. E. Hinkel *et al.* Review of indirect-drive ignition design options for the national ignition facility. *Phys. Plasmas*, 5:1966, 1998.

[4] *Proceedings of Inertial Fusion Sciences and Applications, 2005*. In Publication.

[5] Peter Amendt, T. J. Murphy, and S. P. Hatchett. Novel symmetry tuning in nova hohlraums using axial gold disks. *Phys. Plasmas*, 3:4166, 1996.

[6] S. Skupsky, J. A. Marozas, R. Betti R. S. Craxton, and T. J. B. Collins *et al.* Polar direct drive on the national ignition facility. *Phys. Plasmas*, 11:2763, 2004.

[7] M. Tabak, J. Hammer, M. E. Glinsky, W. L. Kruer, S. C. Wilks, J. Woodworth, E. M. Campbell, and M. D. Perry. Ignition and High-Gain with Ultrapowerful Lasers. *Phys. Plasmas*, 1:1626, 1994.

[8] M. H. Key. Fast track to fusion energy. *Nature*, 412:775, 2001.

[9] M. H. Key, M. D. Cable, T. E. Cowan, K. G. Cowan, and K. G. Estabrook *et al.* Hot electron production and heating by hot electrons in fast ignitor research. *Phys. Plasmas*, 5:1966, 1998.

[10] E. Kodama, P. A. Norreys, K. Mima, A. E. Dangor, and R. G. Evans *et al.* Fast heating of ultrahigh-density plasma as a step towards laser fusion ignition. *Nature*, 412:798, 2001.

[11] T. Tajima and J. M. Dawson. Laser Electron Accelerator. *Phys. Rev. Lett.*, 43:267, 1979.

[12] J. G. Wang, D. F. DuBois, G.L. Payne, and H. A. Rose. Vlasov simulation of modulational instability and Langmuir collapse. *Phys. Plasmas*, 2:1129, April 1995.

[13] A. Salcedo. *Coupled Modes Analysis or SRS Backscattering, with Langmuir Decay and Possible Cascadings*. PhD thesis, Massachusetts Institute of Technology, December 2001.

[14] R. J. Focia. *Investigation and Characterisation or Single Hot Spot Laser-Plasma Interactions*. PhD thesis, Massachusetts Institute of Technology, December 2001.

[15] P. A. Sturrock. *Plasma Physics*. Cambridge, 1996.

[16] R. O. Dendy. *Plasma Dynamics*. Oxford Science.

[17] L. D. Landau. *Sov. Phys. JETP*, 10:25, 1946.

[18] E. Infeld and G. Rowlands. *Nonlinear waves, solitons and chaos*. Cambridge, 1992.

[19] J. P. Holloway and J. J. Dorning. Undamped longitudinal plasma-waves. *Phys. Lett. A*, 138:279, 1989.

[20] J. P. Holloway and J. J. Dorning. Undamped plasma waves. *Phys. Rev. A*, 44:3856, 1991.

[21] H. Schamel. Electron holes, ion holes and double layers : Electrostatic phase space structures in theory and experiment. *Physics Reports*, 140:162, 1986.

[22] H. Schamel. Hole equilibria in Vlasov-Poisson systems: A challenge to wave theories of ideal plasmas. *Phys. Plasmas*, 7:4831, 2000.

[23] L. Friedland, F. Peinetti, W. Bertsche, J. Fajans, and J. Wurtele. Driven phase space holes and synchronized Bernstein, Greene, and Kruskal modes. *Phys. Plasmas*, 11:4305, 2004.

[24] D. S. Montgomery, N. Renard-LeGalloudec, and H. A. Rose *et. al.* Observation of Stimulated Electron-Acoustic-Wave Scattering. *Phys. Rev. Lett.*, 87:155001, 2001.

[25] D. S. Montgomery, J. A. Cobble, and J. C. Fernández *et. al.* Recent Trident single hot spot experiments: Evidence for kinetic effects, and observation of Langmuir decay instability cascade. *Phys. Plasmas*, 9:2311, 2002.

[26] M. E. Dieckmann, B. Eliasson, A. Stathopoulos, and A. Ynnerman. Connecting shock velocities to electron-injection mechanisms. *Phys. Rev. Lett.*, 92:065006, 2004.

[27] A. Ghizzo, B. Izrar, P. Bertrand, E. Fijalkow, and R. Feix. Stability of berstein-green-kruskal plasma equilibria. numerical experiments over a long time. *Phys. Fluids*, 31:72, 1988.

[28] R. D. Gill. *Plasma Physics and Nuclear Fusion Research*. Academic Press, 1981.

[29] S. Eliezer. *The interaction of high power lasers with plasma*. IoP, 2002.

[30] R. A. Cairns. *Plasma Physics*. Blackie, 1985.

[31] S. G. Thornhill and D. ter Haar. Langmuir Turbulence and Modulational Instability. *Phys. Reports*, 2:43, 1978.

[32] U. Frish. *Turbulence, the Legacy of A. N. Kolmogorov*. Cambridge, 1995.

[33] S. H. Glenzer, P. Arnold, and G. Bardsley *et al*. Progress in long scale length laser-plasma interactions. *Nuclear Fusion*, 44:S185, 2004.

[34] J. Lindl, Amendt P, Berger RL, Glendinning SG, Glenzer SH, Haan SW, Kauffman RL, Landen OL, and Suter LJ. The physics basis for ignition using indirect-drive targets on the National Ignition Facility. *Phys. Plasmas*, 11:339, 2004.

[35] E. A. Williams, B. I. Cohen, L. Divol, M. R. Dorr, J. A. Hittinger, and D. E. Hinkel *et al.* Effects of ion trapping on crossed-laser-beam stimulated brillouin scattering. *Phys. Plasmas*, 11:231, 2004.

[36] R. M. Stevenson, L. J. Suter, K. Oades, W. Kruer, and G. E. Slark *et al.* Effects of plasma composition on backscatter, hot electron production, and propagation in underdense plasmas. *Phys. Plasmas*, 11:2709, 2004.

[37] D. J. Strozzi, M. M. Shoucri, and A. Bers. Study of laser plasma interactions using an Eulerian Vlasov code. *Comp. Phys. Comm.*, 164:159, 2004.

[38] T. D. Arber and R. G. L. Vann. A Critical Comparison of Eulerian-Grid-Based Vlasov Solvers. *J. Comp. Phys.*, 180:339, June 2002.

[39] E. Esarey and P. Sprangle. Overview of Plasma-Based Accelerator Concepts. *IEEE Trans. on Plasma Sci.*, 24:252, 1996.

[40] S. P. D. Mangles, C. D. Murphy, Z. Najmudin, and A. G. R.Thomas *et al.* Monoenergetic beams of relativistic electrons from intense laser-plasma interactions. *Nature*, 431:535, 2004.

[41] C. G. R. Geddes, C. Toth, J. van Tilborg, and E. Esarey *et al.* High-quality electron beams from a laser wakefield accelerator using plasma-channel guiding. *Nature*, 431:538, 2004.

[42] J. Faure, Y. Glinec, A. Pukhov, and S. Kiselev *et al.* A laser-plasma accelerator producing monoenergetic electron beams. *Nature*, 431:541, 2004.

[43] R. Bingham, J. T. Mendonça, and P. K. Shukla. Plasma based charge-particle accelerators. *Plasma Phys. Control. Fusion*, 46:R1–R23, 2004.

[44] S. Bulanov, N. Naumova, F. Pegoraro, and J. Sakai. Particle injection into the wave acceleration phase due to nonlinear wake wave breaking. *Phys. Rev. E*, 59:R5257, 1998.

[45] Z. Najmudin, K. Krushelnick, E. L. Clark, S. P. D. Mangles, A. E. Dangor, S. Fritzler, V. Malka, E. Lefebvre, D. Gordon, F. S. Tsung, and C. Joshi. Self-modulated wakefield and forced laser wakefield acceleration of electrons. *Phys. Plasmas*, 10:2071, 2003.

[46] A. Pukhov and J. Meyer-ter-Vehn. Laser wake field acceleration: the highly nonlinear broken-wave regime. *Appl. Phys. B*, 74:355, 2002.

[47] D. Umstadter, J. K. Kim, and E. Dodd. Laser Injection of Ultrashort Electron Pulses into Wakefield Plasma Waves. *Phys. Rev. Lett.*, 76:2073, 1996.

[48] F. Amiranoff, D. Bernard, B. Cros, F. Dorchies, F. Jacquet, V. Malka, J. R. Marques, G. Matthieussent, Ph. Mine, A. Modena, J. Morilllo, and Z. Najmudin. The laser wakefield acceleration experiment and Ecole Polytechnique. *Nucl. Instr and Meth. in Phys. Res. A*, 410:364, 1998.

[49] D. Pesme, S. Hüller, J. Myatt, C Riconda, A. Maximov, V. T. Tikhonchuk, C. Labaune, J. Fuchs, S. Depierreux, and H. A. Baldis. Laser-plasma interaction studies in the context of megajoule lasers for inertial fusion. *Plasma Phys. Control. Fusion*, 44:B53–B67, 2002.

[50] F. Califano and M. Lontano. Vlasov simulations of strongly nonlinear electrostatic oscillations in a one-dimensional electron-ion plasma. *Phys. Rev. E*, 58:6503, November 1998.

[51] A. I. Akhiezer and R. V. Polovin. Theory of Wave Motion of an Electron Plasma. *Soviet JETP*, 3:696, 1956.

[52] C. Z. Cheng and G. Knorr. The integration of the Vlasov equation in configuration space. *J. Comp. Phys*, 22:330, 1976.

[53] P. Colella and P.R. Woodward. The Piecewise Parabolic Method (PPM) for Gas-Dynamical Simulations. *J. Comp. Phys*, 54:174, 1984.

[54] N. E. Andreev, L. M. Gorbunov, and S. V. Kuznetsov. Acceleration of a Relativistic Electron Bunch in Linear and Nonlinear Plasma Waves. *Plas. Phys. Reports*, 21:1037, 1995.

[55] E. Fermi. *Phys. Rev.*, 75:1169, 1949.

[56] E. Fermi. *Ap. J.*, 119:1, 1954.

[57] A. R. Bell. The acceleration of cosmic rays in shock fronts. I. *MNRAS*, 182:147, 1978.

[58] A. R. Bell. The acceleration of cosmic rays in shock fronts. II. *MNRAS*, 182:443, 1978.

[59] A. A. Galeev. Generation of ultrarelativistic electrons by shock waves and the associated synchrotron emission. *Sov. Phys. JETP*, 59:965, 1984.

[60] R. A. Treumann and T. Terasawa. *Space Sci. Rev.*, 99:135, 2001.

[61] T. Katsouleas and J. M. Dawson. Unlimited Electron Acceleration in Laser-Driven Plasma Waves. *Phys. Rev. Lett.*, 51:392, 1983.

[62] N. Shimada and M. Hoshino. The dynamics of electron-ion coupling in the shock transition region. *Phys. Plasmas*, 10:1113, 2004.

[63] H. Schmitz, S. C. Chapman, and R. O. Dendy. Electron preacceleration mechanisms in the foot region of High Alfvenic Mach number shocks. *Ap. J.*, 579:327, 2002.

[64] K. G. McClements, R. O. Dendy, R. Bingham, J. G. Kirk, and L. O. Drury. *MNRAS*, 291:241, 1997.

[65] N. Shimada and M. Hoshino. Electron heating and acceleration in the shock transition region: Background plasma parameter dependence. *Phys. Plasma*, 11:1840, 2004.

[66] M. E. Dieckmann, P. Ljung, A. Ynnerman, and K. G. McClements. Large-scale numerical simulations of ion beam instabilities in unmagnetized astrophysical plasmas. *Phys. Plasmas*, 7:5171, 2000.

[67] M. E. Dieckmann, B. Eliasson, and P. K. Shukla. Streaming instabilities driven by mildly relativistic proton beams in plasmas. *Phys. Plasmas*, 11:1394, 2004.

[68] K. G. McClements, M. E. Dieckmann, A. Ynnerman, S.C. Chaoman, and R. O. Dendy. Surfatron and Stochastic Acceleration of Electrons at Supernova Remnant Shocks. *Phys. Rev. Lett.*, 87:255002, 2001.

[69] W. L. Kruer, J. M. Dawson, and R. N. Sudan. Trapped-Particle Instability. *Phys. Rev. Lett.*, 23:838, 1969.

[70] O. Buneman. Instability, Turbulence, and Conductivity in Current-Carrying Plasma. *Phys. Rev. Lett.*, 1:8, 1958.

[71] L. E. Thode and R. N. Sudan. Two-stream instability heating of plasmas by relativistic electron beams. *Phys. Rev. Lett.*, 30:732, 1973.

[72] Lee R, Chapman S C, and Dendy R O. Ion acceleration processes at reforming collisionless shocks. *Phys. Plasmas*, 12:012901, 2004.

[73] N. Shimada and M. Hoshino. Strong electron acceleration at high mach number shock waves: Simulation and study of electron dynamics. *Ap. J.*, 543:L67, 2000.

[74] M. Scholer, I. Shinohara, and S. Matsukio. Quasi-perpendicular shocks: Length scale of the cross-shock potential, shock reformation, and implication for shock surfing. *J. Geophys. Res.*, 108(A1):1014, 2003.

[75] B. Eliasson, M. E. Dieckmann, and P. K. Shukla. Simulation study of surfing acceleration in magnetized space plasmas. *New J. Phys.*, 7:136, 2005.

[76] M. E. Dieckmann, B. Eliasson, A. Stathopoulos, and A. Ynnerman. Connecting Shock Velocities to Electron-Injection Mechanisms. *Phys. Rev. Lett.*, 92:065006, 2004.

[77] N. J. Sircombe, M. E. Dieckmann, P. K. Shukla, and T. D. Arber. Stabilisation of BGK modes by relativistic effects. *Submitted to Astronomy and Astrophysics*.

[78] J. S. Lazendic, P. O. Slane, B.M. Gaensler, and S. P. Raynolds *et al.* A high-resolution study of nonthermal radio and X-ray emission from supernova remnant G347.3-0.5. *Ap. J.*, 602:271, 2004.

[79] J. B. Rosenzweig. Trapping, thermal effects, and wave breaking in the nonlinear plasma wake-field accelerator. *Phys. Rev. A*, 38:3634, 1988.

[80] S. R. Kulkarni, D. A. Frail, M. H. Wieringa, R. D. Ekers, and E. M. Sadler *et al.* Radio emission from the unusual supernova 1998bw and its association with the γ-ray burst of 25 April 1998. *Nature*, 395:663, 1998.

[81] A. Ghizzo, P. Bertrand, M. M. Shoucri, T. W. Johnston, E. Fijalkow, and M. R. Feix. A Vlasov Code for the Numerical Simulation of Stimulated Raman Scattering. *J. Comp. Phys.*, 90:431, 1990.

[82] C. K. Birdsall and A. B. Langdon. *Plasma Physics via Computer Simulation*. IoP, 1991.

[83] N. J. Sircombe, T. D. Arber, and R. O. Dendy. Accelerated electron populations formed by Langmuir wave-caviton interactions. *Phys. Plasmas*, 12:012303, 2005.

[84] W. H. Press, B. P. Flannery, S.I A. Teukolsky, and W. T. Vetterling. *Numerical Recipes in Fortran*. Cambridge, 1986.

[85] T. H. Stix. *The Theory of Plasma Waves*. McGraw-Hill, 1962.

[86] S. Depierreux, J. Fuchs, C. Labaune, D. Pesme, V. T. Tikhonchuk, and H. A. Baldis. First Observation of Ion Acoustic Wave Produced by the Langmuir Decay Instability. *Phys. Rev. Lett.*, 84:2869, 2000.

[87] D. Pesme, S. Huller, and J. Myatt *et al*. *Plasma Physics and Controlled Fusion*, 44:B53, 2002.

[88] C. Labaune, H. Bandulet, and S. Depierreux *et al*. Laser-plasma interaction experiments in the context of inertial fusion. *Plasma Physics and Controlled Fusion*, 46:B301, 2004.